TAMPEREEN TEKNILLINEN YLIOPISTO
TAMPERE UNIVERSITY OF TECHNOLOGY

EETU OJALA

PENETRATION OF PULP-FIBRE SUSPENSION JET

Master of Science thesis

Supervisor: Prof Reijo Karvinen
Examiner: University Lecturer Seppo Syrjälä
Examiner and topic approved by the
Faculty Council of the Faculty of
Engineering Sciences
on 7th December 2016

ABSTRACT

EETU OJALA: Penetration of pulp-fibre suspension jet
Tampere University of Technology
Master of Science thesis, 89 pages
November 2016
Master's Degree Programme in Environmental- and Energy Technology
Major: Energy Efficiency
Supervisor: Prof Reijo Karvinen
Examiner: University Lecturer Seppo Syrjälä
Keywords: Non-Newtonian, Wall Jet, PUDV, CFD, OpenFOAM, Pulp-fibre, Suspension

Manufacturing pulp and paper products is energy-intensive. A better understanding of flow behaviour of pulp-fibre suspension is essential for improving the efficiency of unit processes in pulp and paper industry. Computational fluid dynamics (CFD) offers a powerful tool for simulating the flow of pulp-fibre suspension in industrial processes. There is, however, a lack of experimental research on turbulent flow of pulp-fibre suspension for validation purposes.

The objective of this thesis is to present a new experimental method for measuring a flow field of turbulent pulp-fibre suspension wall jet. In order to validate the CFD simulation approach used in this work, the measurements were compared with the results obtained from CFD simulations. A novel experimental jet chamber was designed and built in Tampere University of Technology to measure the opening angle and penetration depth of pulp-fibre suspension jet discharging from a round pipe next to a wall. Photography was used to visually measure the jet spread and penetration depth, while Pulsed Ultrasound Doppler Velocimetry (PUDV) was used to obtain the velocity profile of the jet.

Open-source CFD toolbox OpenFOAM was used to simulate the flow field inside the jet chamber. The simulation basis consisted of combining a non-Newtonian Herschel-Bulkley material model with the $k - \omega$ SST turbulence model. Material model parameters used in the simulations were obtained from a previous research work conducted at Tampere University of Technology.

The simulations showed a reasonable agreement with the photographic measurements, but there was a significant deviation with the measured and simulated velocity profiles, especially in high fibre consistencies. The simulation approach used in this work can be used to model general flow properties of pulp-fibre suspension in process equipment with acceptable accuracy.

TIIVISTELMÄ

EETU OJALA: Kuitususpensiosuihkun tunkeutuminen
Tampereen Teknillinen Yliopisto
Diplomityö, 89 sivua
Marraskuu 2016
Ympäristö- ja Energiatekniikan koulutusohjelma
Pääaine: Energiatehokkuus
Ohjaaja: Professori Reijo Karvinen
Tarkastaja: Yliopistonlehtori Seppo Syrjälä
Keywords: vesikuitususpensio, turbulenssi, virtauslaskenta, epänewtoninen, PUDV

Kuitususpension virtauskäyttäytymisen parempi ymmärtäminen on merkittävässä roolissa paperiteollisuuden yksikköprosessien energiatehokkuuden parantamisessa. Numeerinen virtauslaskenta tarjoaa tehokkaan työkalun kuitususpension mallintamiseen teollisuuden prosesseissa. Virtauslaskennalla saadut tulokset vaativat kuitenkin kokeellisia mittauksia tukemaan ja validoimaan käytettyjä laskentamalleja. Kokeellisen tiedon puute turbulenttisen kuitususpension virtauskäyttäytymisestä heikentää luottamusta virtauslaskennan antamiin tuloksiin.

Tässä työssä esitetään uusi kokeellinen menetelmä turbulenttisen kuitususpensiosuihkun virtauskentän mittaamiseen. Työssä tehtyjä mittauksia verrattiin virtauslaskennan antamiin tuloksiin ja mittauksilla pystyttiin validoimaan simulaatiomallissa tehtyjä oletuksia. Suihkun mittaamista varten suunniteltiin ja rakennettiin koejärjestelmä Tampereen Teknillisen Yliopiston laboratorioon. Koejärjestelmän avulla valokuvattiin seinän vieressä purkautuvaa kuitususpensiosuihkua ja kuvia analysoimalla selvitettiin suihkun avautumiskulmaa ja tunkeutumaa. Lisäksi pulssitettua ultraääntä käytettiin suihkun nopeusprofiilin mittaamiseen.

Kokeellisen tilanteen mallintamiseen käytettiin avoimen lähdekoodin virtauslaskentaohjelmistoa OpenFOAM. Virtauslaskennan pohjana yhdistettiin epänewtoninen Herschel-Bulkley viskositeettimalli $k-\omega$ SST turbulenssimallin kanssa. Viskositeettimallin parametrit saatiin aikasemmasta TTY:llä suoritetusta tutkimuksesta.

Kuva-analyysiin perustuvien mittausten ja simulaatioiden välillä ei havaittu merkittäviä eroavuuksia. Ultraäänellä mitatut nopeusprofiilit eroavat kuitenkin huomattavasti simulaatioista, erityisesti isoilla kuitukonsentraatioilla. Tässä työssä esitetyllä simulaatiomenetelmällä on mahdollista ennustaa suspension virtauskäyttäytyminen teollisuuden prosessilaitteissa kohtuullisella tarkkuudella.

PREFACE

This work was conducted at Tampere University of Technology during 2016 and it was funded by EFEU program (Efficient Energy Usage) and TUT. The measurements were carried out in a laboratory located in Konetalo.

I would like to express my thanks to prof. Reijo Karvinen for providing guidance and supervising the work. Many thanks also goes to laboratory engineer Jarmo Ruusila and the laboratory staff, who helped me plan and construct the measurement equipment. I would also like to thank all my research colleagues for invaluable guidance with OpenFOAM and CFD. Lastly I would like to thank all my friends and family for support during all my years of studying.

CONTENTS

LIST OF ABBREVIATIONS AND SYMBOLS

CFD	Computational Fluid Dynamics
HB	Herschel-Bulkley
HW	Hardwood pulp
SBK	Semi Bleached Kraft Pulp
SST	Shear Stress Transport
TUT	Tampere University of Technology

δ	boundary layer thickness
N	crowding factor
ρ	density
ν_{eff}	effective kinematic viscosity
d	fibre diameter
ω_c	fibre coarseness
L	fibre length
u_τ	friction velocity
u^+	dimensionless velocity
ε	dissipation rate of turbulent kinetic energy
μ	dynamic viscosity
C_m	mass consistency of fibres
p	pressure
Ω	jet opening angle
ν	kinematic viscosity
δ_{ij}	Kronecker delta
l_η	Kolmogorov length scale
τ_η	Kolmogorov time scale
u_η	Kolmogorov velocity scale
ϕ	passive scalar
ϕ'	passive scalar fluctuation
Re	Reynolds number
$\dot{\gamma}$	shear rate
τ_{ij}	shear stress tensor
S_{ij}	strain-rate tensor
ν_t	turbulent eddy viscosity
I	turbulent intensity
k	turbulent kinetic energy
ω	turbulent dissipation frequency

u_i'	velocity fluctuation
u_i	velocity vector
σ_{ij}	viscous stress tensor
y^+	viscous wall unit
C_v	volumetric concentration of fibres
Q	volumetric flow rate
τ_0	yield stress
τ_w	wall shear stress

1. INTRODUCTION

Fibre suspension flows are encountered in various industrial manufacturing processes, such as paper production, food processing and textile manufacturing. The largest industrial sector that utilizes these flows is the the pulp and paper industry. Fibres in pulp and paper industry are most often produced from wood, but other fibrous plant sources are also used. The unit processes in pulp and paper industry are energy intensive, for example the typical power consumption of a motor in a bale slushing vat is in the range of 55-630 kW [26]. Understanding how fibre suspension flows behave in these unit processes is vital for designing and optimizing new and more energy efficient process equipment for pulp and paper industry.

Computational Fluid Dynamics (CFD) provides an useful tool for optimization and design of process equipment in industrial applications. Reliable and practically useful CFD simulations require that the physical phenomena governing the flow situation are completely understood and modelled correctly. Some examples of important flow situations and the related process equipment for pulp and paper industry are:

- Turbulent mixing (Pulpers, mixing tanks and centrifugal pumps)
- Non-Newtonian fluid flow (Pipes, valves and fittings)
- Turbulent planar jet (Headbox forming section)

The interaction between a non-Newtonian pulp-fibre suspension and turbulence is not completely understood. Most turbulence models used in industry and academia were developed with the assumption of Newtonian fluid behaviour. Thus, when simulating turbulent flows of non-Newtonian fluids, the non-Newtonian behaviour is only included in the selected viscosity model, which connects the apparent molecular viscosity of the fluid into the shear rate of the flow. Turbulence is modelled separately, with the assumption of Newtonian fluid behaviour. The validation of this approach is lacking as acquiring accurate velocity data is difficult from opaque fibre-suspensions.

In this thesis, the turbulent structure of a pulp-fibre suspension wall jet is under inspection. A novel experimental apparatus was designed and constructed to visualize highly opaque pulp-fibre suspension jets. In addition to visual measurements, pulsed ultrasound doppler velocimetry (PUDV) was used to determine the velocity profile of the jet.

The numerical computations of fibre-suspension flows were done using an open-source CFD toolbox OpenFOAM. The simulation approach used in this thesis is to model the turbulence with a RANS-turbulence model and the molecular viscosity with a non-Newtonian material model. The parameters for the material model were gained from a previous study conducted at TUT.

The goal of this thesis is to present the experimental method for visualizing turbulent fibre-suspension jets and compare the measured results with the results obtained from the CFD simulations. Chapter 2 describes the basic fundamentals of fibre-suspension flows. Chapters 3 and 4 are dedicated to the equations and models related to modelling turbulent flow of non-Newtonian fluid. Chapter 5 describes the experimental method used in the study of pulp-fibre suspension jet. Chapter 6 introduces the reader to the finite volume method in CFD and OpenFOAM case structure and usage. The measured and simulated flow fields are compared in chapter 7 and the final chapter summarizes the research.

2. CHARACTERISTICS OF PULP-FIBRE SUSPENSION FLOWS

2.1 Fibre properties

Wood is composed of tubular cells, which are commonly referred to as fibres. Fibres are held together by adhesive forces located in the intercellular polymers of the wood, such as lignin. For good quality paper, the fibres have to be separated from the rest of the raw materials in a process known as pulping.

The produced pulp is often dried up and formed into bales at a separate location, than the actual paper production site. These bales are then transported to paper production plant and slushed with water to form a thick slurry that can be pumped between the unit processes in the paper mill and eventually formed into an even sheet of paper in the paper machine.

Pulp can be produced chemically or mechanically, or by a combination of both methods. In mechanically produced pulp, the fibres are separated using a specifically designed grindstones or refiner plates. The wood can also be steamed before grinding, which reduces the energy consumption of the grinding process. In chemical pulp production, the fibres are separated by chemically dissolving ligning and other substances that keep the fibres in contact. In this pulping method, wood chips are cooked in a specific cooking liquid to completely separate the fibres. Mechanically produced pulp can consist of whole fibres, damaged fibres and fibre bundles whereas chemically produced pulp contains only completely separated fibres [8].

Fibre properties vary greatly even within the same wood species. Fibres typically have a length of 1 to 3 millimeters, while a typical diameter is between 15 to 30 micrometers [5]. Mechanical properties of the produced fibres are highly dependant on the wood quality and the method of pulping. Besides fibre length, other common parameters that affect paper quality are fibre coarseness, fibre curl, and fibre flexibility. Fillers such as calcium carbonate are added into fibres to improve optical qualities and printability of the final paper product.

2.2 Categorization of fibre suspensions

In the papermaking process, pulp-fibre suspensions are processed in a wide range of different consistencies, ranging from the very dilute suspension found in the headbox, to the thick slurry in slushers and stock chests. The flow behaviour of high consistency and low consistency suspension are drastically different. Fibre suspension in the pulp and paper industry is categorized coarsely to different groups by mass consistency C_m, which is defined as the mass of fibres in the suspension divided by the total mass of the suspension:

$$C_m\,[\%] = \frac{mass\ of\ fibres}{mass\ of\ suspension} \cdot 100\% \tag{2.1}$$

Low consistency suspensions have a $C_m < 5\%$ and are widely used in paper making processes. The typical consistency of pulp fibre suspension in the headbox forming section is between $0-1\%$. Low consistency paper pulp suspensions acts as a fibrous slurry, and can become turbulent in high enough flow rates [15]. Turbulence breaks down fibre networks and distributes fibres in the suspension more evenly. This effect is important, as the end quality of the paper product is determined by the fibre distribution in the headbox.

Medium and high consistency suspensions have a $C_m > 5\%$ and as the consistency increases, the suspension behavior begins to significantly alter from that of low consistency suspension. As the consistency increases above 10%, a considerable amount of air is trapped within the fibre network, making high consistency suspension a three-phase system. There is financial interest in increasing the mass consistency of the suspension inside the unit processes in paper production. Water and energy consumption could effectively be reduced if the same quality end product can be manufactured with high-consistency forming methods. For example, increasing the slushing consistency from 4.0% to 7.0%, reduces the energy consumption of the slushing process by 40% - 50% [26].

2.2.1 Crowding factor

Flocculation is the process of entanglement of individual fibres in the suspension to form groups of multiple fibres known as flocs. Flocculation occurs, when the concentration of fibres is high enough, which causes fibres to mechanically lock in on each other. Flocs are detrimental to good paper quality, as they cause the end product to have a heterogeneous distribution of fibres.

Kerekes and Schell [19] used crowding factor to categorize fibre suspensions and to study the flocculation of fibres. Crowding factor N is defined as the number of fibres in a spherical volume of diameter equal to the length of a fibre:

$$N = \frac{2}{3} C_v \left(\frac{L}{d} \right)^2, \tag{2.2}$$

where C_v is the volumetric concentration of the fibres, L the fibre length and d fibre diameter. The crowding factor can also be expressed approximately with mass consistency C_m and fibre coarseness ω_c (unit kg/m):

$$N = \frac{5 C_m L^2}{\omega_c} \tag{2.3}$$

When $N < 1$, fibres move freely in relation to one another and only random collisions exists between the fibres. As the crowding factor increases, more collisions happen and fibres begin to lock in on each other and eventually forming fibre networks. Table 2.1 presents a categorization of fibre suspension regimes based on the crowding factor:

Table 2.1 *Fibre suspension regimes*

Regimes	Type of fibre contact	Crowding Factor
Dilute	Chance Collision	$N < 1$
Semi-Concentrated	Forced Collision	$1 < N < 60$
Concentrated	Continuous Contact	$N > 60$

An important crowding factor of $N = 16$ was recognized by Martinez [22] as the gel concentration point. It was postulated by Martinez that at this point the interfibre contact in the suspension is high enough for the fibre network to bear loads. After the gel concentration point, the network strength increases dramatically with increasing N.

2.3 Rheological properties of fibre-suspension flows

Tanner defines rheology as the science of deformation and flow of materials [35]. The fundamental problem in rheological studies is relating the the conservation laws used in fluid dynamics, such as the conservation of mass, energy and forces, to flow kinematics imposed by the geometry and flow conditions. Rheology uses constitutive relations to link these two together. Well known examples of such relations are Hooke's law of elasticity and Newton's law of viscosity.

Often the material under study has a complex molecular structure, such as fibres suspended in water or long polymer chains. In engineering problems, there is no need to inspect the material behaviour at such a detailed level. A more practical approach is to use idealized continuum material models, which do not specify the microscopical structure of the material.

2.3.1 Apparent yield stress

The most noteworthy rheological property of pulp-fibre suspensions is the apparent yield stress. As the fibres in the suspension lock in on each other and form networks, a certain stress is required to break the network and 'fluidisize' the suspension. This stress is called the yield stress of the suspension. Many past works in the field of pulp-fibre suspensios have focused on estimating the value of this stress.

There are multiple ways to measure the apparent yield stress of fibre suspensions. Derakhshandeh [7] listed the most widely used methods and categorized them in the following manner:

Maximum viscosity method, where the shear stress of the suspension is increased and the viscosity of the suspension is measured. The apparent yield stress is the value of shear stress, where the maximum viscosity is found.

Apparent stress to initiate flow method, in which the shear stress-shear rate curve of the suspension is measured. The apparent yield stress is found, by extrapolating shear stress from the linear portion of the curve to zero shear rate.

Ultimate shear strength method, where the strain rate is increased and the apparent yield stress is the maximum stress reached until the suspension begins to flow. After flow begins the stress decreases, implying that the ultimate shear strength needs to be exceeded in the suspension for flow to begin.

Figure 2.1 depicts the maximum viscosity and apparent stress to initiate flow methods for determining yield stress of the suspension. Figure 2.2 shows a typical rotary vane geometry used in the yield stress measurements and the ultimate shear strenght method.

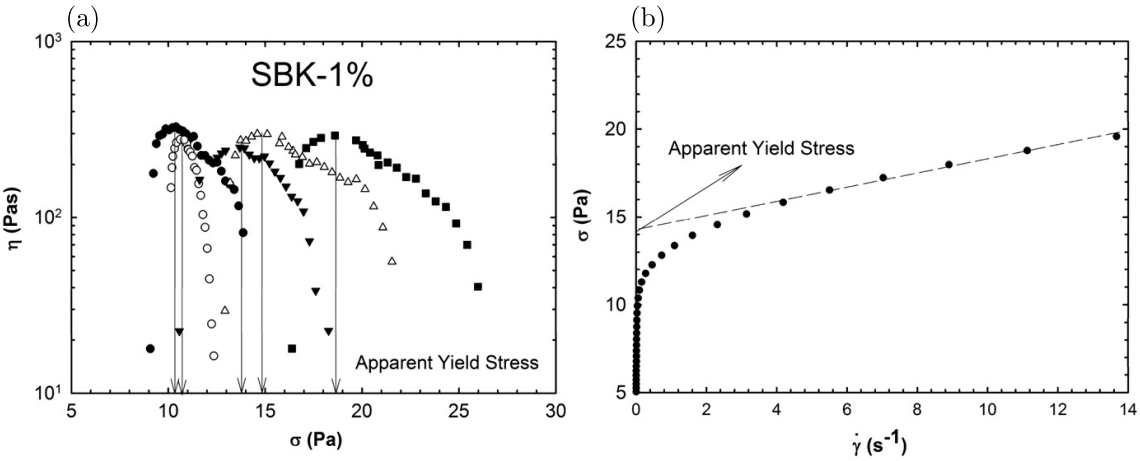

Figure 2.1 *(a): Maximum viscosity method (b): Apparent stress to initiate flow method [7]*

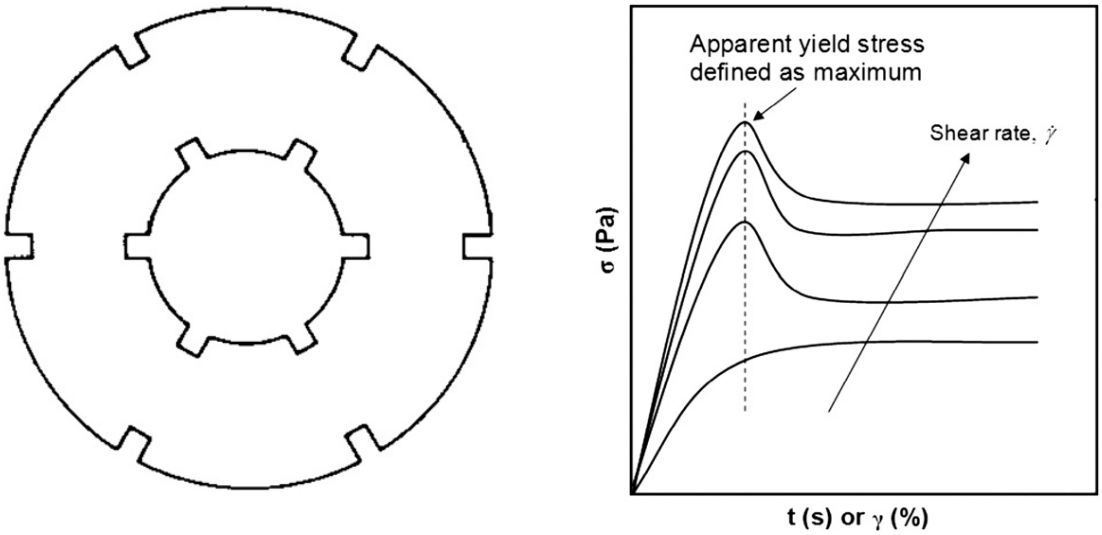

Figure 2.2 *(a): Rotary vane geometry (b): Ultimate shear strength method [7]*

Derakhshandeh [6] used a rotary vane rheometer and pulsed ultrasound doppler velocimeter to determine the yield stress for various pulp-fibre suspensions, at consistencies ranging from $C_m = 0.5 - 5\%$. The yield stress was found to have strong

dependency on the mass consistency of the suspension and a power-law model was used to express the relationship:

$$\tau_y = aC_m^b, \tag{2.4}$$

where a and b are experimental constants dependent on the physical properties of the fibres. Similar experiments were performed in Tampere University of Technology by Mustalahti [25]. Experimental constants a and b for different species of wood are presented in the table 2.2 from different experiments:

Table 2.2 *Experimental constants for yield stress power-law fit*

Method	Pulp	Reference	$a \times 10^{-5}$	b
Linear shear stress ramp	SBK	[6]	4.95 ± 0.20	2.33 ± 0.10
	HW	[6]	3.94 ± 0.23	2.60 ± 0.21
	TMP	[6]	35.2 ± 2.22	3.18 ± 0.25
	SGW	[6]	19.0 ± 0.96	3.16 ± 0.16
	Birch	[25]	1.086	2.64

Table 2.2 shows that the measured constants for the apparent yield stress vary greatly between wood species and production method. For example, the yield stress of a semi bleached kraft pulp (SBK) at 5% mass consistency, was measured by Derakhshandeh [6] to be 460.5 Pa. The yield stress of birch pulp at the same consistency, was measured by Mustalahti [25] to be approximately 40 Pa .

2.3.2 Flow regimes of pulp-fibre suspensions

The multiphase nature of fibre suspension flows has a complex effect on the flow pattern of the suspension. At low flow velocities the velocity gradients present in the flow are not strong enough to tear fibre flocs apart. As flow velocities increase the formed flocs begin to rupture and fibres are more evenly distributed in the suspension through turbulent diffusion.

In pipe flow situations the tendency for fibres to form flocs and turbulence to break these flocs apart means that different flow regimes for fibre suspensions can be identified based on the velocity of the flow.

Plug flow regime In pipe flow the fibres can create networks that cover the pipe cross section entirely. The formed plug scrapes along the pipe wall as it moves.

A pressure difference above a certain threshold value has to be applied in order to break down the fibre network sticking to the pipe wall.

When flow rate increases a water annulus forms between the plug and the pipe wall, which effectively lubricates the plug. Typically the thickness of the water annulus is less than 1 mm [18]. As the flow rate increases, the wall roughness of the pipe begins to have an effect and turbulent eddies are formed in the water annulus. These turbulent motions break down the plug and detach individual fibres from the plug into the water annulus.

Turbulent regime The water layer thickness increases as the flow rate increases and eventually the shearing forces in the suspension are so large that the turbulent motions prevent the formation of fibre plugs. At this flow regime the suspension becomes completely fluidised and fibres are randomly distributed in the suspension. Because the fibres dampen out turbulence, the pressure loss of pumping fibre suspension at the turbulent regime is smaller than that of pure water.

Figure 2.3 shows the drag reduction effect of fibre suspensions flows. $\Delta P/x$ is the pressure loss divided by the length of the pipe x and U_b is the bulk velocity of the flow. The dashed line represents the pressure loss of water.

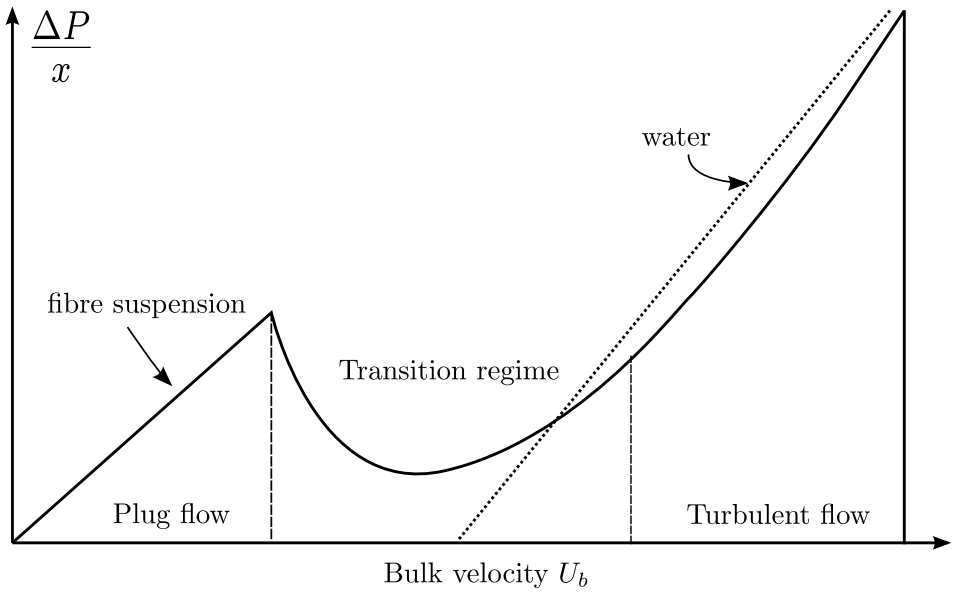

Figure 2.3 *Pressure loss of fibre suspension flow main regimes, dashed line represents water*

At medium and high consistencies suspensions are virtually always in the plug flow regime as the networks formed by the fibres are strong enough to withstand the shearing forces created by turbulence [7].

3. FLUID DYNAMICS

3.1 Conservation laws

Fluids are treated as a continuous substance, which means that the conservation laws from continuum mechanics have to be obeyed. For a infinitesimal fluid volume, the mass conservation equation can be written in the following form:

$$\frac{\partial \rho}{\partial t} + \nabla \cdot (\rho u_i) = 0, \tag{3.1}$$

where the first term in equation 3.1 is the rate of change in density ρ over time t. The second term is called the convection term and it describes the flow of mass out of the fluid volume. The density of the fluid can be assumed to be constant for an incompressible liquid. Thus for an incompressible fluid, equation 3.1 takes the form:

$$\nabla \cdot u_i = 0 \tag{3.2}$$

Newton's second law states that the rate of change in the momentum of a fluid particle is equal to the surface forces and body forces experienced by that fluid particle. The conservation equation for momentum for an infinitesimal fluid volume, can be expressed in the following form:

$$\frac{\partial}{\partial t}(\rho u_i) + \rho u_j \frac{\partial u_i}{\partial x_j} = -\frac{\partial p}{\partial x_i} + \frac{\partial \sigma_{ij}}{\partial x_j} + \mathbf{T}, \tag{3.3}$$

where $\frac{\partial}{\partial t}(\rho u_i)$ is the rate of change of momentum over time, $\rho u_j \frac{\partial u_i}{\partial x_j}$ is the convective momentum term, $\frac{\partial p}{\partial x_i}$ is the pressure gradient, σ_{ij} is the viscous stress tensor, and $\mathbf{T}$ the body-force vector. This vector can contain effects such as gravity or electromagnetic forces. If Newtonian fluid behaviour is assumed, the viscous stress tensor is given by a linear relationship between viscosity and deformation:

$$\sigma_{ij} = 2\mu S_{ij} - \frac{2}{3}\mu\delta_{ij}S_{kk}, \tag{3.4}$$

where μ is the fluid viscosity, S_{ij} the strain rate tensor and δ_{ij} the Kronecker delta. The strain rate tensor is defined as the symmetric part of the gradient of flow velocity:

$$S_{ij} = \text{sym}\left(\nabla u_i\right) = \frac{1}{2}\left(\nabla u_i + \left(\nabla u_i\right)^T\right) = \frac{1}{2}\left(\frac{\partial u_i}{\partial x_j} + \frac{\partial u_j}{\partial x_i}\right) \tag{3.5}$$

$$S_{kk} = \frac{1}{2}\left(\frac{\partial u_k}{x_k} + \frac{\partial u_k}{x_k}\right) \tag{3.6}$$

Using the continuity equation 3.1 in equation 3.6, it can be seen that for an incompressible fluid S_{kk} is equal to zero. The linear relationship between the viscous stress tensor and strain rate tensor in equation 3.4 only holds if Newtonian fluid flow is assumed. As mentioned in chapter 2, the viscosity of fibre-suspension is a variable which is dependant on the local shear rate of the flow. Thus, in order to solve the aforementioned equations for fibre-suspension flows, the non-Newtonian apparent viscosity of the suspension has to be modelled correctly.

3.2 Non-Newtonian fluids

Viscosity is the fluids property to resist shearing forces. A highly viscous fluid, such as motor oil, will flow more 'thickly' compared to a liquid with a lower viscosity, such as water. Figure 3.1 shows an example of the connection between viscosity and shear stress.

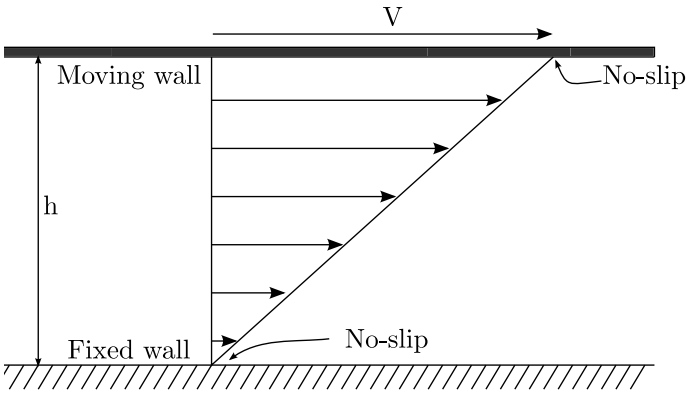

Figure 3.1 *Viscous fluid sheared between two plates [4]*

In the shown geometry, the upper plate with a surface area of A is moving at a constant velocity V, while the lower plate is fixed and the distance between the plates is h. Because of the no-slip condition at the plate surfaces, the flow speed varies linearly from zero at the bottom plate to V at the top plate. When applying equations 3.4 and 3.5 to the geometry in figure 3.1, the viscous stress tensor can be expressed in the following form:

$$\sigma_{ij} = \tau_{yx} = -\mu \frac{du}{dy} = \mu \dot{\gamma}_{yx}, \tag{3.7}$$

where the first subscript in τ_{yx} refers to the shearing plane normal and the second one refers to the direction of the force and flow. $\dot{\gamma}_{yx}$ is an important rheological variable, called shear rate. Shear rate shows the magnitude of shearing forces experienced by the fluid. Viscosity in non-Newtonian fluids is often modelled as a function of shear rate. The minus sign on the right hand of the equation 3.7 is because the stress resists the motion of the plate. Equation 3.7 can be rearranged into the following form:

$$\tau_{yx} = -\frac{\mu}{\rho} \frac{d}{dy} \left(\rho u \right), \tag{3.8}$$

where the quantity ρu is the linear momentum of the fluid. This form clearly shows that viscosity determines the rate of momentum transfer in the fluid in the y direction. The minus sign here means that momentum transfers from the upper plate to the lower plate. This form is analogous to Fourier's law of heat transfer, in which thermal conductivity of the material determines the heat flux between two different temperatures.

If viscosity is only dependent on pressure and temperature of the environment, the fluid is called Newtonian. Gases, water and simple organic liquids are all examples of Newtonian fluids. The viscosity of many industrial liquids, such as slurries and colloidal suspensions, is not a constant, but dependent on the flow circumstances.

Non-Newtonian fluids are fluids that depart from the Newtonian behaviour in any way. Because the definition of non-Newtonian fluid covers such a wide range of different fluids, it is useful to categorize these fluids based on their shear stress-shear rate behaviour.

Chhabra [4] recognized three different dominant features that can be used to categorize non-Newtonian fluids:

Generalized Newtonian fluids are time independent and show purely viscous behaviour.

Time-dependent fluids have a shear stress behaviour that is also dependent on the duration of the shearing motion and the kinematic history the fluid experienced.

Viscoelastic fluids exhibit behaviour from both fluids and solids, such as recovery after deformation.

The scope of this thesis is limited to generalized Newtonian fluids. Details of time-dependent fluids or viscoelastic fluids can be in found most engineering rheology books.

3.2.1 Generalized Newtonian fluids

Generalized Newtonian fluids are time-independent fluids. The shear stress of the fluid only depends on the shear rate experienced by the fluid at that particular time. The history of the shearing motion does not influence the shear stress. [4].

Many fluids in industrial applications exhibit shear-thinning behaviour, meaning that as the shearing motion in the fluid increases, the viscosity of the fluid decreases. As a result, the fluid begins to flow more freely. The opposite of shear-thinning is shear-thickening. As the shear rate in the fluid increases the fluid begins to resist the shearing force more and exhibiting solid like behaviour. Rheograms (shear stress plotted against shear rate) of Newtonian, shear-thinning and shear-thickening fluids are presented in figure 3.2.

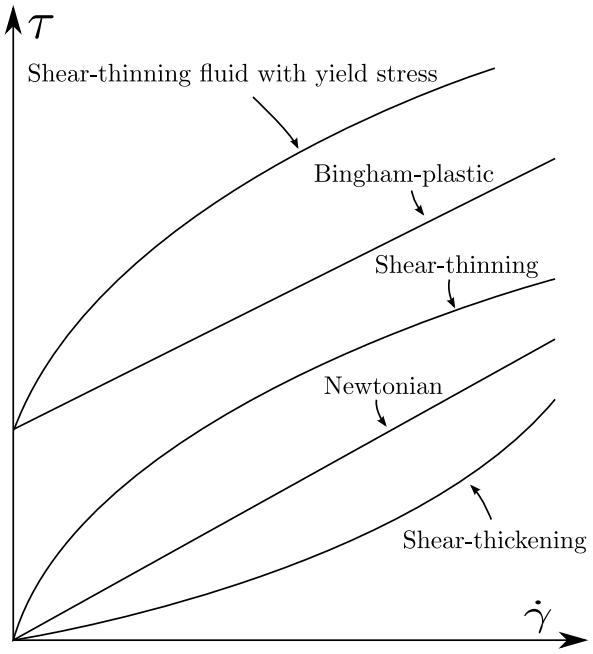

Figure 3.2 *Rheograms of time-independent fluids*

The shear stress experienced by a generalised Newtonian fluid is written as a product of viscosity, and shear rate:

$$\tau = \mu\left(\dot{\gamma}\right)\dot{\gamma}, \tag{3.9}$$

where $\mu\left(\dot{\gamma}\right)$ indicates that viscosity is a function of shear rate only. Numerous different viscosity models exist to express the relationship between shear rate and viscosity. The most commonly used models in industry and academia are listed here.

Power-law model

Power-law model uses two rheological constants to model the viscosity:

$$\mu = K\dot{\gamma}^{n-1}, \tag{3.10}$$

where K is called the consistency coefficient and n the power-law index. Both K and n are determined experimentally from rheological measurements.

The power-law index n determines the viscosity behaviour of the fluid:

- $n < 1$ shear-thinning behaviour
- $n = 1$ Newtonian fluid
- $n > 1$ shear-thickening behaviour

The power-law model is the most used viscosity model of shear-thinning and shear-thickening fluids. Viscosity parameters K and n can be found from literature for a wide range of fluids. The main drawback of the power-law model is that the power-law relationship most often only holds true for a certain shear rate range. For very low and high shear rates the viscosity curve of a typical power-law fluid deviates from the power-law model.

Herschel-Bulkley model

Herschel-Bulkley model is used for fluids with yield stress that exhibit shear thinning or thickening behaviour.

$$\begin{cases} \mu = \frac{\tau_y}{\dot{\gamma}} + K\dot{\gamma}^{n-1} & \dot{\gamma} > \dot{\gamma}_{crit} \\ \mu = \mu_0 & \dot{\gamma} < \dot{\gamma}_{crit} \end{cases} \tag{3.11}$$

where τ_y is the yield stress of the fluid and $\dot{\gamma}_{crit}$ is the critical shear rate.

Due to the combination of shear-thinning and yielding behaviour, the H-B model is often used for fibre suspension flows. The critical shear rate $\dot{\gamma}_{crit}$ is not a material property, but a mathematical cut-off value to prevent unrealistically high viscosity values, if shear rate approaches zero. Computational fluid dynamics software OpenFOAM uses a slightly different formulation for Herschel-Bulkley model:

$$\nu = \min\left(\nu_0 \quad , \quad \frac{\tau_y}{\dot{\gamma}} + K\dot{\gamma}^{n-1}\right), \tag{3.12}$$

where ν is the kinematic viscosity of the fluid and the critical shear-rate is replaced with a cut-off viscosity value ν_0. Kinematic viscosity is the dynamic viscosity of the fluid divided by density of the fluid: $\nu = \mu/\rho$.

Bird-Carreau viscosity model

The Bird-Carreau viscosity model takes into account deviations from the power-law model, when shear rates reach very low or high values. The Bird-Carreau viscosity model is expressed in the following way:

$$\mu = \mu_\infty + (\mu_0 - \mu_\infty)\left[1 + (K\dot{\gamma})^a\right]^{(n-1)/a}, \tag{3.13}$$

where μ_{inf} is the limiting viscosity for high shear rate, μ_0 is the limiting viscosity for low shear rate and a is a model constant which typically has a fixed value of 2.

3.3 Three dimensional shear rate

For generalised Newtonian fluid viscosity models, the viscosity is dependent on shear rate $\dot{\gamma}$ only. In a simple geometry, such as the geometry in figure 3.1, the shear rate value can easily be evaluated from the strain rate tensor S_{ij}.

For three dimensional cases, the strain rate tensor is more complex and the evaluation of shear rate is more difficult. Most CFD-codes and rheological studies use the following expression for shear rate:

$$\dot{\gamma} = \sqrt{2}\left(S_{ij} : S_{ij}\right)^{1/2}, \tag{3.14}$$

where $S_{ij} : S_{ij}$ is the double-dot product of the strain rate tensor.

4. TURBULENT FLOW

Turbulence can be observed in everyday environment. Smoke rising from a chimney and a wake behind a ship are both common examples of turbulent flows. Turbulent flows are characterised by unsteady chaotic motions over a wide range of different time and length scales. Most flows in industrial applications and nature are turbulent. Understanding turbulent phenomena is essential for designing and optimizing geometries in process equipment.

Turbulence can be beneficial to the system: Industrial mixers rely on increased diffusivity caused by turbulent motions to rapidly mix chemical species. Golf balls have dimples added to them because the turbulent boundary layer created by the added surface roughness reduces the overall drag force of the ball, when compared to a smooth golf ball.

On the other hand, processes involving turbulent flows have a degree of uncertainty in them. Chaotic effects such as vortices and other large-scale turbulent structures make prediction of turbulent flows difficult. Turbulence also wastes pumping energy in fluid transportation (except for fibre suspension flows in the turbulent regime), as part of the pumping power is transferred into turbulent motions.

4.1 Transition

When deriving the equations in Chapter 2, laminar flow was assumed. With increasing flow velocity, small perturbations in the flow are amplified, causing irregular chaotic motions to arise in the flow field. These flow instabilities are due to the non-linear inertial terms in the momentum-equations, and they occur at a certain Reynolds number:

$$Re = \frac{inertial\ forces}{viscous\ forces} = \frac{UL}{\nu}, \tag{4.1}$$

where U is the velocity of the flow, L a typical length scale of the flow and ν the kinematic viscosity of the fluid. Reynolds number is a dimensionless group that

is used to analyse turbulent flows. It is defined as the ratio of inertial forces to viscous forces. A large Reynolds number means that inertial forces dominate the flow behaviour and vice versa.

Transition from a laminar flow into a turbulent one for a Newtonian fluid happens when the Reynolds number of the flow is in the range of 2000. Laminar flow may be maintained even for larger Reynolds numbers if flow conditions are strictly controlled.

For non-Newtonian fluids, the transition criteria has been under extensive research. The Reynolds number for a non-Newtonian fluid flow is more difficult to determine, because the viscosity of the fluid is not constant. A commonly used Reynolds number for power-law fluids is the generalized Reynolds number proposed by Mentzner and Reed [24], which takes into account the shear index n and the consistency parameter K of the fluid. The Mentner-Reed Reynolds number for pipe flow is presented in equation 4.2:

$$Re_{genPL} = \frac{\rho D^n u^{2-n}}{K\left((3n+1)/(4n)\right)^n 8^{n-1}}, \tag{4.2}$$

where ρ is the density of the fluid and D is the pipe diameter and u the bulk flow velocity.

A generalized Reynolds number for Herschel-Bulkley fluids was derived for pipe flows by Madlener et al [21].

$$Re_{genHB} = \frac{\rho D^n u^{2-n}}{(\tau_0/9)(D/u)^n + K\left((3m+1)/(4m)\right)^m 8^{n-1}}, \tag{4.3}$$

$$\text{with } m = \frac{nK(8u/D)^n}{\tau_0 + K(8u/D)^n}, \tag{4.4}$$

where τ_0 is the yield stress of the fluid. However, there is no clear Reynolds number range to mark the transition from laminar to turbulent flow in non-Newtonian fluids.

4.2 Scales of turbulent motion

Multiple length scales can be identified from turbulent flows. Length scales in the flow range from the width of the flow geometry, to very small eddies present in the flow. Richardson was the first to introduce the concept of energy cascade [31]. The main idea of the energy cascade concept is that turbulence consists of eddies of different sizes and turbulent energy is transferred from the larger eddies to the smaller ones. The energy transfer process eventually ends in the smallest eddies of the flow, which are dissipated by molecular viscosity.

Eddies are turbulent motions in the flow which have a length-scale l, a characteristic velocity $u(l)$ and a time-scale $\tau(l) = l/u(l)$. The largest eddies of the flow extract energy from the mean flow and are virtually unaffected by molecular viscosity, and contain most of the turbulent kinetic energy k. The large eddies have a clear orientation depending on the boundary conditions of the flow, and are the main source of anisotropy in turbulent flows.

An eddy of a length l can be associated with a wavenumber $\kappa = 2\pi/\lambda$, where λ is the wavelength of the eddy. The energy cascade is represented as the turbulent spectral energy as a function of eddy wavenumber $E(\kappa)$. A diagram of the turbulent energy spectrum is depicted in figure 4.1.

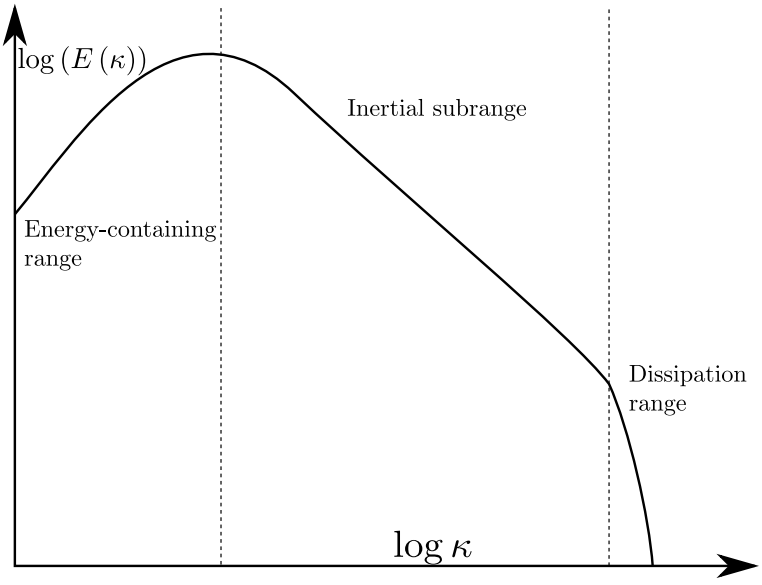

Figure 4.1 *Energy spectrum of turbulence*

The smallest eddies are dissipated into heat by viscous forces. The length-, velocity- and time-scales of the smallest eddies are named after their founder as the Kolmogorov scales:

$$l_\eta = \left(\nu^3/\varepsilon\right)^{1/4}, \tag{4.5}$$

$$u_\eta = (\varepsilon\nu)^{1/4}, \tag{4.6}$$

$$\tau_\eta = (\nu/\varepsilon)^{1/2}, \tag{4.7}$$

where ε is the viscous dissipation in $[m^2/s^3]$. Small eddies are considered to be isotropic and adapt themselves to the energy-transfer rate set by the large eddies. Smallest eddies are found in the dissipation range of the energy turbulent energy spectrum in figure 4.1.

The Inertial subrange is an eddy wavenumber range, where energy drops with a slope of $-\frac{5}{3}$. In the Inertial subrange, viscous effects are still negligible, hence the scale of eddies in this range are independent of ν. Energy is transferred from the inertial subrange into the dissipation range at a rate of ε, where viscous dissipation finally dissipates the smallest eddies containing the least energy [3].

4.3 Reynolds Averaged Equations for turbulent flow

Turbulent flows have a degree of uncertainty in them. When measuring the velocity of a turbulent flow at a certain point, the measurement would fluctuate around a mean value. A typical measurement point measurement of a turbulent velocity signal u is presented in figure 4.2.

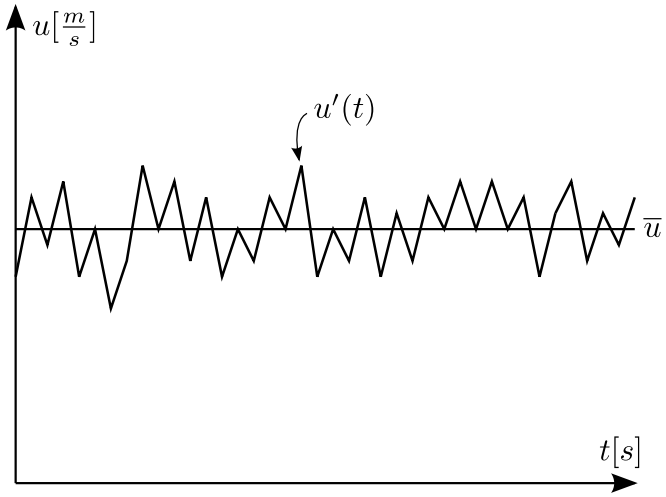

Figure 4.2 *Typical point velocity measurement in turbulent flow*

In engineering applications the interest often lies in the mean qualities of the turbulent flow field. In order to form the equations for the mean qualities of the flow,

first a tool referred to as *Reynolds decomposition* is introduced, where a turbulent flow variable is decomposed into its mean and fluctuating part.

For velocity u_i the Reynolds decomposition can be written in the following way:

$$u_i = \overline{u}_i + u_i', \tag{4.8}$$

where $\overline{u}_i$ is the mean velocity and u_i' the fluctuating part of the velocity.

For a scalar variable ϕ such as temperature or concentration of species the decomposition is exactly the same:

$$\phi = \overline{\phi} + \phi', \tag{4.9}$$

now $\overline{\phi}$ is the mean part and ϕ' the fluctuating component.

The intensity of turbulence in the flow is often expressed via turbulent kinetic energy k, which is defined as the root mean square of the velocity fluctuations:

$$k = \frac{1}{2}\left(\overline{(u_x')}^2 + \overline{(u_y')}^2 + \overline{(u_z')}^2\right), \tag{4.10}$$

where u_x', u_y' and u_z' are the fluctuating velocities in x, y and z directions respectively.

In order to use Reynolds decomposition presented in equations 4.8 and 4.9 on the conservation equations, the following Reynolds conditions have to be enforced on the averaging process:

1. $\overline{f+g} = \overline{f} + \overline{g}$
2. $\overline{af} = a\overline{f}$, where $a = constant$
3. $\overline{\overline{f}g} = \overline{f}\,\overline{g}$
4. $\overline{f'} = 0$ (Reynolds average of a fluctuation is zero)
5. $\overline{\overline{f}g'} = 0$

The decomposed variables we are interested in are velocity, pressure, viscous stress tensor and the rate-of-strain tensor:

$$\begin{aligned} u_i &= \overline{u_i} + u_i' \\ p &= \overline{p} + p' \\ \sigma_{ij} &= \overline{\sigma_{ij}} + \sigma_{ij}' \\ S_{ij} &= \overline{S_{ij}} + S_{ij}' \end{aligned} \tag{4.11}$$

The turbulent equations for mean mass conservation and mean momentum conservation are obtained by substituting the decomposed variables into equations 3.1 and 3.3. To highlight the process of averaging, the convective term in 3.3 is written in its conservative form:

$$\rho u_j \frac{\partial u_i}{\partial x_j} = \rho \frac{\partial u_i u_j}{\partial x_j} - \rho u_i \frac{\partial u_j}{\partial x_j} \tag{4.12}$$

Using the continuity equation 3.1 in equation 4.12 the latter term in the right hand side of the equation goes to zero.

The decomposed velocity can now be substituted into the conservative form using equation 4.8:

$$\rho \frac{\partial}{\partial x_j} \left(\overline{u_i u_j}\right) = \rho \frac{\partial}{\partial x_j} \left(\overline{\overline{u}_i \overline{u}_j + \overline{u}_i u_j' + \overline{u}_j u_i' + u_i' u_j'}\right) \tag{4.13}$$

Using the rules for Reynolds decomposition presented before, equation 4.13 can be written in the following form:

$$\rho \frac{\partial}{\partial x_j} \left(\overline{u_i u_j}\right) = \rho \overline{u}_j \frac{\partial \overline{u}_i}{\partial x_j} + \rho \frac{\partial \overline{u_i' u_j'}}{\partial x_j}, \tag{4.14}$$

where $\overline{u_i' u_j'}$ are called the Reynolds stresses. The Reynolds stresses originate from the fluctuating velocity field and are responsible for the additional momentum transfer in turbulent flows.

Conservation equations 3.1 and 3.3 can now be written for the Reynolds averaged turbulent flow:

$$\nabla \cdot \overline{u}_i = 0 \tag{4.15}$$

$$\frac{\partial}{\partial t} \left(\rho \overline{u}_i\right) + \rho \overline{u}_j \frac{\partial \overline{u}_i}{\partial x_j} = -\frac{\partial \overline{p}}{\partial x_i} + \frac{\partial \overline{\sigma}_{ij}}{\partial x_j} + \mathbf{T} - \rho \frac{\partial \overline{u_i' u_j'}}{\partial x_j}, \tag{4.16}$$

In the simulation part of this work, there are no external forces to be included into the body-force vector **T**, so it is eliminated from equation 4.16. Substituting equations 3.4, 3.5 and kinematic viscosity $\nu = \mu/\rho$ into equation 4.16 gives the final form for momentum conservation equation in a turbulent flow of a Newtonian fluid, with no body-forces:

$$\frac{\partial \overline{u}_i}{\partial t} + \overline{u}_j \frac{\partial \overline{u}_i}{\partial x_j} = -\frac{1}{\rho}\frac{\partial \overline{p}}{\partial x_i} + \nu \frac{\partial^2 \overline{u}_i}{\partial x_j^2} - \frac{\partial \overline{u_i' u_j'}}{\partial x_j}, \tag{4.17}$$

Reynolds stresses add 6 more unknown terms into the momentum equations. In order to solve equations 4.15 and 4.17 6 more equations are needed. This is known as the closure problem of turbulence.

4.4 Boussinesq Eddy Viscosity

Newton's law of viscosity described in equation 3.4 connects the viscous stress tensor and the rate-of-strain tensor through molecular viscosity. In a similar fashion, the simplest turbulence models relate the Reynolds stresses to the average rate-of-strain $\overline{S_{ij}}$. In the turbulent-viscosity hypothesis, the Reynolds stresses are expressed in the following way:

$$-\rho \overline{u_i' u_j'} = 2\mu_t \overline{S}_{ij} - \frac{2}{3}\rho \delta_{ij} k, \tag{4.18}$$

where μ_t is called *eddy-viscosity* and k is the turbulent kinetic energy from equation 4.10. Equation 4.18 is known as the *Boussinesq eddy viscosity hypothesis* and is the main assumption of many turbulence models.

For numerical reasons it is beneficial to introduce effective viscosity ν_{Eff} as:

$$\nu_{Eff} = \nu_{app}\left(\dot{\gamma}\right) + \nu_t, \tag{4.19}$$

where ν_t is the turbulent kinematic viscosity $\nu_t = \mu_t/\rho$ and $\nu_{app}\left(\dot{\gamma}\right)$ is the apparent molecular viscosity, computed from the viscosity model. Equation 4.19 is the main assumption made in the modelling of turbulent pulp-fibre suspension. **The molecular and turbulent viscosities are modelled separately and combined as one effective viscosity in the momentum equation.**

Substituting equation 3.5, 4.18 and 4.19 to equation 4.17 yields a simple form for

turbulent momentum equation:

$$\frac{\partial \overline{u}_i}{\partial t} + \overline{u}_j \frac{\partial \overline{u}_i}{\partial x_j} = -\frac{1}{\rho}\frac{\partial \overline{p}^*}{\partial x_i} + \nu_{eff}\frac{\partial^2 \overline{u}_i}{\partial x_j^2}, \tag{4.20}$$

where $\overline{p}^*$ is the modified pressure, $\overline{p}^* = \overline{p} + \frac{2}{3}\rho\delta_{ij}k$. Using a modified pressure difference does not affect the solution significantly. The magnitude of turbulent stresses vary in the flow. Highest stresses are found in areas where high shearing rates and velocities are present. Numerous different eddy viscosity models exist in literature. These models are typically categorized based on the number of partial differential equations in the model.

4.4.1 Two-equation eddy viscosity models

Two-equation models are commonly used in industrial applications to model the mean qualities of the turbulent flow field. These models are called two-equation models because they solve two additional transport equations to model the eddy viscosity.

The standard $k - \varepsilon$ model

The $k - \varepsilon$ turbulence model is the most common two-equation model to simulate turbulent flows. The eddy viscosity of the flow is determined by solving two additional transport equations for k and ε. The standard $k - \varepsilon$ model was developed for fully turbulent flows where molecular viscosity is assumed to be negligible. For this reason the equations in the standard $k - \varepsilon$ model cannot be integrated all the way to the wall. If one wishes to integrate the $k - \varepsilon$ model equations all the way to the wall, special damping functions need to be added to the equations to account for the low Reynolds number near the wall. The standard $k - \varepsilon$ turbulence model is known as a high Reynolds number turbulence model, which is suitable for free shear flows, but performs poorly on flows with separation.

The equation for the total kinetic energy budget of the flow $K + k$ can be obtained by multiplying the momentum equation with u_i and performing the Reynolds decomposition. The turbulent kinetic energy balance can then be obtained from the total energy budget, by subtracting the mean kinetic energy K of the flow from the total energy budget. This requires some substantial algebra and it is skipped here.

The $k-\varepsilon$-model uses k and ε to define the eddy viscosity:

$$\nu_t = C_\mu \frac{k^2}{\varepsilon}, \tag{4.21}$$

where C_μ is a model constant. Transport equations for k and ε are presented in equations 4.22 and 4.23.

$$\frac{\partial k}{\partial t} + \frac{\partial}{\partial x_i}\left(k\overline{u}_i\right) = \frac{\partial}{\partial x_j}\left[\left(\nu_{app} + \frac{\nu_t}{\sigma_k}\right)\frac{\partial k}{\partial x_j}\right] + P_k - \varepsilon + S_k \tag{4.22}$$

$$\frac{\partial \varepsilon}{\partial t} + \frac{\partial}{\partial x_i}\left(\varepsilon\overline{u}_i\right) = \frac{\partial}{\partial x_j}\left[\left(\nu_{app} + \frac{\nu_t}{\sigma_\varepsilon}\right)\frac{\partial \varepsilon}{\partial x_j}\right] + C_{1\varepsilon}\frac{\varepsilon}{k}P_k - C_{2\varepsilon}\frac{\varepsilon^2}{k} + S_\varepsilon \tag{4.23}$$

where P_k is the production of turbulent kinetic energy:

$$P_k = 2\nu_t \overline{S}_{ij}\overline{S}_{ij}, \tag{4.24}$$

and S_k is the source term for k and S_ε is the source term for ε. The model constants for the standard $k-\varepsilon$-model are defined in table 4.1.

Table 4.1 *Constants for standard $k-\varepsilon$ turbulence model*

$C_\mu = 0.09$	$\sigma_k = 1.00$	$\sigma_\varepsilon = 1.30$	$C_{1\varepsilon} = 1.44$	$C_{2\varepsilon} = 1.92$

The $k-\omega$ SST model

The $k-\omega$ turbulence model uses turbulence frequency $\omega = \frac{\varepsilon}{k}$ as the second variable to determine eddy viscosity. The $k-\omega$ model is a low Reynolds number model, which means that the equations can be integrated to the wall without the use of damping functions. The most commonly used version of the $k-\omega$ model is the shear-stress transport model by Menter, [23] known as the $k-\omega$ SST model. The SST model uses blending functions to change between $k-\omega$ and $k-\varepsilon$ formulations based on the distance from wall regions.

The transport equations for k and ω in the SST formulation are presented as follows:

$$\frac{\partial k}{\partial t} + \frac{\partial}{\partial x_i}\left(k\overline{u}_i\right) = \frac{\partial}{\partial x_j}\left[\left(\nu_{app} + \nu_t\sigma_k\right)\frac{\partial k}{\partial x_j}\right] + \widetilde{P_k} - \beta^* k\omega + S_k \tag{4.25}$$

$$\frac{\partial \omega}{\partial t} + \frac{\partial}{\partial x_i}\left(\omega\overline{u}_i\right) = \frac{\partial}{\partial x_j}\left[\left(\nu_{app} + \nu_t\sigma_\omega\right)\frac{\partial \omega}{\partial x_j}\right] + \alpha S^2 - \beta\omega^2 + 2\left(1 - F_1\right)\frac{\sigma_{\omega 2}}{\omega}\frac{\partial k}{\partial x_i}\frac{\partial \omega}{\partial x_i}, \tag{4.26}$$

where F_1 is a blending function defined by:

$$F_1 = \tanh\left(\left[\min\left[\max\left(\frac{\sqrt{k}}{\beta^*\omega y}, \frac{500\nu}{y^2\omega}\right), \frac{4\sigma_{\omega 2}k}{CD_{k\omega}y^2}\right]^4\right]\right), \tag{4.27}$$

where y is the distance to the nearest wall and β^* and $\sigma_{\omega 2}$ are model constants. F_1 gains values between one and zero (tanh function). Far away from surfaces F_1 is equal to zero ($k-\varepsilon$), while near the walls F_1 is equal to one ($k-\omega$ model).

$CD_{k\omega}$ in equation 4.27 is defined by:

$$CD_{k\omega} = \max\left(2\sigma_{\omega 2}\frac{1}{\omega}\frac{\partial k}{\partial x_i}\frac{\partial \omega}{\partial x_i}, 10^{-10}\right) \tag{4.28}$$

The $k-\omega$ SST model uses the following formulation for the turbulent eddy viscosity:

$$\nu_t = \frac{a_1 k}{\max\left(a_1\omega, SF_2\right)}, \tag{4.29}$$

where S is the invariant measure of the strain rate. F_2 is a second blending function given by:

$$F_2 = \tanh\left[\left[\max\left(\frac{2\sqrt{k}}{\beta^*\omega y}, \frac{500\nu}{y^2\omega}\right)\right]^2\right] \tag{4.30}$$

In order to prevent unrealistic build-up of turbulence in stagnant regions of the flow, the production of turbulent kinetic energy $\widetilde{P_k}$ in the k equation of the SST model is limited:

$$\widetilde{P_k} = \min\left(P_k, 10 \cdot \beta^* k\omega\right), \tag{4.31}$$

where P_k is the production of turbulent kinetic energy from equation 4.24.

Constants in the SST model are computed as blend between the constants from the $k-\varepsilon$ and $k-\omega$ models in the following manner:

$$\alpha = \alpha_1 F_1 + \alpha_2 \left(1 - F_1\right) \tag{4.32}$$

The constants for the $k-\omega$ SST model are listed in table 4.2.

Table 4.2 *Constants for $k-\omega$ SST turbulence model*

$\beta^* = 0.09$	$\alpha_1 = 5/9$	$\alpha_2 = 0.44$	$\sigma_{k1} = 0.85$	$\sigma_{\omega 1} = 0.5$
$\beta_1 = 3/40$	$\beta_2 = 0.0828$	$\sigma_{k2} = 1$	$\sigma_{\omega 2} = 0.856$	$a_1 = 0.31$

4.5 Turbulence modelling for Generalized Newtonian Fluids

There are numerous applications in industry, where non-Newtonian fluids are subjected to turbulent flow conditions. Drilling fluids in drill stings, oils in heat exchangers and bearings and pulp-fibre suspension in slushers are examples of non-Newtonian turbulent flow. When compared to Newtonian fluids, non-Newtonian fluids have a decreased turbulent intensity normal to the wall. This effect causes the friction losses of some non-Newtonian flows to be lower, when compared to Newtonian flows. On the other hand, the streamwise turbulent fluctuations for non-Newtonian flows can be even higher than those of Newtonian ones [13].

Pinho [30] and Gavrilov et al. [12] [13] have developed Reynolds averaged turbulence models that take into account molecular viscosity fluctuations due to turbulent motions.

Gavrilov noted that in order to correctly model turbulent flows of non-Newtonian fluids two problems need to be solved:

1. Modeling of the apparent molecular viscosity so that it is connected to the turbulent velocity fluctuations of the flow
2. Modeling of correlations not found in Newtonian flows

In Gavrilov's work, a turbulence model for power-law fluids was proposed, based on the $\zeta - f$ model by Durbin [9] and modifications by Hanjalic et al. [14]. The system of equations for the model is presented in equations 4.33 to 4.37.

$$\rho \mathbf{U} \cdot \nabla (\mathbf{U}) = -\nabla p + \nabla \cdot [2 (\mu + \mu_t) \mathbf{S}] + \nabla \cdot \tau_N, \tag{4.33}$$

$$\rho \mathbf{U} \cdot \nabla (k) = \nabla \cdot [(\mu + \mu_t/\sigma_k) \nabla k] + P - \rho\varepsilon + (D_N + \Gamma_N), \tag{4.34}$$

$$\rho \mathbf{U} \cdot \nabla (\varepsilon) = \nabla \cdot [(\mu + \mu_t/\sigma_\varepsilon) \nabla \varepsilon] + \frac{1}{T} (C_{\varepsilon 1} P - C_{\varepsilon 2} \rho\varepsilon) + E_N, \tag{4.35}$$

$$\rho \mathbf{U} \cdot \nabla (\zeta) = \nabla \cdot [(\mu + \mu_t/\sigma_\zeta) \nabla \zeta] + \rho f - \frac{\zeta}{k} P - \frac{\zeta}{k} (D_N + \Gamma_N), \tag{4.36}$$

$$L^2 \nabla^2 f - f = \frac{1}{T} \left(\zeta - \frac{2}{3} \right) \left(C_{1f} - 1 + C_{2f} \frac{P}{\rho\varepsilon} \right), \tag{4.37}$$

where ζ is dimensionless turbulent fluctuation normal to streamlines, and f an elliptic relaxation function. The additional non-Newtonian turbulent stress is added through an non-Newtonian stress tensor τ_N in the momentum equation. Viscosity fluctuations due to turbulent motions are taken into account throughout the model in the Reynolds averaging process and the calculation of shear rate $\dot{\gamma}$ is also modified.

The additional non-Newtonian stress tensor τ_N is defined as:

$$\tau_N = C_N 2 \mu_N \overline{S}_{ij}, \tag{4.38}$$

where μ_N is the polymeric viscosity:

$$\mu_N = (n-1) \rho\varepsilon / \dot{\gamma}^2, \tag{4.39}$$

The model adds three different terms into the system of equations that need to be evaluated. The additional work of non-Newtonian stresses:

$$\Gamma_N = -C_N \mu_N S^2 \tag{4.40}$$

Additional turbulent diffusion through viscosity fluctuations:

$$D_N = \nabla \cdot \left[C_N \frac{(n-1) \mu S^2}{\dot{\gamma}^2} \nabla k \right] \tag{4.41}$$

Production of dissipation of turbulent kinetic energy E_N:

$$E_N = C_{\varepsilon N} \frac{C_{\varepsilon 1}}{T} \left(D_N + \Gamma_N \right) \tag{4.42}$$

The average apparent viscosity is evaluated through a system of non-linear equations:

$$\mu = k_v \left(\dot{\gamma}^2 \right)^{\frac{n-1}{2}}, \quad \dot{\gamma}^2 = S^2 + \rho, \varepsilon/\mu, \tag{4.43}$$

where k_v is the consistency index of the power-law fluid. Additionally, the term $\rho\varepsilon/\mu$ in the shear rate evaluation is the contribution of turbulent fluctuations.

An attempt was made to program the Gavrilov model into OpenFOAM environment, but it was found to be too time-consuming and difficult given the scope of this work. The Gavrilov model requires linking of viscosity and turbulence models in a way does not well suit the standard method of how turbulence models are implemented in OpenFOAM. The model was presented here in order to highlight the future framework and difficulties present in Reynolds averaged modeling of non-Newtonian flows. Full details of the model can be found in [13].

4.6 Large Eddy Simulations

Large-eddy simulations (LES) separate scales of turbulent motions to large scales and subgrid scales. The large-scale motions of the eddies are resolved directly, while the small scale motions of the turbulent flow field are modelled and their effect is added to the large scale motions through subgrid models. The resolved scales and subgrid scales are separated by using filtering functions. Figure 4.3 depicts a simple scale separation operator in physical space and Fourier space.

The interest in Large-eddy simulations has increased in the recent years. The computational requirements of LES are becoming easier to meet for simple flow problems. The benefits of LES are that the unsteady turbulence motions of the flow are revealed from the simulation and large scale turbulence can be resolved directly. Flow situations where large-scale turbulent vortices have a major effect on the flow field such as combustion chambers, pipe bends and vortex shedding behind bodies are good applications for Large-eddy simulations [37].

Hybrid LES-RANS models have been developed, which offer some advantages of

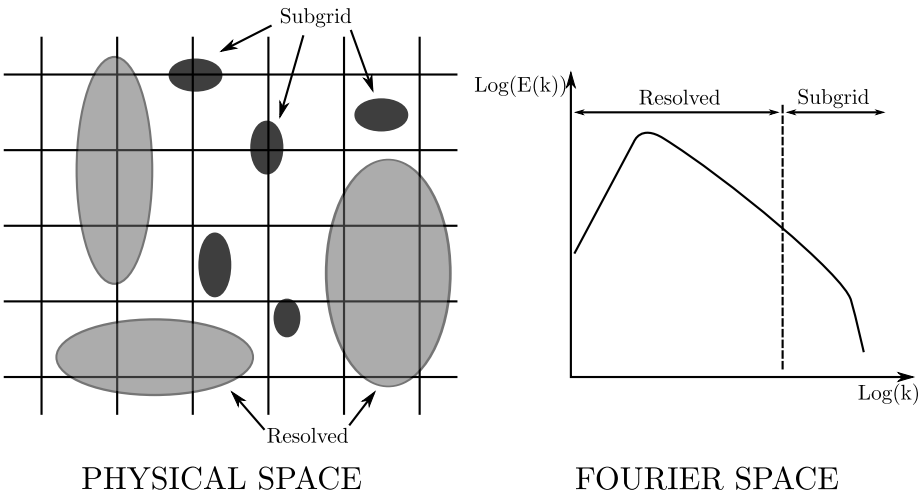

Figure 4.3 *Schematic of a simple scale separation operator [32]*

the LES approach, but at a reduced computational cost. These are *Detached Eddy Simulations* (DES) and *Scale-Adaptive-Simulations* (SAS). DES uses the RANS formulation in the attached boundary layer and LES approach in the separated flow regions, where the turbulent length scale exceeds the grid spacing dimension. SAS attempts to avoid the issue of grid-induced turbulence by not using explicit grid length scale in the transition from RANS-mode to LES-mode [41].

4.7 Boundary layers

When considering a wall-bounded turbulent flow case such as a pipe flow or channel flow, the no-slip condition at solid walls requires that the velocity component tangential to the wall normal is the same as the velocity of the wall. If the wall is stationary, the velocity of the flow is also zero at the surface. Near solid surfaces, visocus forces dominate and the flow creates a thin layer known as the boundary layer, where the flow velocity rapidly changes from the freestream value to zero at the walls. Figure 4.4 depicts the development of boundary layer thickness δ over a flat plate.

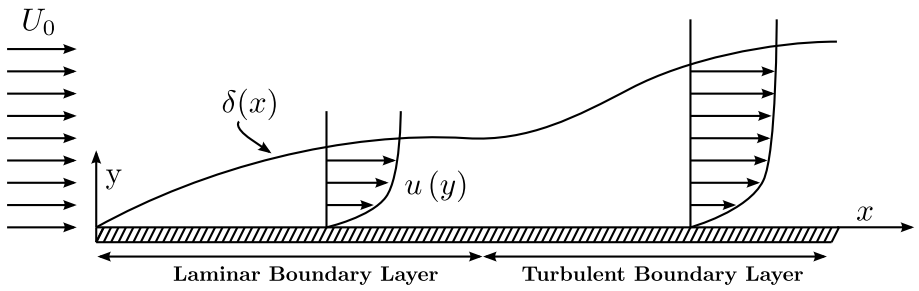

Figure 4.4 *Boundary layer development over a flat plate*

Close to the wall, the important parameters affecting the velocity of the flow are viscosity ν and wall shear stress τ_w. The viscous velocity scale, defined by wall shear stress and commonly known as friction velocity u_τ, is used in boundary layer analysis:

$$u_\tau = \sqrt{\frac{\tau_w}{\rho}} \tag{4.44}$$

The viscous length scale can then be expressed using dimensional analysis:

$$\delta_\nu = \frac{\nu}{u_\tau} \tag{4.45}$$

The distance from the wall is measured in wall units:

$$y^+ = \frac{y}{\delta_\nu}, \tag{4.46}$$

where y is the distance from the wall in meters.

Boundary layers are separated into different regions on the basis of y^+. Near the wall, at $y^+ < 50$ exists a *viscous wall region*, where molecular viscosity dominates the flow behaviour. In the *outer layer* where $y^+ > 50$, the direct effect of molecular viscosity becomes negligible.

Note that this may not be the case in non-Newtonian fluids as the molecular viscosity is dependant on the shear experienced by the fluid, which in turn makes the effect of molecular viscosity on the mean flow profile more complicated than that of Newtonian fluids.

The near wall-region of the flow is analysed by using non-dimensional velocity u^+, which is a function of y^+ only. Dimensionless velocity u^+ is defined as follows:

$$u^+ = \frac{U}{u_\tau}, \tag{4.47}$$

where U is the mean velocity of the flow.

Right next to a solid wall, in a region known as the *viscous sublayer*, the relationship between u^+ and y^+ is linear. In this region $u^+ = y^+$ holds, as long as $y^+ < 5$. Significant departure from this linear relation begins when $y^+ > 12$.

Moving away from the wall, a logarithmic relation between $y+$ and u^+ is observed. This is known as the logarithmic law of the wall by von Kármán:

$$u^+ = \frac{1}{\kappa} \ln y^+ + B, \tag{4.48}$$

where B is a constant and κ is the von Kármán constant. Some variation for these values exists in literature but typically used values for the constants are:

$$\kappa = 0.41, \quad B = 5.2 \tag{4.49}$$

The log-law is valid for values of $y^+ > 30$. Deviation from the log-law will begin depending on the flow, typically at y^+ values of 500-1000 [3].

In the *outer layer*, the effect of viscosity ν to the flow is negligible. The velocity defect law, which states that the difference between the freestream velocity and mean velocity depends on y/δ only:

$$\frac{U_0 - U}{u_\tau} = F_D \left(\frac{y}{\delta} \right), \tag{4.50}$$

where F_D is a function which has no universal form, but instead depends on the flow conditions.

4.7.1 Wall functions

The complex behaviour of the velocity profile in the turbulent boundary layer makes modelling of Reynolds averaged wall bounded turbulent flows difficult. The transport equations for k, ϵ and ω have to be modified, to take into account the presence of walls, so that the velocity in the boundary layer is correct. This is often done by using wall functions, which constrain and modify the values of turbulent fields near solid walls.

The $k - \omega$ SST turbulence model presented in equations 4.25 4.26, can use the following wall function for determining ω near walls:

$$\omega = \sqrt{\omega_{vis}^2 + \omega_{log}^2}, \tag{4.51}$$

where ω_{vis} is ω in the viscous wall region and is defined in the following way:

$$\omega_{vis} = \frac{6.0\nu}{\beta_1 y^2}, \tag{4.52}$$

where y is the distance from the wall and β_1, ν the kinematic viscosity at the wall and β_1 is a model constant from table 4.2.

ω_{log} in equation 4.51 is ω in the log-law region, which is evaluated through:

$$\omega_{log} = \sqrt{\frac{k}{\beta^{*0.25}\kappa y}}, \tag{4.53}$$

where β^* is a model constant from table 4.2.

The wall-function approach used in the $k-\omega$ SST model is robust. The grid spacing in the near-wall region does not have a significant effect to the solution, as equation 4.51 creates a continuous curve for ω regardless of the near-wall grid refinement. The robustness of the wall-treatment for modelling turbulent flows in industrial applications is extremely beneficial, as there are no strict requirements for near-wall grid spacing.

For ν_t, a Spalding wall function was used in the simulation part of this work, which provides a continuous profile for kinematic turbulent viscosity at walls, based on velocity [36]. The kinematic turbulent viscosity near a wall is calculated in the following way:

$$\nu_t = \frac{u_\tau^2}{\frac{\partial u}{\partial y}} - \nu, \tag{4.54}$$

where u_τ is evaluated through:

$$u_\tau = u_t + \frac{f}{df}, \tag{4.55}$$

where f and df are functions based on distance from wall and flow velocity. u_t in equation 4.55 is evaluated through:

$$u_t = \sqrt{(\nu_t + \nu)\frac{\partial u}{\partial y}}, \tag{4.56}$$

where $\frac{\partial u}{\partial y}$ is the velocity gradient normal to the wall. Functions f and df in equation 4.55 are defined in the following way:

$$f = -\frac{u_t y}{\nu} + \frac{u}{u_t} + \frac{1}{E}\left(C_{f_{kU}} - \frac{1.0}{6.0}C_{kU}^3\right), \tag{4.57}$$

$$df = \frac{y}{\nu} + \frac{u}{u_t^2} + \frac{1}{E}C_{kU}\frac{C_{f_{kU}}}{u_t}, \tag{4.58}$$

where C_{kU} and $C_{f_{kU}}$ are functions of u and E is a constant with a value of 9.8. Functions C_{kU} and $C_{f_{kU}}$ are defined in the following way:

$$C_{kU} = \min\left(\kappa\frac{u}{u_t}, 50\right), \tag{4.59}$$

$$C_{f_{kU}} = exp(C_{kU}) - 1 - C_{kU}\left(1 + \frac{1}{2}C_{kU}\right), \tag{4.60}$$

where κ is the Von Karman constant.

4.7.2 Boundary layers in turbulent fibre-suspension

Jäsberg [18] studied the near-wall behaviour of turbulent pulp fibre suspension and found that, when u^+ plotted against $\ln y^+$ the flow curve forms a S-shaped curve instead of a straight line as in the Newtonian case. The modified law of the wall is expressed in the following way:

$$u^+ = \frac{1}{\kappa}\left(y^+\right) + B + \Delta u^+, \tag{4.61}$$

where Δu^+ is the additional term introduced to the modified log-law, which gets different values depending on the distance from the wall:

$$\Delta u^+ = \begin{cases} 0 & 0 < y^+ < y_L^+ \\ \frac{\alpha}{\kappa}\ln(\frac{y^+}{y_L^+}) & y_L^+ < y^+ < y_C^+ \\ \frac{\alpha}{\kappa}\ln(\frac{y^+}{y_L^+}) - \frac{\beta}{\kappa}\ln(\frac{y^+}{y_L^+}), & y_L^+ < y^+ < R^+ \end{cases} \tag{4.62}$$

where α, y_L^+ and y_H^+ are constants for a given suspension, while β and y_C^+ depend on the flow rate. Figure 4.5 depicts the near-wall dimensionless velocity profile of turbulent pulp-fibre suspension.

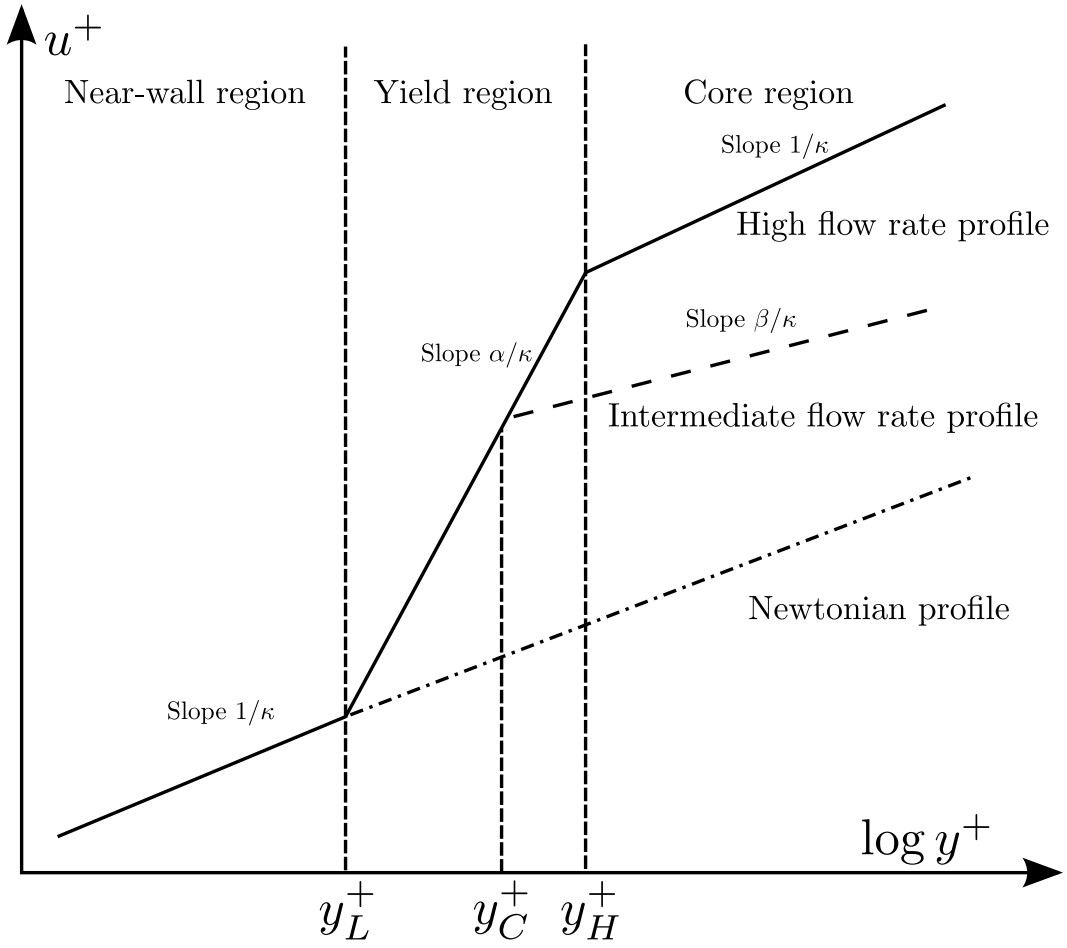

Figure 4.5 *The structure of dimensionless velocity profile in turbulent pulp-fibre suspension flow, adapted from [18]*

5. EXPERIMENTAL WORK

5.1 Jet experiment

An experimental jet apparatus was designed and constructed in Tampere University of Technology. The purpose of the apparatus was to visually observe a pulp-fibre suspension jet, and to measure the velocity profile of the formed suspension wall jet by using pulsed ultrasound velocimetry.

The pulp-fibre suspension jet was discharged into an acrylic glass tank with a wall thickness of 10 mm. At the top of the tank there is an rectangular opening the size of 180 mm times 280 mm. At the bottom of the tank there is an round outlet with a diameter of 40 mm. The height of the tank is 1.0 meter and the bottom 30 cm is angled, so that the suspension flows evenly out of the system without forming zones where the suspension would be at rest. The container was attached to a steel frame so that the top opening was pointing upwards towards the ceiling. The suspension jet was discharged into the tank from a round pipe with an inner diameter of 14.0 mm. The pipe entered the tank from the rectangular opening and was attached parallel with one of the tank walls. Figure 5.1 displays the dimensions of the experimental apparatus.

A Sulzer Ahlstar WP-20 pump was used to pump the fibre suspension through the system. The pump used in this experiment is a Sulzer Ahlstar WP-20. The electric motor driving the pump is connected to an ABB frequency converter. The volumetric flow rate of the suspension was measured with an Endress Hauser Proline Promag 50P electromagnetic flowmeter.

The pulp-fibre suspension was prepared by first soaking pieces of chemically prepared mass in water overnight and then mixing the suspension with an electric mixer before injecting it into the system. Final pulping was achieved by setting a high flow rate into the system for a set amount of time before conducting experiments.

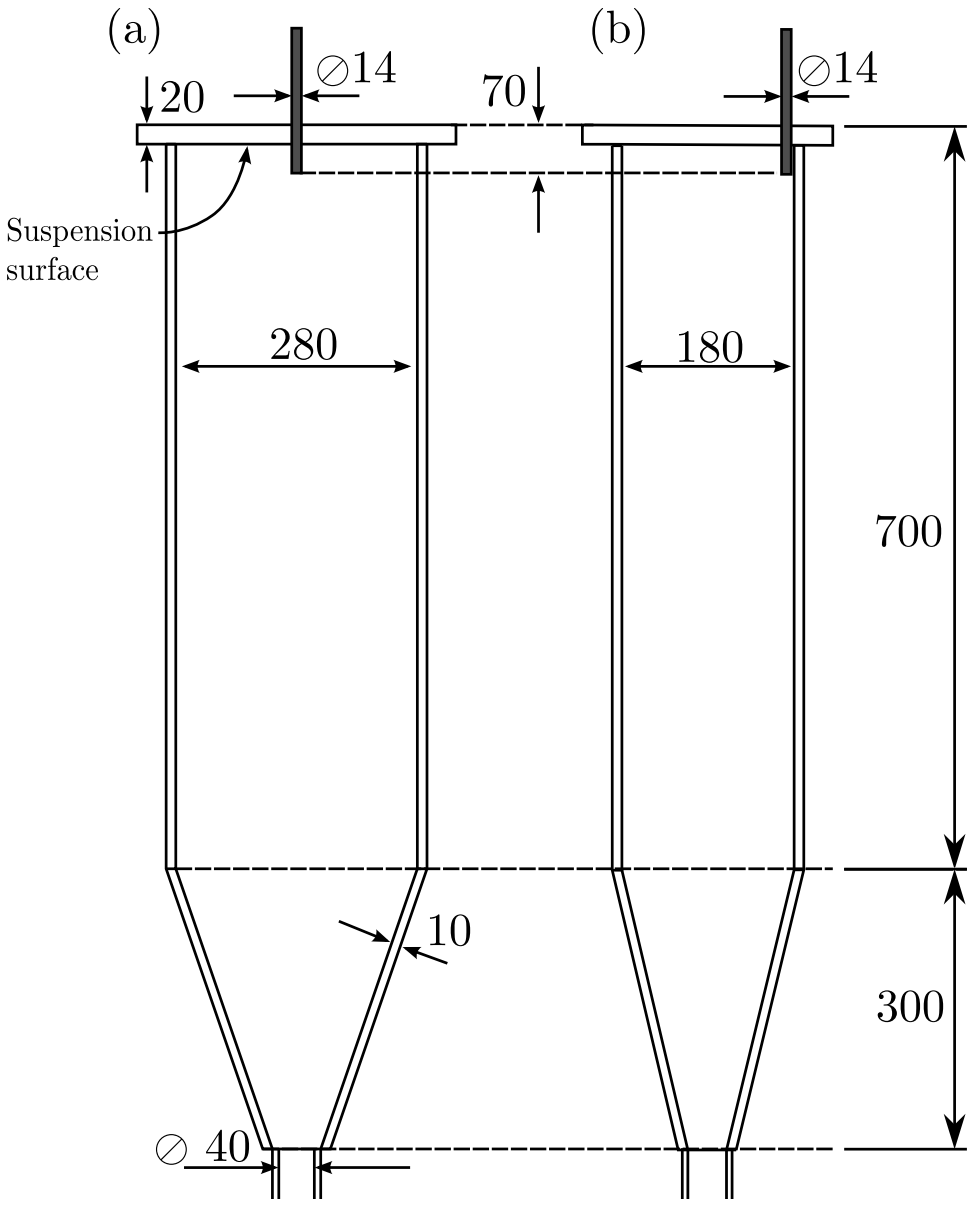

Figure 5.1 *Experimental setup (dimensions in mm)*

5.1.1 Wall jet structure

Turbulent wall jets have been widely researched for their great importance in engineering applications. Wall jet flows are present in heating, cooling and ventilation applications. A wall jet is formed when a jet discharges into ambient or slower medium next to a wall. A schematic of a plane wall jet is depicted in figure 5.2.

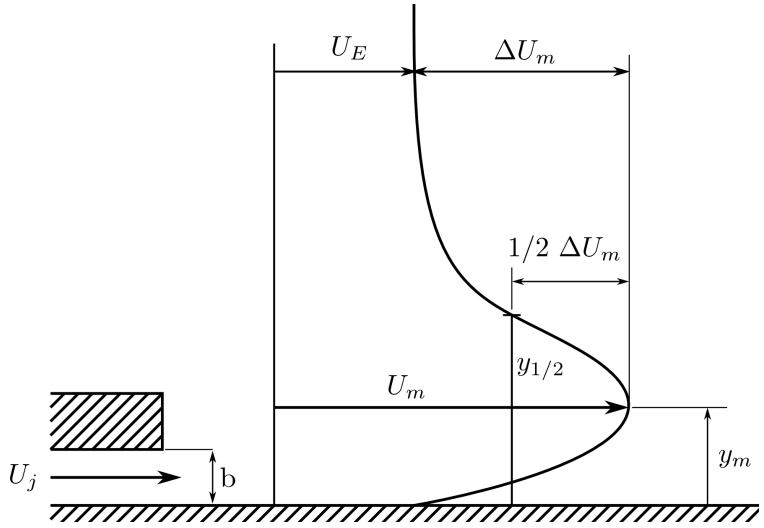

Figure 5.2 *Plane turbulent wall jet*

In figure 5.2, U_j is the flow velocity at jet discharge, U_E is the ambient fluid velocity, U_m is the maximum velocity of the wall jet and ΔU_m is the difference between these velocities. y_m is defined as the y-coordinate of the maximum velocity and an important parameter for wall jets is the jet half-width $y_{1/2}$ where the difference between ambient velocity and maximum velocity is halved.

The experimental apparatus used in this work produces a more complicated three dimensional wall jet. The jet discharges from a pipe with a diameter d and spreads in y- and z-directions. Figure 5.3 depicts the flow structure of the three dimensional wall jet.

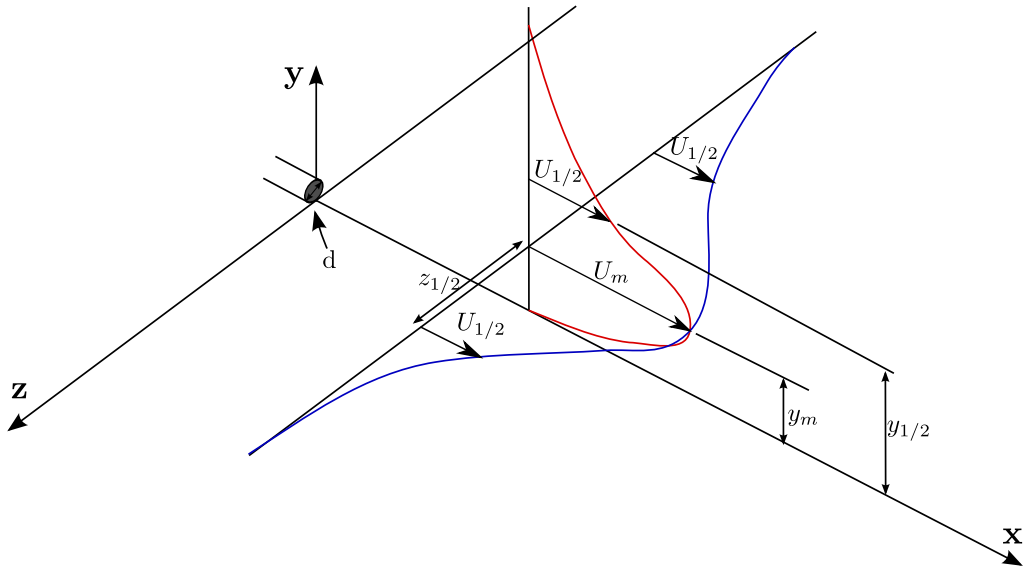

Figure 5.3 *Three dimensional wall jet*

Close to the discharge nozzle, the jet will behave as a free unbounded jet with a

core flow surrounded by a turbulent shear layer. Moving away from the nozzle, the xz-plane and the jet will begin to interact and a velocity profile seen in figure 5.3 will form. Newtonian wall jets reportedly have a far greater lateral spread rate (z-direction) than normal to the wall (y-direction) [20]. Adane investigated a laminar non-Newtonian wall jet with PIV measurements [1] and found similar results than that for a Newtonian fluid. The fluid used in Adane's experiment was a shear-thinning xantham gum solution.

5.2 Photography experiment

In order to measure the spread angle of the jet, the pulp-fibre suspension jet was photographed. To obtain good quality pictures of the jet, it was essential to use a camera that could separate the sheared suspension under motion from the stationary pulp that is unaffected by the shearing motion imposed by the jet. It was found experimentally, that by using a back-illuminated lighting, the spread angle of the jet could be easily identified from the photographs.

The jet chamber was covered with a plastic sheet to create a dim space around the plexiglass, eliminating reflections from the acrylic glass. Three 400W halogen work lights combined with a light diffuser made out of nylon sheet and aluminium frame was used to provide suitable back-illuminated lighting for the experiments. The photography arrangement used in this work is presented in figure 5.4.

A Nikon D90 DSLR camera with a 12.3 megapixel CMOS sensor was used to photograph the pulp fibre suspension jet entering the test section. The photographs were taken of the surface where the inlet pipe was attached to the plexiglass surface as seen in figure 5.4. The lens was focused manually into the inner surface of the test section by placing a focusing shape onto the surface and then focusing the camera until the shape becomes clear.

The parameters affecting the produced photographs are shutter speed, aperture, ISO-number and exposure compensation. These four parameters were tested systematically to find the best combination to produce the clearest pictures.

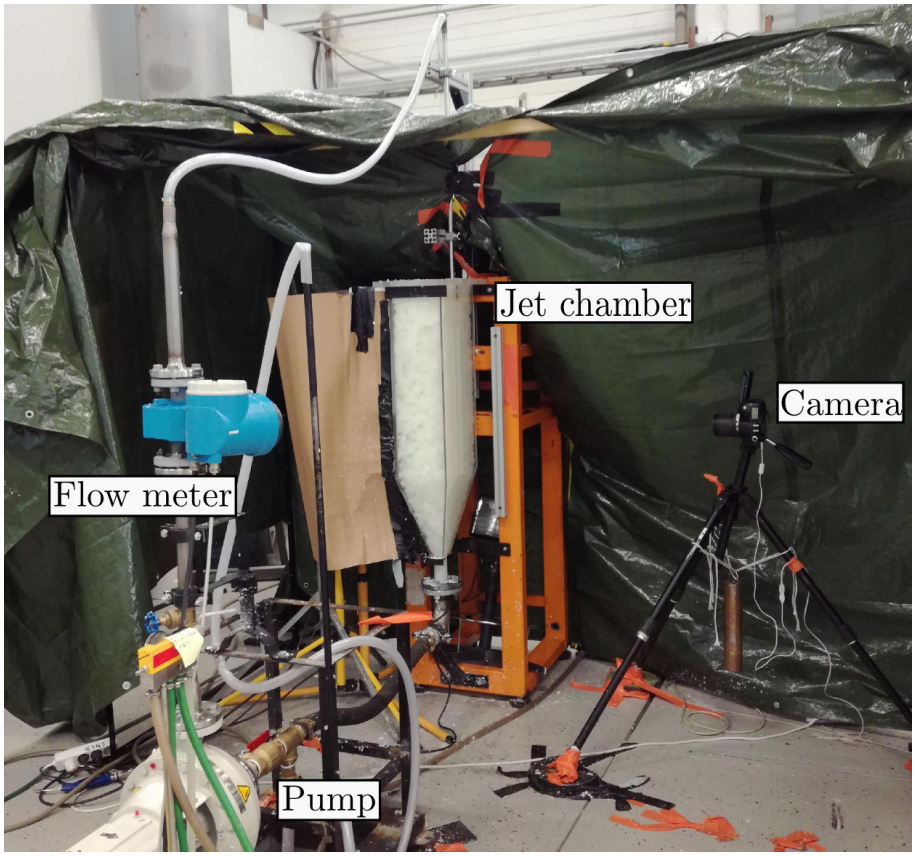

Figure 5.4 *Overview of the photography arrangement*

It was found experimentally, that by using relatively long exposure times, the sheared pulp could easily be separated from the unyielded pulp. The suspension in the jet chamber could coarsely be categorized into three different types, based on visual observations:

- Completely fluidised
- Partially fluidised
- Stationary unyielded pulp

Completely fluidised pulp was observed in the cavern formed by the jet. This area extends into the chamber, depending on the flow rate and consistency of the suspension. Increasing the volumetric flow rate in the system, the cavern size increased. Increasing the mass consistency of the suspension decreased the fluidised volume of the pulp. The fibre suspension in the completely fluidised region flows in a completely Newtonian fashion and fibres move freely in relation to each other.

At the edges of the fluidised suspension, the decaying turbulence field causes the fibres to mechanically lock in on each other and form flocs. Closer to the walls of

the tank, the suspension forms a more thick network as the shearing forces imposed by the jet dissipate.

The stationary unyielded pulp was observed in the areas of the tank where fluid movement was minimal. The pulp formed whole networks that remained stationary regardless of the flow rate. In these areas, the shearing rates are not enough to break down the fibre networks.

The different flow regions of the suspension can be identified from the photographs, such as the one presented in figure 5.5.

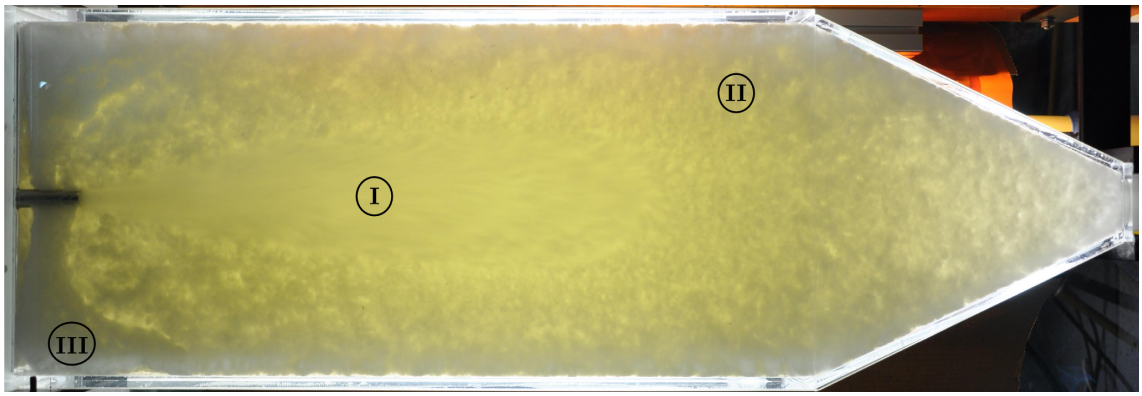

Figure 5.5 *Typical photograph of the jet with zones depicted: (I): Completely fluidised pulp, (II): Partially fluidised (III): Unyielded pulp*

At the lowest mass consistency of $C_m = 1\%$, the interface between the completely fluidised and partially fluidised suspension is not clearly visible in the photographs. For this reason, the jet penetration depth was difficult to measure from the photographs of the low consistency suspension. It could also be argued that, at this consistency the yield stress behaviour of the suspension is insignificant and the suspension behaves in a fluid-type manner throughout the jet chamber.

In order to measure the opening angle and the penetration length of the jet, ten photographs were sampled from each set of photographs. The picture analysis was done by using a vector graphics program Inkscape, which allows importing the pictures in jpg format into the program and using rulers to measure the jet penetration and jet width in pixels. These pixel readings were then converted into millimeters and the half-angle of the jet spread was calculated using by using geometric calculus. The measured values of jet depth, width and angle were averaged over the ten pictures. Figure 5.6 illustrates the image analysis method.

The opening angle was then calculated by using:

$$\Omega = \frac{1}{2}\left[\arctan\left(\frac{W(L_1)}{2L_1}\right) + \arctan\left(\frac{W(L_2)}{2L_2}\right)\right], \tag{5.1}$$

where L_1 was fixed at a distance of 210 millimeters from the pipe nozzle. L_2 was placed at the location where the fluidised region was widest.

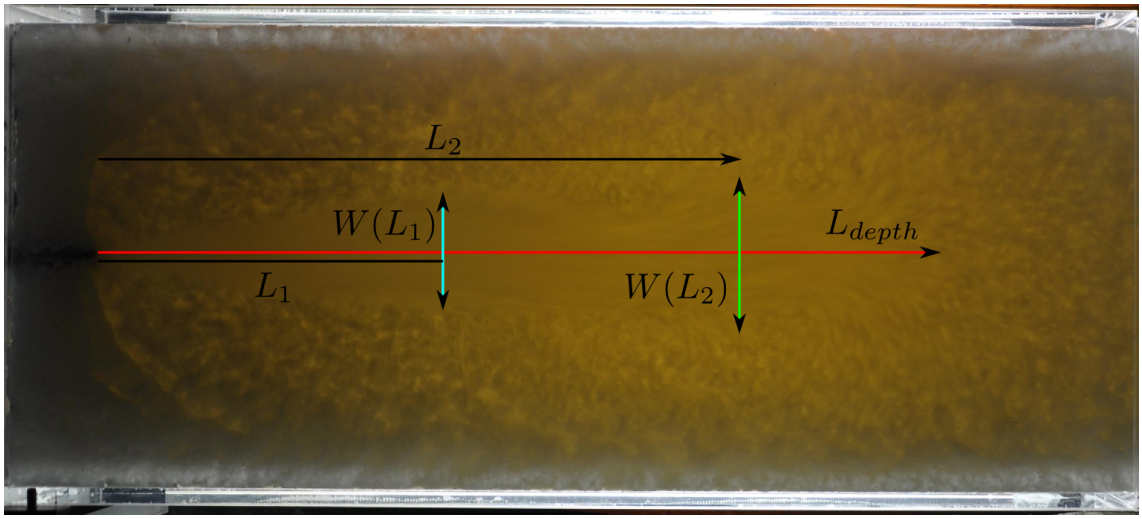

Figure 5.6 *Jet measurement procedure*

For the low flowrate measurements of $Q = 0.3dm^3/s$, the jet penetration length did not exceed 210 millimeters. The angle of the jet was measured by finding the widest area of the jet in the pictures and measuring the angle based on that width only.

5.3 Pulsed Doppler ultrasound velocimetry

Pulsed ultrasound velocimetry (PUDV) has been applied to a wide number of flow cases over the past 20 years. Takeda [34] developed and used PUDV to measure the recirculating flow field of a square cavity, T-branching flow of mercury and oscillating pipe flow. Takeda listed the strengths of PUDV-measurement technique as:

- Efficient flow mapping
- Applicability to opaque liquids
- Ability to record the spatiotemporal velocity field

Ultrasonic Doppler velocimetry has also been successfully applied to pulp fibre suspension flows by Mozaffari [10], who measured pulp-fibre suspension velocities in

an agitated chest with mass consistencies ranging from 2.1% to 3.3%. Jäsberg [18] measured velocity profiles of turbulent birch and pine fibre suspensions in pipe flow. Jäsberg also estimated the intensity of turbulence in the pipe flow from the velocity fluctuations present in the ultrasound data. Xu [40] used PUDV to measure velocity profiles of fibre suspension in a rectangular channel and in a small scale planar headbox forming jet.

Garman [11] used PUDV to measure velocity profiles of water and soda lime glass spheres in an experimental centrifugal pump loop. These measurements were then compared to CFD results and a reasonable agreement was found between the measured results and the numerical simulations. Similar work was done by Pakzad et al. [29] where ultrasound was used to measure the velocities of xantham gum sheared by an impeller. Commercial CFD code was used to simulate the impeller flow regime using Herschel-Bulkley viscosity model and a MRF-approach. Good agreement was found between the simulated and measured velocity fields.

Most authors noted that one of the weaknesses of the PUDV measurement method is the inability to accurately measure the ultrasound echo near a wall. This was also found to be the case in the measurements done in this work. The ultrasound echo penetration distance into the suspension was found to be fairly limited and it was impossible to measure the velocity profile through the whole jet chamber area.

5.3.1 Principle of PUDV

Pulsed Doppler ultrasound velocimetry device DOP-2000 by Signal Processing was used to measure the velocity profile of the wall jet. The velocity profile of the flow is derived from the shifts in positions of the fibres between the transmitted pulses. The principle of measurement is depicted in figure 5.7.

In figure 5.7 the angle θ is the Doppler angle between the transducer signal pulse and the flow direction, u_p is the velocity of the particle in the flow and P_1 and P_2 the measured particle depths in two consecutive pulses. The transducer sends short ultrasonic bursts and after sending the bursts switches to receiving mode to listen on the reflections of these bursts. The depth of a particle P can be calculated from the time delay T_d between an emitted burst and the received echo from the particle:

$$P = \frac{c \cdot T_d}{2}, \tag{5.2}$$

where c is the speed of sound in the liquid. When the particle is travelling in an

angle θ compared to the axis of the ultrasonic beam, as in figure 5.7, the velocity of the particle can be computed from the change of its depth between two emissions:

$$P_2 - P_1 = u_P T_{prf} \cos(\theta) = \frac{c}{2}(T_2 - T_1), \tag{5.3}$$

where T_{prf} is the time between two consecutive pulses and it is inverse of the pulse-repetition frequency, a parameter that can be selected from the DOP 2000 device. The time-difference $T_2 - T_1$ is often in the range of microseconds, so it is useful to introduce the phase difference of the received echo:

$$\delta = 2\pi f_e (T_2 - T_1), \tag{5.4}$$

where f_e is the emitting frequency. The Doppler frequency can now be expressed in the following way:

$$f_d = \frac{\delta}{2\pi T_{prf}} \tag{5.5}$$

And finally, using equations 5.4 and 5.5 in equation 5.3, the particle velocity can be through the following formula:

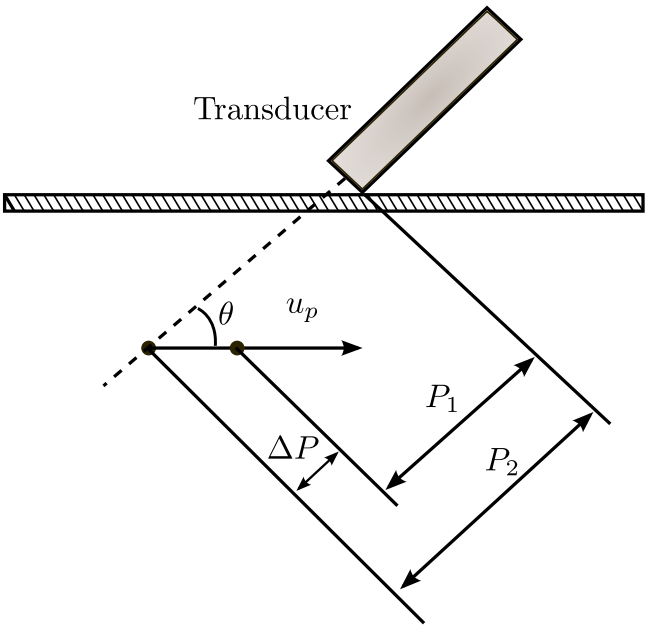

Figure 5.7 *Principle of PUDV-measurement*

$$u_p = \frac{cf_d}{2f_e \cos(\theta)} \tag{5.6}$$

In the measurements done in this work, the particles from which the ultrasound waves are reflected, are the fibres and flocs suspended in water. Because of the continuum hypothesis made earlier, the fibres are assumed to move at the same velocity as the suspending medium. Essentially a two-phase mixture is simplified to a single non-Newtonian suspension. No assumptions about slip velocity between the fibres and water are made and the whole suspension is assumed to move at the same velocity.

Because the transducer switches between emitting and listening of the ultrasound pulses, the velocity information of the particles is only available periodically. Thus, the PUDV technique suffers from the Nyquist theorem and for each pulse repetition frequency there is a maximum velocity that the PUDV system is able to record. If the measured velocities are too high, the measured ultrasound echoes are aliased, and incorrect velocities are recorded.

5.3.2 PUDV measurement settings

The PUDV velocity profile measurements were done on the centerline of the jet. Two 4MHz transducers were used at two different Doppler angles. For each profile, 32 echoes were collected and for one measurement, 1000 profiles were recorded. These velocity profiles were then averaged, to form the averaged velocity profile of the jet. Pulse repetition frequency was set based on the volumetric flow rate of the measurement, so that the frequency was enough to capture the largest velocity value. The measurement configuration is depicted in figure 5.8 with related parameters in table 5.1.

Table 5.1 *Parameters in PUDV-measurement*

$L_1 = 415$ mm	$\alpha_1 = 80^o$	$L_2 = 420$ mm	$\alpha_2 = 75^o$
$c_w = 1700$ m/s	$c_l = 1400$ m/s	$d_w = 10.0$ mm	$d_c = 0$ mm

The measured PUDV-profiles were corrected using a wall-correction formula by Wang [38]. This correction was made, because the ultrasound beam travels through media with different ultrasound velocities. The regular software in DOP2000-device calculates the measuring incorrectly as it does not take the different mediums into account.

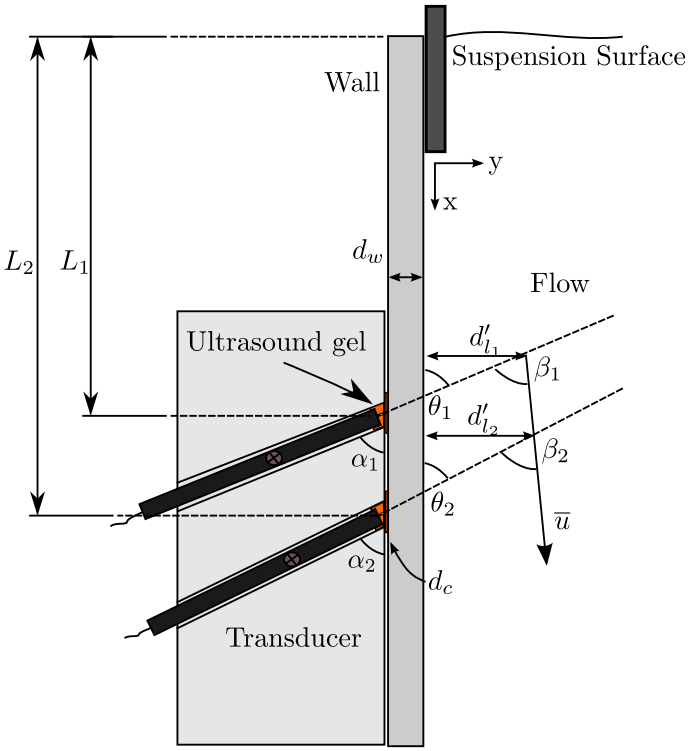

Figure 5.8 *PUDV-measurement setup*

The correct measuring distance d is calculated using the following formula:

$$d = d_c + d_w + d_l = d_c + d_w + \left(\frac{d'_l}{c_l \sin\alpha} - \frac{d_c}{c_c \sin\alpha} - \frac{d_w}{c_w \sin\beta} \right) c_l \sin\theta, \tag{5.7}$$

where c_l, c_c and c_w are the speeds of sound in the liquid, coupling media and wall, respectively. The speeds of sound in acrylic glass were assumed to be 1700 m/s and 1400 m/s in the suspension.

The transducers were attached into the jet chamber using a mounting kit, which was 3D-printed specifically for this work. The mounting kit had slots for the PUDV-transducers at specific doppler angles listed in table 5.1. The mounting kit was moved into the desired position with railing made from aluminium profile. A photograph showing the PUDV-configuration is presented in figure 5.9.

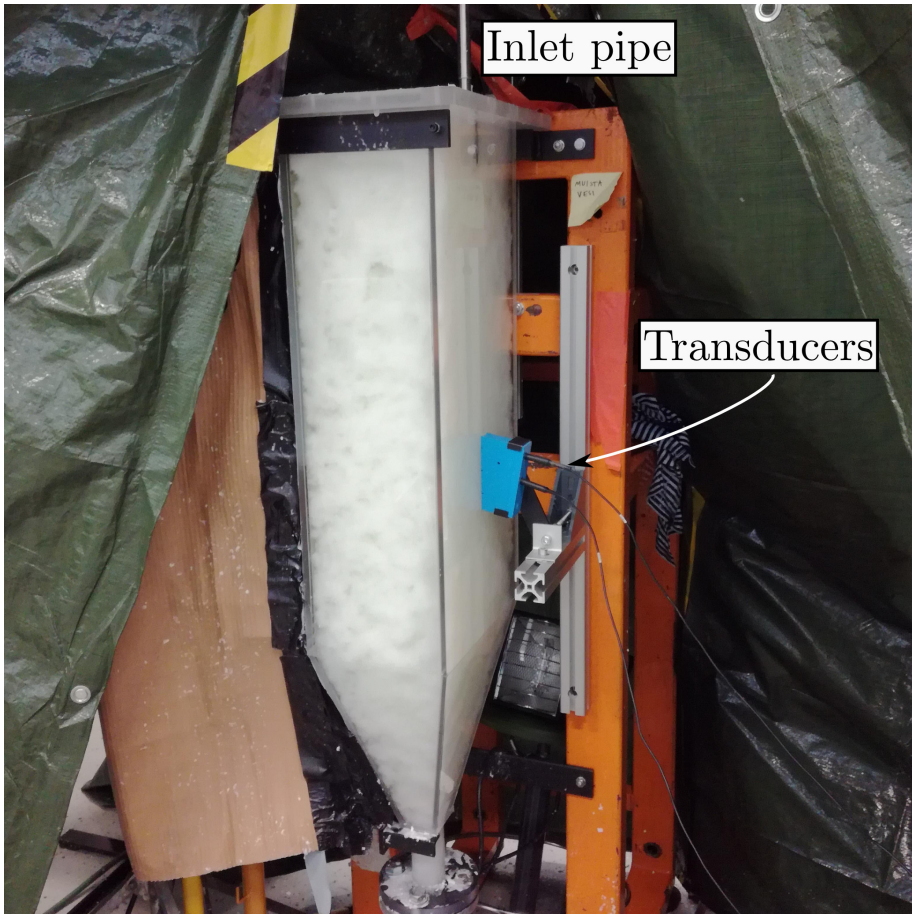

Figure 5.9 *Photograph of PUDV-measurement configuration*

5.4 Measurement results

5.4.1 Image analysis results

The measurements were done with chemically prepared birch- and pine-pulp suspensions. The measured angles and penetration depths for birch- and pine-pulp suspension are listed here. Table 5.2 lists the measured spreading half-angles calculated from equation 5.1 for birch pulp suspension and table 5.3 lists the measured jet penetration depths in inlet pipe diameters d=14mm.

Table 5.2 *Jet opening half-angles for birch pulp suspension, Q in dm^3/s*

C_m	$Q_{low} = 0.3$	$Q_{med} = 0.7$	$Q_{high} = 1.05$
2%	-	7.9^o	10.3^o
3%	-	7.9^o	10.0^o

Table 5.3 *Jet penetration depth for birch pulp suspension, Q in dm^3/s*

C_m	$Q_{low} = 0.3$	$Q_{med} = 0.7$	$Q_{high} = 1.05$
2%	11.3d	39.0d	47.3d
3%	6.1d	28.4d	41.6d

The penetration depth and measurement angles for $C_m = 1\%$ mass consistency suspension could not be determined, due to low consistency suspension not forming strong enough fibre networks to be separated from the photographs. The measured opening angle of the jet remained constant for $C_m = 2\%$ and 3% birch pulp suspension. The penetration depth of the jet decreased, when mass consistency of the suspension was increased. Increasing the amount of fibres in the suspension would appear to affect more on the streamwise velocity decay of the jet, than on the opening angle of the jet.

Similar results were obtained for pine-pulp suspension. There is however, a surprisingly large difference between the pine- and birch-pulp suspensions, in regards to measured penetration depths and spread rates. Unlike birch pulp suspension, the jet angle was also measured for $C_m = 1\%$ mass consistency pine-suspension.

Table 5.4 *Jet opening angles for pine pulp suspension, Q in dm^3/s*

C_m	$Q_{low} = 0.3$	$Q_{med} = 0.7$	$Q_{high} = 1.05$
1%	13.7^o	15.2^o	17.4^o
2%	-	13.6^o	15.7^o
3%	-	8.3^o	11.1^o

Table 5.5 *Jet penetration depth for pine pulp suspension, Q in dm^3/s*

C_m	$Q_{low} = 0.3$	$Q_{med} = 0.7$	$Q_{high} = 1.05$
2%	27.6d	42.5d	48.8d
3%	11.6d	35.5d	47.2d

Due to the heterogeneous multiphase nature of the suspension, the volumetric flow rate fluctuated around the desired value during the measurement. The fluctuation was larger for high consistency suspension, but it was deemed that the volumetric flow rate into the system could be assumed to be constant.

5.4.2 PUDV measurement results

The velocity profiles measured with PUDV are presented here for volumetric flow rate of Q=0.7dm^3/s for birch- and pine-pulp suspensions. The $C_m = 1\%$ velocity profile resembles that of a Newtonian wall jet. As the fibre concentration increases, the profile begins to deviate from this profile. The wall-slip effect is detectable from the profiles. Figure 5.10 shows the velocity profiles for birch- and pine-pulp suspensions at $C_m = 1\%$ at a volumetric flow rate of 0.7 dm^3/s.

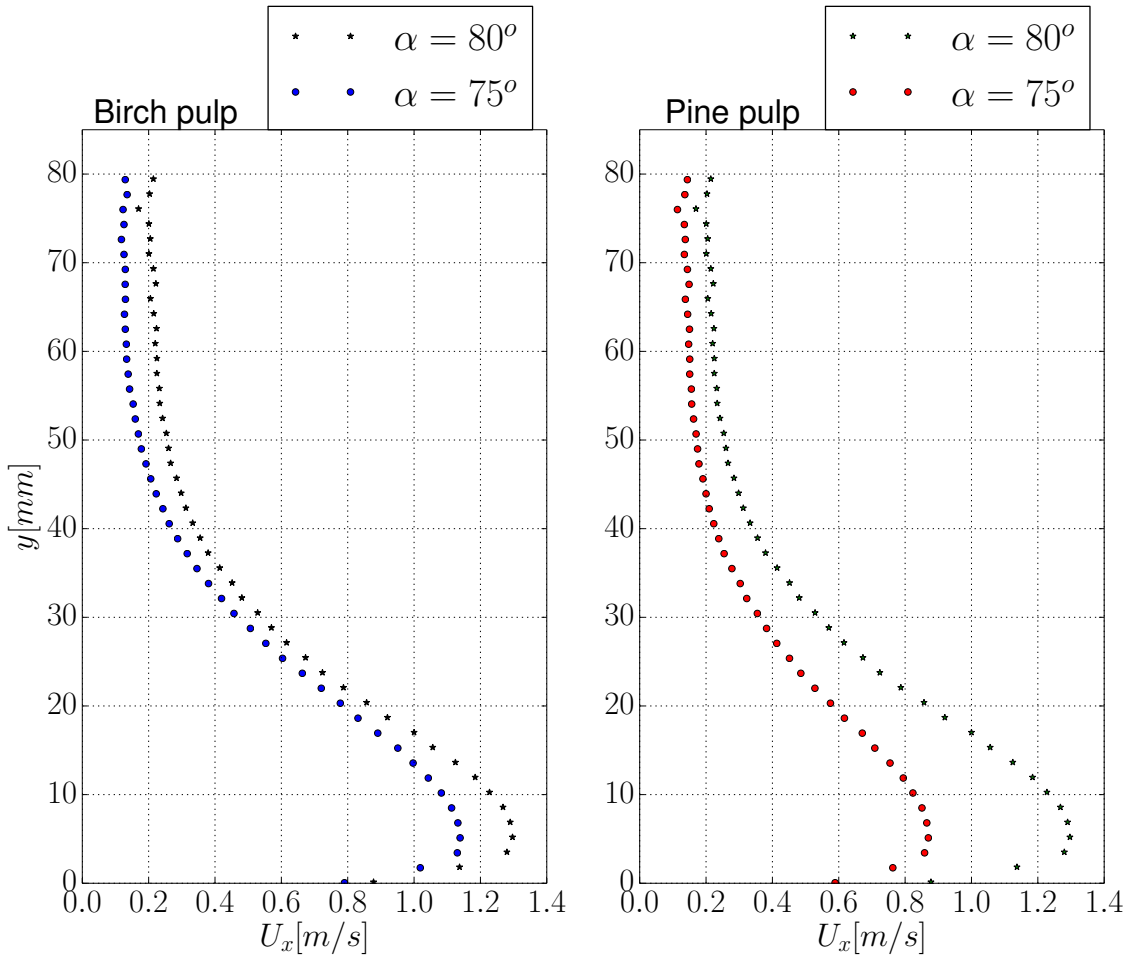

Figure 5.10 *Measured velocity profiles for $C_m = 1\%$ birch and pine pulp suspensions, Q=0.7dm^3/s*

In theory, the profiles measured with different doppler angles should fall into the same curve. The pine-pulp suspension shows a significant deviation in the measured velocity profiles between the different Doppler angles. The absolute measured velocity values should be considered critically, as the angle of the transducer appears to have a significant effect on the measured values. The shape of the profile is the key interest in the PUDV measurements.

Figure 5.11 shows the measured velocity profiles for $C_m = 2\%$ suspension. The profile has a similar shape when compared to the 1% consistency suspension, except there is a sudden increase in the velocity after y=40mm. The reason for the velocity increase is unknown and it is also observed in the 3 percent mass consistency suspension, as seen in figure 5.12.

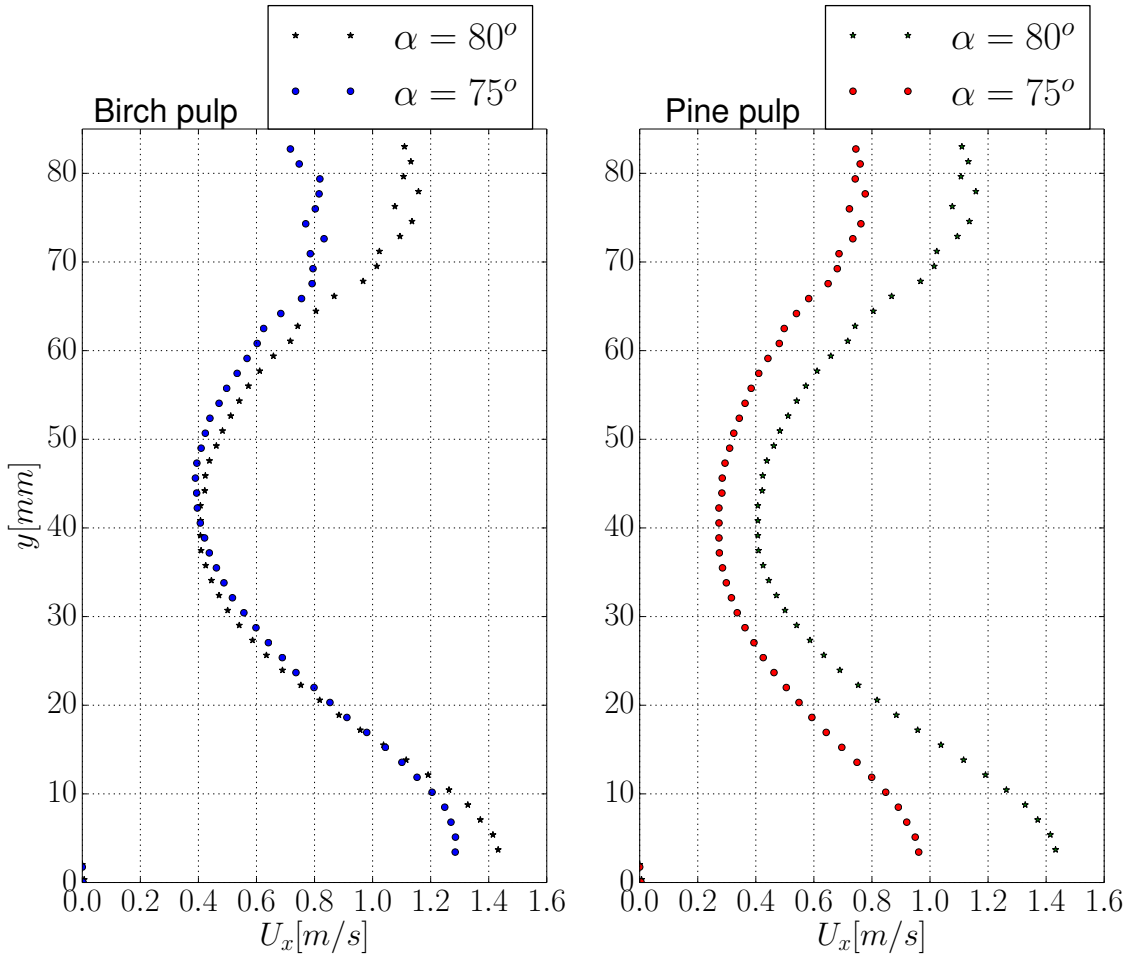

Figure 5.11 *Measured velocity profiles for $C_m = 2\%$ birch and pine pulp suspensions, Q=0.7dm^3/s*

The wall-slip effect is more clear in the $C_m = 2\%$ consistency suspension, when compared to the 1% suspension. The increase in suspension consistency causes the wall jet to create a plug-flow type velocity profile, where wall slip is more prominent.

The measured velocity profile for $C_m = 3\%$ suspensions at a flow rate of 0.7 dm^3/s are presented in figure 5.12. The measured velocity values for 3 percent mass consistency suspensions are smaller than for lower consistencies. The increased consistency decreases the jet penetration depth, thus decreasing the velocity values at the measurement location.

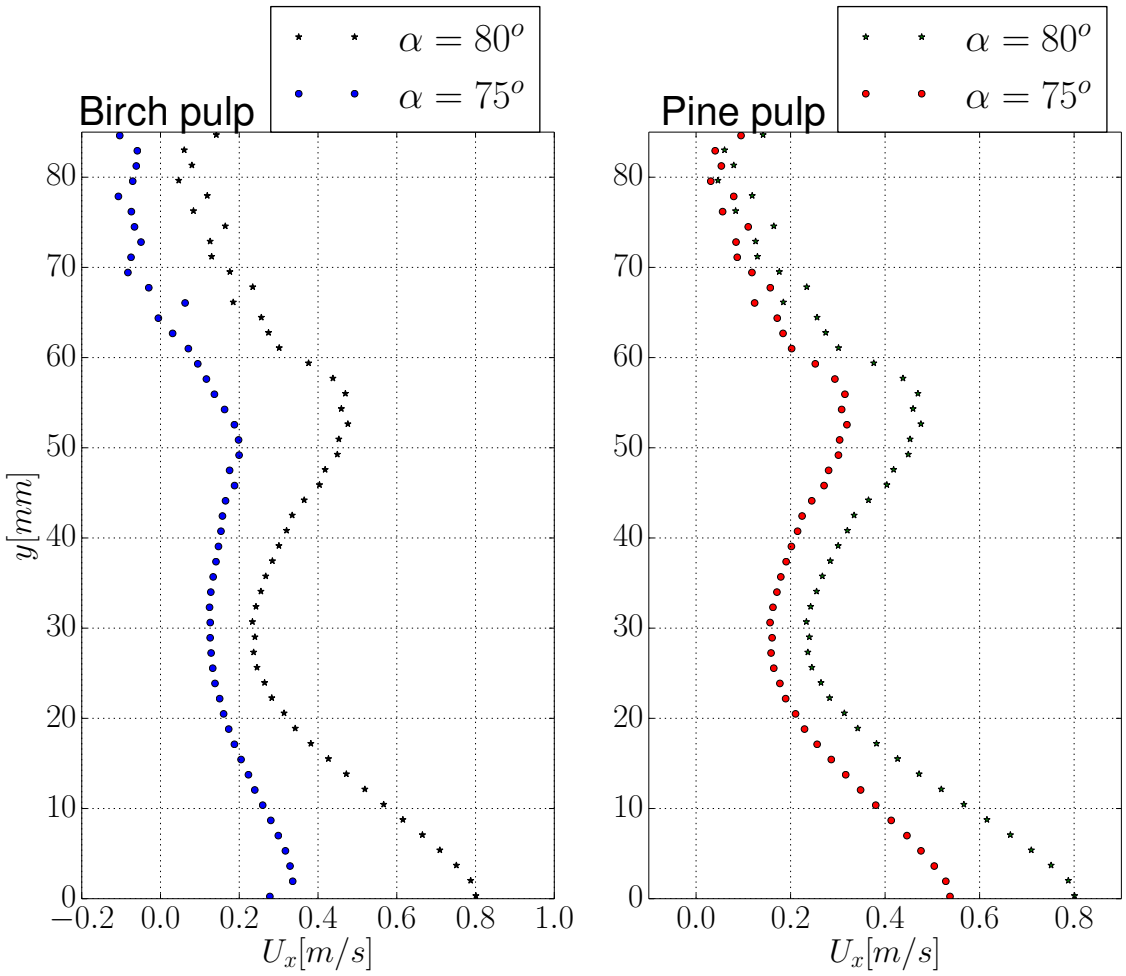

Figure 5.12 *Measured velocity profiles for $C_m = 3\%$ birch and pine pulp suspensions, Q=0.7dm^3/s*

The ultrasound echo signal strength diminished quickly when moving deeper into the suspension. The higher consistency suspensions reduced the signal strength at a faster pace.

6. COMPUTATIONAL FLUID DYNAMICS

Computational Fluid Dynamics, or CFD, studies systems that involve fluid flow and associated phenomena, such as heat transfer and chemical reactions, by using computer-based simulations. Decresed computational costs have made CFD a powerful tool for industrial research and development. The complexity of the underlying physics in fluid dynamics is the reason why CFD is not as widely used in industrial design, when compared to other computer-aided design methods such as structural mechanics solvers [37].

According to Sagaut [32], computational fluid dynamics simulations have two distinctly different purposes:

First, fundamental research simulations help us understand, model and gain insight into the physics underlying the flow problem. These type of simulations produce results with very high accuracy and require that all the physics governing the flow are correctly modelled. The aim of the fundamental type of research is to gain understanding of the correct modelling methods, that can then be used in industrial applications.

Second, engineering CFD analyses are simulations, where the designers want to predict the flow behaviour of a given system. Here the goal is to understand the values of the physical parameters, that affect the flow system and the goal is to reduce expensive prototyping. Optimizing the incident angle of a mixer blade or finding the optimal fin shape and layout of a cooling fin array are examples of engineering CFD analyses.

The use of CFD has potential in pulp and paper industry, as CFD simulations can be used to find optimal geometries and flow conditions for process equipment. However the multiphase non-Newtonian nature of pulp fibre suspension, combined with highly anisotropic turbulent conditions in process equipment, makes the production of reliable CFD results challenging.

Huhtanen [16] used CFD to analyse the flow of pulp-fibre suspension in paper making processes. Pulp-fibre suspension flows were modelled using a Herschel-Bulkley

material model and RANS turbulence models. A new set of refiner segments were developed based on Huhtanen's research. Olson et al. [27] used CFD simulations to develop a new pulp screen rotor prototype. Based on CFD simulations, a prototype rotor was created and tested at a de-ink newsprint mill. The prototype rotor could provide up to 43% energy savings, when compared to a conventional rotor.

Other processes involving non-Newtonian fluid dynamics, such as wastewater treatment in anaerobic digesters and the flow of food products, can also be modelled using CFD. Sajjadi et al [33] used CFD to simulate unsteady jet mixing of non-Newtonian flow in an anaerobic digester. Optimum power input for efficient mixing could be found from the simulations.

6.1 The Finite Volume Method

The conservation equations presented in Chapter 3 and 4 are partial differential equations with differential volumes. The Finite Volume Method (FVM) transforms these equations into discrete algebraic equations over finite volumes, which can then be solved numerically.

The FVM method can be summarized in 4 steps:

(i) Modelling of the geometric domain and physics involved

(ii) Discretisation of the geometric domain into finite volumes or cells

(iii) Transforming the partial differential equations into discrete ones that are defined over each finite volume

(iv) Solving the algebraic set of equations in an iterative solver to find the fields that satisfy these equations

The pre-processing step of the solution process involves the creation of the computational domain and mesh generation. The first step of the pre-processing is the creation of the computational domain, which is the physical geometry where the flow field is to be solved. The computational domain is then divided into finite elements to create the finite volume mesh. Figure 6.1 depicts two adjacent finite volumes with related discretisation parameters.

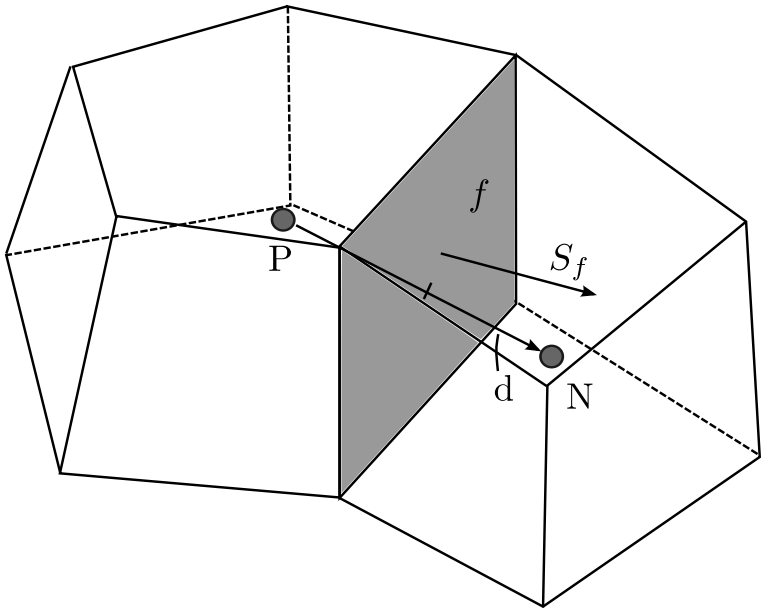

Figure 6.1 *Parameters in finite volume discretisation, adapted from [36]*

P and N in figure 6.1 mark the centroids of finite volumes and f is the face between the volumes and the face normal vector is marked by S_f. The vector between the cell centroids $\overrightarrow{PN}$ has a length of d. The finite volumes in OpenFOAM can be any shape, but hexahedral shapes are most commonly used.

Velocity, pressure and turbulence variables are stored in the centroids of these elements, such as P and N in figure 6.1. Storing both velocity and pressure in the cell centroids can cause non-physical velocity and pressure fields to be sensed as uniform fields by the numerical scheme. The staggered grid arrangement removes this problem by storing pressure and velocity in different locations of the element, but for complex geometries the staggered grid causes issues. A common approach in CFD codes is to use a co-located mesh, where both velocity and pressure are stored in the centroid of the cell, but mass fluxes are stored in the faces of the cell. A special Rhie-Chow interpolation is then used to ensure that pressure and velocity fields behave in a physically realistic manner.

Fluid properties, such as viscosity and density need to be specified for each CFD simulation. The solution process is constrained by boundary conditions, that are specified by the user. Numerical boundary conditions can be divided into two different groups: fixed value and fixed gradient boundary conditions. Typically, the computational domain consists of an inlet, an outlet and the walls that bound the flow. Initial values for all variables have to be specified in the computational domain and boundary conditions for each variable have to be assigned at each boundary surface.

The differential equations in presented in chapter 3 have to be discretized into simple algebraic equations, that are calculated over each cell. These simple equations can then be combined into a system of global matrices and vectors in the form:

$$A\mathbf{x} = \mathbf{b}, \tag{6.1}$$

where A is a matrix that contains coefficients from the discretisation process , $\mathbf{x}$ contains the unknown variables at each interior cell and at the boundary of the computational domain and $\mathbf{b}$ is a vector source to the equation. The discretisation begins by transforming the volume integrals into surface integrals using the Gauss theorem. The partial differential equations presented in chapter 4 contain convection terms, diffusion terms and source terms. The operators present different physical phenomena. Thus, the discretisation process for each operator is different.

The formed system of equations is difficult to solve for two reasons: The convection term is non-linear and the formed system is coupled over three equations in x-, y- and z-directions. For this reason, an iterative solver is used to find the final solution to the flow field by using solutions of previous iterations. The convergence rate of the solver depends on the size of the problem and the diagonal dominance of the matrix A.

The most significant challenge in incompressible flow CFD is that there is no transport equation for pressure, yet the pressure gradient is present in the momentum equations. The SIMPLE-algorithm developed by Spalding and Patankar tackles this problem by transforming the continuity equation into a pressure correction equation. The initial pressure field is guessed and the discretized momentum equations are solved to obtain the velocity field. The pressure field is then corrected by using the pressure correction equation with the obtained velocity field, so that the continuity equation is satisfied. This process is done iteratively until velocity and pressure fields are obtained, that satisfy both momentum and continuity equations. Under-relaxation is used to blend the new solution value with the old one so that the new pressure and velocity fields do not diverge because of numerical sensitivity.

The post-processing of CFD results is often time consuming, as simulations provide a large amount of data. The goal of post-processing is to present the data of the CFD simulation provides in a meaningful way. Whether the goal of the simulation is to understand more about the general flow field of the system or obtain actual physical values, the data needs to be interpreted correctly.

6.2 OpenFOAM

Open source CFD code OpenFOAM was used for the numerical simulation of pulp-fibre suspension jet. OpenFOAM is an object-oriented C++ framework developed to be able to build a variety of different solvers for continuum mechanics problems. The OpenFOAM classes and functions closely mimic continuum mechanics differential operators [39].

For example, the simpleFoam solver in OpenFOAM, uses the SIMPLE-algorithm for pressure and velocity coupling. The solver first solves the following equation for momentum conservation, without including the pressure gradient:

$$\nabla \cdot (\mathbf{U} \otimes \mathbf{U}) - \nabla \cdot (\nu_{eff} \nabla \mathbf{U}) = P\mathbf{U} - C, \tag{6.2}$$

where terms $P\mathbf{U}$ and C are explicit and implicit source and sink terms for momentum. Equation 6.2 is implemented in OpenFOAM as program 6.1 in lines 5-12.

```
1   // Momentum predictor

3   MRF.correctBoundaryVelocity(U);

5   tmp<fvVectorMatrix> UEqn
    (
7       fvm::div(phi, U)
      + MRF.DDt(U)
9     + turbulence->divDevReff(U)
      ==
11      fvOptions(U)
    );
13
    UEqn().relax();
15
    fvOptions.constrain(UEqn());
17
    solve(UEqn() == -fvc::grad(p));
19
    fvOptions.correct(U);
```

Program 6.1 *Momentum predictor in simpleFoam solver loop*

In program 6.1 fvm::div(phi, U) is the convection term $\nabla \cdot (\mathbf{UU})$, MRF.DDt(U) contains terms from possible rotational sources and the pointer turbulence->divDevReff(U) contains the $\nabla \cdot (\nu_{eff} \nabla \mathbf{U})$ term, which includes contributions from the viscosity

model and the turbulence model. Possible sources and sinks of momentum are included in the fvOptions(U) term. The fvm::div operator discretises the convection term in a implicit way, while explicit discretisation would be done by using a fvc::div operator.

UEqn().relax() applies under-relaxation to the momentum equation, which is required to stabilize the SIMPLE-algorithm. The fvOptions.constrain(UEqn()) on line 16 applies possible user-defined constraints. Finally, the momentum predictor with the included pressure gradient is solved in line 18 of program 6.1 in solve(UEqn() == -fvc::grad(p)).

After the momentum predictor phase, the pressure correction equation is solved, where the velocities computed by the momentum predictor are corrected to satisfy continuity. The corrected velocity field is used to compute a new pressure field, which also satisfies continuity. The corrected velocities and pressures are then used in program 6.1 again. The SIMPLE-algorithm iteratively loops through this process until desired solution convergence is reached.

6.2.1 OpenFOAM case directory structure

OpenFOAM case is set up as a case directory, which contains sub-directories with necessary files such as boundary conditions and selected turbulence models. The case directory structure is shown in figure 6.2.

The system directory contains files and parameters related to the solution process itself. The controlDict file determines the run control parameters such as output of files and start and end time of the simulation. In the fvSchemes file, the discretisation methods for the differential operators present in the partial differential equations in chapters 3 and 4 are selected. Finally, in the fvSolution dictionary, solver settings, such as equation under-relaxation factors and tolerances are selected.

The constant directory contains physical properties of the simulation, such as fluid properties and turbulence properties. Material properties of the fluid are determined in the transportProperties file in the constant directory. Turbulence modeling method is selected in the turbulenceProperties of the constant directory, where the user can first select the type of simulation (RAS,LES,laminar) and then select the turbulence model itself. The polyMesh subdirectory contains a complete description of the finite volume mesh.

The time directories contains files for fields such as velocity, turbulent kinetic energy k and pressure. The user must specify the boundary conditions of the simulation in

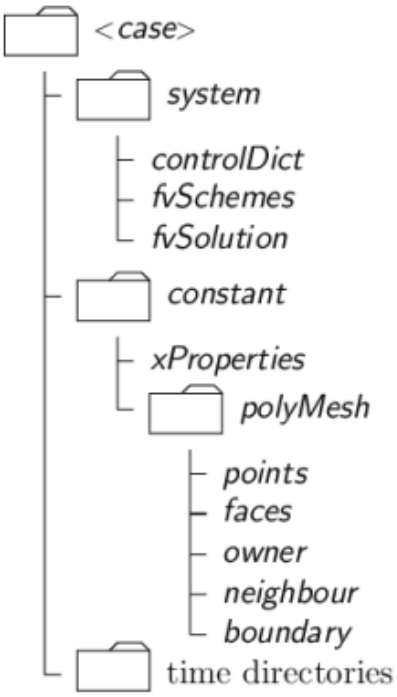

Figure 6.2 *OpenFOAM case directory structure [36]*

the files of the time directory that the simulation starts from. New time directories are written as the simulation progresses and the user can control the write interval in the controlDict file in the system directory.

Solving the case is done by running the chosen solver at the case directory. OpenFOAM has numerous different solvers for both compressible and incompressible simulations. Large CFD cases, such as the one in this work, requires multiple CPU:s to be used, in order to solve the system in reasonable time. The number of CPU:s used by the solver is defined by the user, when the solver is started.

Parallelization in OpenFOAM is done by dividing the mesh to as many processors as selected by the user. The interface between the processor meshes is handled by processor faces. At the end of the simulation the individual processor domains can be reconstructed back into a complete case for post-processing.

Paraview [2], an open-source data analysis and visualization software was used to post-process the CFD data of this work. Paraview can be used interactively with an user interface or with Python batch scripts to produce both 3D flow information such as contour plots and streamlines or 2D-plots for velocity profiles.

7. CASES AND RESULTS

7.1 Numerical simulation setup

The flow in the jet chamber was simulated by using a steady-state incompressible CFD solver simpleFoam. Herschel-Bulkley viscosity model was used to model the apparent viscosity of the pulp-fibre suspension and turbulence was accounted for by using the $k-\omega$ SST turbulence model.

Simulations were done a linux-based computing cluster Merope located at Tampere University of Technology. Typically in CFD simulations, convergence of the simulation is monitored by using residuals. It was however found out, that the unsteady nature of the simulation (a separating flow combined with a non-Newtonian material model) caused the equation residuals to stay at a high value. Convergence of the simulation was instead monitored by creating monitors in the flow field. When the average value of a scalar variable, such as turbulent kinetic energy of turbulence k, over a surface in the flow field did not change over iterations, it could be concluded that the simulation has reached a solution.

7.1.1 Computational domain

The experimental jet chamber was generated as a geometric domain with Salome pre-processor [28]. The output generated by Salome are the surfaces that bound the computational domain in STL-format. A presentation of the computational domain is presented in figures 7.1 and 7.2.

The computational domain takes advantage of the symmetry of the system and only half of the jet chamber is meshed. For meshing purposes two simplifications were done to the computational domain: The gap between the bottom wall and the inlet pipe entering the jet chamber is sealed with a straight wall and the wall thickness between the bottom wall and the inlet pipe is not modelled in the geometry. These simplifications are illustrated in picture 7.2 (c). The inlet is located at $x = 0$ and the flow profile is allowed to develop for 160 mm (10.75 d_{inlet}) before entering the

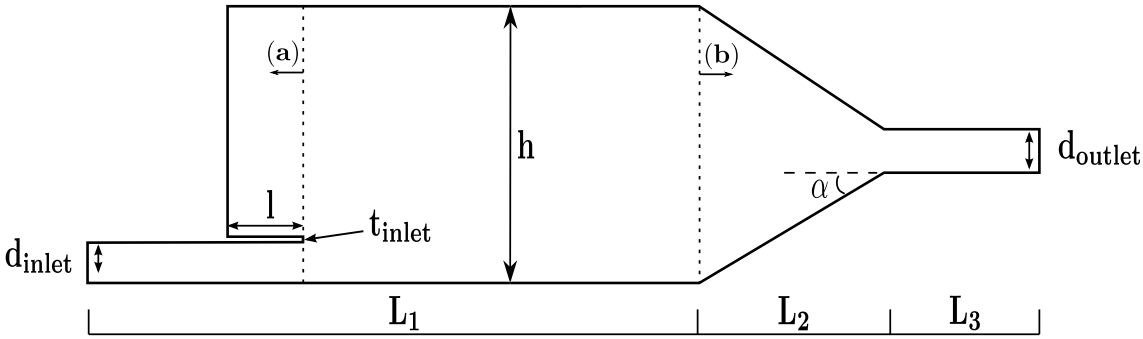

Figure 7.1 *Overview of the geometrical domain (xy-plane)*

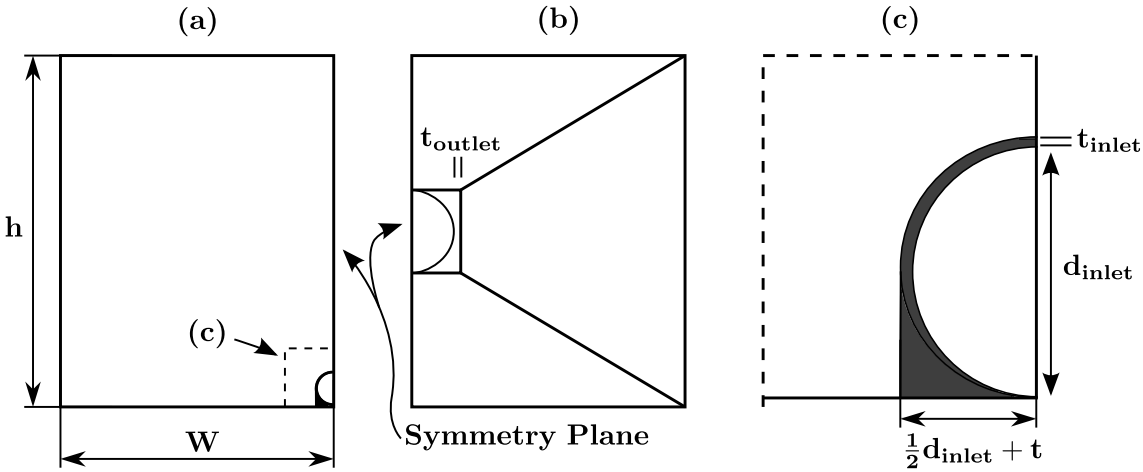

Figure 7.2 *(a): View to the negative x-direction (b): View to the positive x-direction (c): Close up of the pipe entering the chamber area*

chamber area. This ensures that the flow profile that discharges from the pipe nozzle is fully developed. The outlet of the chamber is located at $x = 1340mm$ and with $250mm$ of outlet pipe modelled so no gradients are present at the outlet to satisfy the boundary conditions for velocity and turbulence variables.

The computational domain is otherwise a replication of the experimental jet chamber constructed. The dimensions used in figures 7.1 and 7.2 are presented in table 7.1 below:

Table 7.1 *Geometric domain dimensions*

d_{inlet}	14.00 mm	t_{inlet}	0.65 mm	W	140.00 mm
l	50.00 mm	L_1	790.00 mm		
L_2	300.00 mm	L_3	250.00 mm		
d_{outlet}	40.00 mm	t_{outlet}	5.00 mm		
α	13.134^o	h	180.00 mm		

The finite volume mesh used in the simulations was created by using an automatic mesh generator cfMesh [17]. The unstructured mesh used in the simulation consisted

of approximately 5 million cells. Most of these cells were hexahedral, but some polyhedral and tetrahedral cells were created in areas which were difficult for the mesher. The mesh was refined in areas were high gradients would be present and left unrefined in areas with small gradients. The vicinity of the walls are meshed with three boundary layer cells. Figure 7.3 has the computational mesh depicted with details of selected areas.

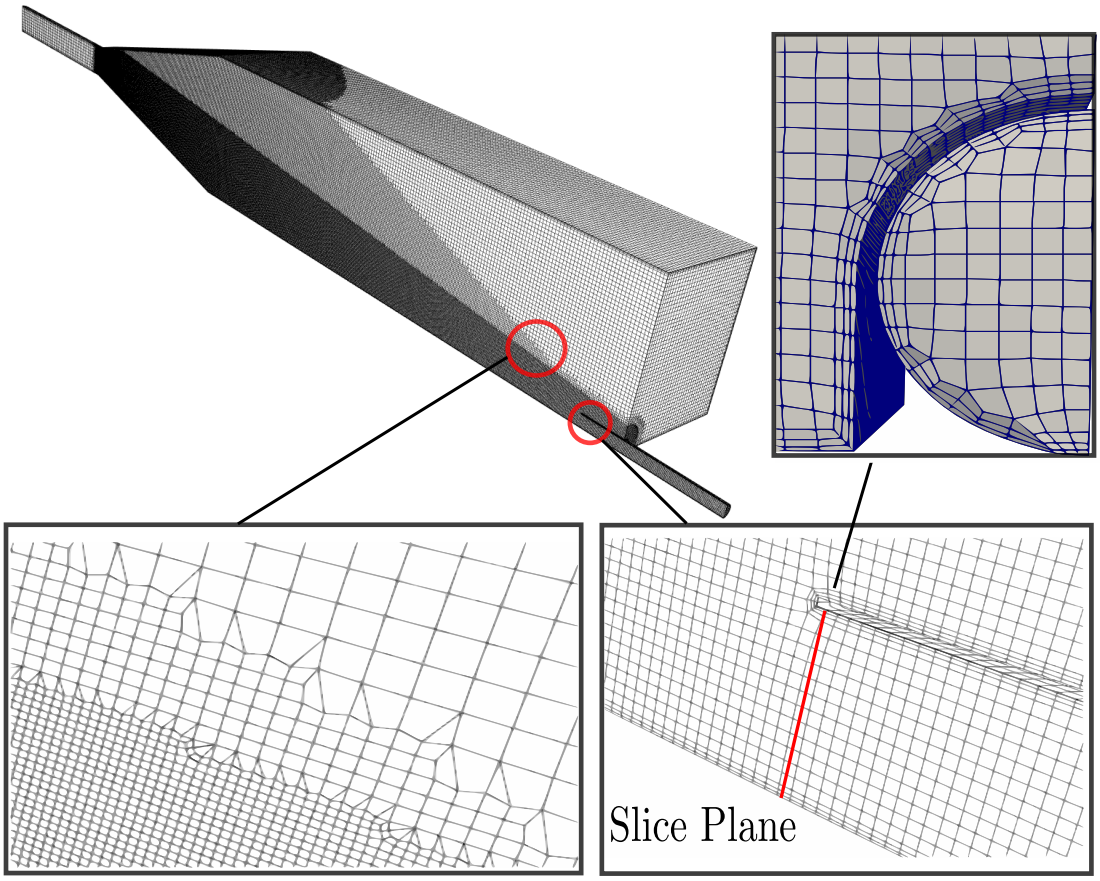

Figure 7.3 *Computational mesh with details*

Using an automated meshing tool such as cfMesh speeds up the whole CFD process as the user does not need to provide anything else but the geometry of the computational domain. This is crucial as time is conserved when geometries become more complex. The quality of the mesh was checked with an OpenFOAM utility and all the metrics (skewness, non-orthogonality and cell openess) were in the approved range.

A mesh independence study was also done, to see that the simulation results were not dependent on the selected cell size. A coarser mesh of approximately 1.5 million cells was used as a comparison, and the maximum x-directional velocity difference between the meshes was in the range of 4 percent. The results could then be considered to be independent of the mesh size. The fine mesh was used for the simulation

for improved accuracy. The fine mesh was divided for 48 processors, leaving approximately 100,000 cells per processor.

7.1.2 Boundary and Initial conditions

Boundary conditions are specified for velocity, pressure and turbulence variables. The velocity was fixed at zero at the walls of the domain, and a slip-condition was used at the top surface of the tank. The slip-condition secures that the mass flux normal to the surface is zero, but does not enforce tangential velocities so the can fluid move parallel to the surface. Table 7.2 below lists the used boundary conditions for pressure p and velocity U in OpenFOAM syntax for the numerical simulations:

Table 7.2 *Boundary conditions for velocity and pressure*

patch	p	U
inlet	zeroGradient	volumetricFlowRate
outlet	fixedValue uniform 0.00	InletOutlet
surface	zeroGradient	slip
walls	zeroGradient	fixedValue uniform (0 0 0)
symmetry	symmetryPlane	symmetryPlane

The zeroGradient boundary condition forces the gradient of the variable to be zero at a given patch. This is used for pressure at the inlet and the walls of the computational domain. For incompressible flows, the pressure has to be fixed at some patch. Typically the pressure at the outlet is defined and here it is also fixed to zero with the fixedValue boundary condition.

The volumetricFlowRate boundary condition for velocity is defined by selecting a volumetric inflow rate into the system. The inletOutlet boundary condition for velocity at the outlet is identical to that of zeroGradient, except if the flow would move into the domain. In this case the boundary condition would enforce a fixedValue type boundary condition with the aim of restricting the reversed flow into the domain.

The symmetryPlane boundary condition creates a symmetric mirror plane into the computational domain. No mass is moved across the symmetry plane and all gradients across the symmetry plane are equal to zero.

For turbulent kinetic energy k, the inlet value can be estimated through turbulence intensity I. The kinetic energy k can be estimated through the following equation:

$$k = \frac{3}{2}(IU)^2 \tag{7.1}$$

This approach does however require the approximation of the turbulent intensity I, which is a measure of the level of turbulence. I is non-dimensional and is defined as the ratio of average velocity fluctuation u' divided by bulk velocity U:

$$I = \frac{u'}{U} \tag{7.2}$$

It was assumed that the turbulent intensity was 3%. The value selected does not have a significant effect on the simulation outcome. The inlet value for ω was chosen to be fixed at 500.0 $1/s$. Boundary conditions for k and ω are listed in tables 7.3 and 7.4.

Table 7.3 *Boundary conditions for k*

patch	k	value
inlet	turbulentIntensityKineticEnergyInlet	intensity 0.03
outlet	inletOutlet	internalField
surface	slip	-
walls	kqRWallFunction	-
symmetry	symmetryPlane	-

For walls, a kqRWallFunction boundary condition was used, which essentially is a zeroGradient boundary condition.

Table 7.4 *Boundary conditions for ω*

patch	ω	value
inlet	fixedValue	500.0
outlet	zeroGradient	-
surface	zeroGradient	-
walls	omegaWallFunction	-
symmetry	symmetryPlane	-

The omegaWallFunction boundary condition selected for walls enables the use of wall functions in the calculation of ω near wall cells. The formulation was presented in equations 4.51- 4.53 in chapter 4.

For turbulent viscosity ν_t a calculated-type boundary condition was used in inlet, outlet and surface patches. This boundary condition calculates the ν_t value based on the $k - \omega$ SST turbulence model ν_t formulation. For walls, a nutUSpalding-WallFunction was used, which calculates ν_t in the wall cells based on velocity. The formulation of the Spalding wall function was presented in chapter 4.

7.1.3 Discretisation and solver settings

The selected discretisation methods and solver settings are selected in the fvSolution and fvSchemes files in systems directory of the case directory. Program 7.1 shows the selected discretisation methods for the differential operators used in the simulations.

```
2  gradSchemes
   {
4          default cellMDLimited Gauss linear 1;
   }
6
   divSchemes
8  {
           div(phi,U)      bounded Gauss linearUpwindV grad(U);
10         div(phi,k)      bounded Gauss upwind;
           div(phi,omega)  bounded Gauss upwind;
12         div((nuEff*dev2(T(grad(U))))   Gauss linear;
   }
14
   laplacianSchemes
16 {
           default         Gauss linear corrected;
18 }
```

Program 7.1 *Discretisation settings from fvSchemes-file*

A cell-limited Green-Gauss gradient was used for computing the gradient, as seen in line 4 of 7.1. The limiter reduces the instability of the simulation, by limiting the the gradient such that the face values of cells extrapolated by the gradient fall between the bounds of values in surrounding cells [36]. A limiting coefficient 1 ensures boundedness of the gradient.

The convection term for momentum $\nabla \cdot (\mathbf{U} \otimes \mathbf{U})$, turbulent kinetic energy $\nabla \cdot (\mathbf{U}k)$ and specific dissipation rate $\nabla \cdot (\mathbf{U}\omega)$ are discretised with the Gauss upwind method, as seen in lines 9-11 in program 7.1. The upwind method has the least accuracy, but is the most stable method for discretising the convection term. The bounded keyword improves the stability of the solver.

The diffusion terms are discretised by selecting the discretisation method under the laplacianSchemes-keyword in program 7.1. Diffusion terms are present in all transport equations and the modelled non-Newtonian viscosity and turbulent eddy viscosity are added to the momentum equation through the $\nabla \cdot (\nu_{eff} \nabla \mathbf{U})$ term. The corrected keyword in line 17 of program 7.1 corrects the gradient used in the

discretisation of the diffusion term, if the angle between cell face normal and the vector connecting the cell centroids is high.

After discretising the partial differential equations, the system of algebraic equations is solved iteratively. Program 7.2 shows the selected algebraic solver settings for the simulations, defined in the fvSolution file in the systems directory of the case. The solvers and smoothers were selected based on recommendations from the OpenFOAM guide [36].

```
p
{
        solver           GAMG;
        tolerance        1e-6;
        relTol           0.01;
        smoother         GaussSeidel;
        cacheAgglomeration on;
        agglomerator     faceAreaPair;
        nCellsInCoarsestLevel 100;
        mergeLevels     1;
}
"(U|k|omega)"
{
        solver           smoothSolver;
        smoother         GaussSeidel;
        tolerance        1e-8;
        relTol           0.1;
        nSweeps          1;
}
SIMPLE
{
    nNonOrthogonalCorrectors 0;
    consistent yes;
}
```

Program 7.2 *Solver settings from the fvSolution-file*

The Generalised Geometric-algebraic multi-grid solver, or GAMG is recommended for solving pressure. The principle of this solver is to generate a quick solution on a coarse mesh and then mapping this solution onto a fine mesh. The nCellsInCoarsestLevel keyword specifies the approximate number of cells at the coarsest level.

The smoothSolver is used for velocity, k and ω. The smoother keyword defines the used smoother, which was selected as the GaussSeidel. Solver tolerances are selected by the tolerance and relTol keywords. Tolerance is the maximum allowable value of the absolute residual for the solver to stop iterating. relTol is the ratio between the

initial residual and the actual residual for the solver to stop iterating.

For the SIMPLE-algorithm, the consistent keyword defines that the consistent version of the algorithm is used. The consistent SIMPLE has a slightly different formulation, when compared to the regular SIMPLE-algorithm, but in most cases convergence rate of the algorithm is faster.

The under-relaxation factors for the equations were selected in the fvSolutions file of the case directory. in lines 25-37 of program 7.3.

```
relaxationFactors
{
    fields
    {
        p                       0.3;
    }
    equations
    {
        "(U)"                   0.4;
        "(k)"                   0.3;
        "(omega)"               0.3;
    }
}
```

Program 7.3 *Equation under-relaxation settings from the fvSolution-file*

The equations are heavily under-relaxed to ensure the stability of the solution process. Higher under-relaxation factors would speed up the convergence rate, but at a risk of instability.

7.1.4 Material model specifications

The Herschel-Bulkley viscosity model used in OpenFOAM simulations was given by equation:

$$\nu = \min\left(\nu_0\ ,\ \frac{\tau_0}{\dot{\gamma}} + k\dot{\gamma}^{n-1}\right) \tag{7.3}$$

The parameters for the material model are for birch pulp-suspension, which were measured by Mustalahti [25]. Mustalahti expressed the Herschel-Bulkley parameters as a function of C_m. Table 7.5 presents the HB-model parameters.

Table 7.5 *Parameters for HB-model as a function $C_m[\%]$ [25]*

$\tau(\dot{\gamma}) = \tau_0 + K\dot{\gamma}^n$		
τ_0	K	n
$0.57 \cdot (C_m)^{2.64}$	$\frac{3}{4}\tau_0$	0.5

The incompressible solvers in OpenFOAM use kinematic viscosity instead of dynamic viscosity, so parameters τ_0 and k are divided by density of the suspension which was assumed to be 1000 kg/m^3. For numerical reasons, the viscosity model requires a maximum value for viscosity which is known as the zero-shear viscosity ν_0. This is done to ensure that the viscosity would remain in a physically reasonable value when the strain-rate values would near zero. It was decided that the limiting viscosity would be the of the viscosity given by equation 7.3 at a strain-rate value of $\dot{\gamma} = 10^{-3}$.

The parameters used for the Herschel-Bulkley viscosity model for all mass consistencies are given in table 7.6.

Table 7.6 *Parameters for Herschel-Bulkley material model used in OpenFOAM*

$C_m[\%]$	$\tau_0[m^2/s^2]$	k $[m^2/s]$	n	ν_0
1	0.000570	0.0004275	0.5	0.56
2	0.003553	0.0026647	0.5	3.7
3	0.010363	0.0077721	0.5	10.6

7.1.5 Analysis of CFD results

Assumptions had to be made, when comparing the CFD results with the measurements made from the photographs. It was assumed, that the visible area of the jet is limited to the depth of y=$\frac{1}{2}$d. Figure 7.4 depicts the plane, at which CFD results are analysed.

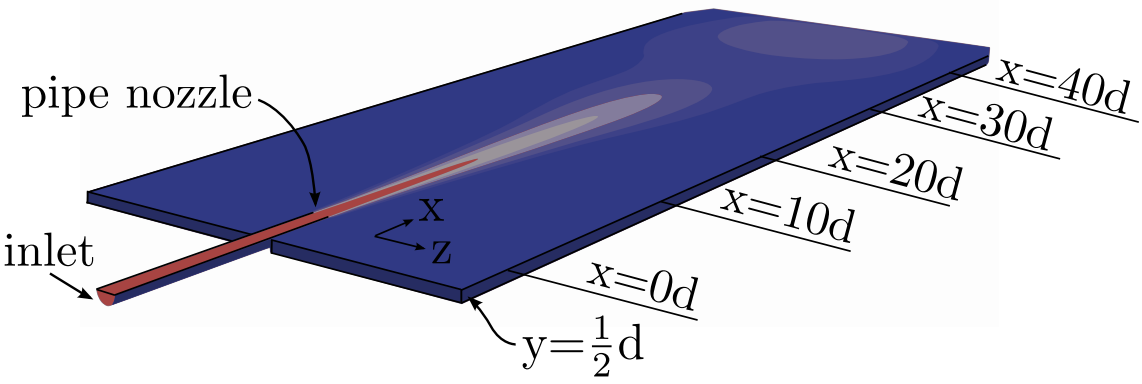

Figure 7.4 *Plane of CFD-measurements*

The edge of the jet in the lateral direction is defined as the location, where the x-directional velocity has dropped to 1% of the jet centerline velocity. The angle of the opening can then be determined as:

$$\Omega = \arctan\left(\frac{z_{edge}}{x}\right), \tag{7.4}$$

where z_{edge} is defined as:

$$z_{edge} = z\left(U_x = 0.01U_0\right), \tag{7.5}$$

where U_0 is the jet centerline velocity in the x-direction and x is the location of the measurement downstream from pipe nozzle.

The penetration depth of the jet in CFD results was determined, by inspecting the maximum x-directional velocity downstream of the nozzle at the centerline of the jet origin y =$\frac{1}{2}$d. The penetration depth of the jet could be found when the maximum x-directional velocity was nearing zero.

7.2 Laminar simulations

Simulation of pulp-fibre suspension was first done using a laminar flow model. The laminar simulations were done on the $C_m = 2\%$ and 3% consistency suspensions at a flow rate of 0.7 dm^3/s.

The low consistency suspension $C_m = 1\%$ could not be simulated using a laminar flow model, as the low consistency jet is highly transient. A turbulence model is needed to stabilize the simulation. The CFD results for $C_m = 2\%$ and $C_m = 3\%$ laminar simulations using the Herschel-Bulkley material model are presented below for all jet discharge rates.

7.2.1 Flow discharge Q = 0.7 dm^3/s

Fig 7.5 presents the development of maximum x-directional velocity downstream from the pipe nozzle. The $C_m = 2\%$ has a smaller velocity decay rate when compared to the $C_m = 3\%$ model, where the U_x velocity is almost non-existent at $x = 25d$. For $C_m = 3\%$ birch pulp suspension the measured jet penetration depth at medium discharge rate was **L = 28d** so the CFD result is consistent with that of the measured one, as can be seen from figure 7.5.

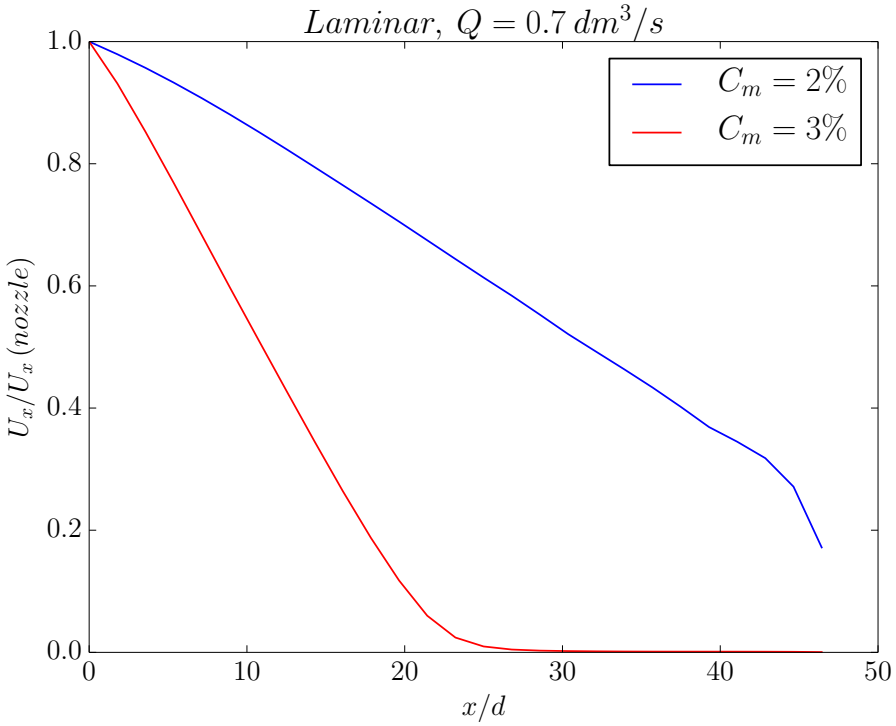

Figure 7.5 *Maximum Ux velocity development from pipe nozzle Q=0.7 dm^3/s*

For $C_m = 2\%$ the jet penetration depth was measured to be $\mathbf{L = 39.0d}$ for birch pulp suspension and $\mathbf{42.5}d$ for pine pulp. From figure 7.5 it can be seen that the velocity has decayed to approximately 40 percent of the maximum discharge velocity at this depth. Thus, it can be said that the CFD results of the laminar flow model is not that consistent with the measured penetration depth. It can be argued however that for the $C_m = 2\%$ pulp suspension, the formed fibre network strength is weaker than that of the high consistency suspension, so the interface between stagnant pulp suspension and partially yielded suspension is not as clear. In other words the $C_m = 2\%$ suspension does not exhibit the same kind of dramatic velocity decay as the $C_m = 3\%$ suspension does.

The jet angle was determined from the CFD-results by using equations 7.4 and 7.5. The jet half-angle development downstream from the pipe nozzle for laminar flow CFD models for $C_m = 2\%$ and 3% suspension are presented in figure 7.6.

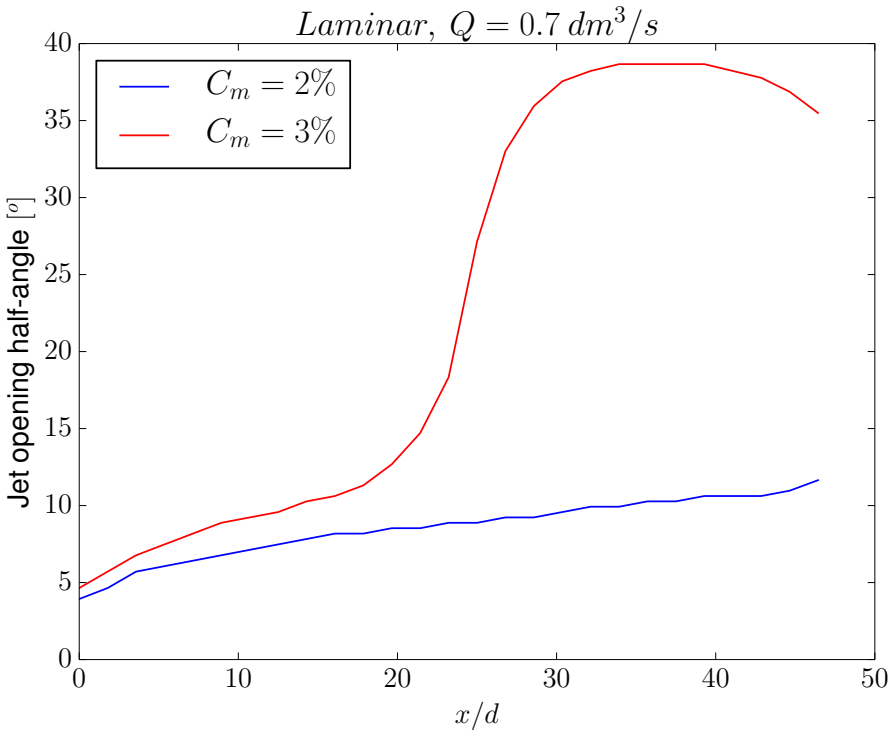

Figure 7.6 *Jet half-angle development from pipe nozzle Q=0.7 dm^3/s*

The $C_m = 2\%$ suspension model exhibits a linear increase in the jet half-angle. This results is consistent with the measured jet half-angle of **7.9** degrees for birch pulp suspension, while for pine pulp the jet half-angle was measured to be **13.6** degrees.

The $C_m = 3\%$ suspension model has a same linear growth pattern in the jet angle and a sudden increase in the angle at x=20d. This is explained by looking at the velocity decay rate from figure 7.5, which shows that the maximum flow velocity is only 10

percent of the original one. Thus, the jet is almost completely stagnant, which means that the jet half-angle has no physical significance at such low velocities. The measured jet spread angle for 3% suspension was 7.9 degrees for birch pulp suspension and 8.3 for pine pulp suspension. There is a reasonable correlation between the CFD results and the measured ones as 8 degrees is the measured angle at x=10d.

For post-processing velocity fields, a bulk velocity is introduced to equalise the velocity fields:

$$U_{bulk} = \frac{Q}{A_{inlet}}, \quad A_{inlet} = \pi \left(\frac{d_{inlet}}{2} \right)^2 \tag{7.6}$$

For a flow rate of 0.7 dm^3/s, equation 7.6 corresponds to a velocity value of 4.55 m/s. Figures 7.7 and 7.8 show x-directional velocity contours divided by bulk velocity.

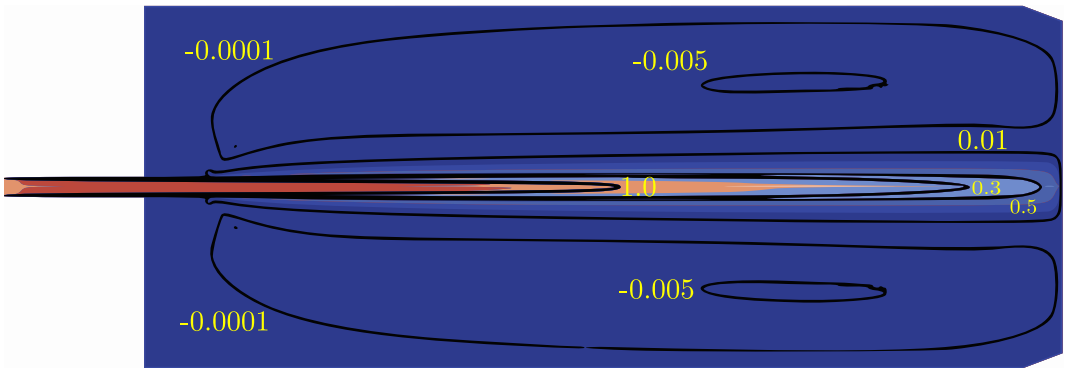

Figure 7.7 *U_x/U_{bulk} velocity contours for $C_m = 2\%$, Q=0.7dm^3/s*

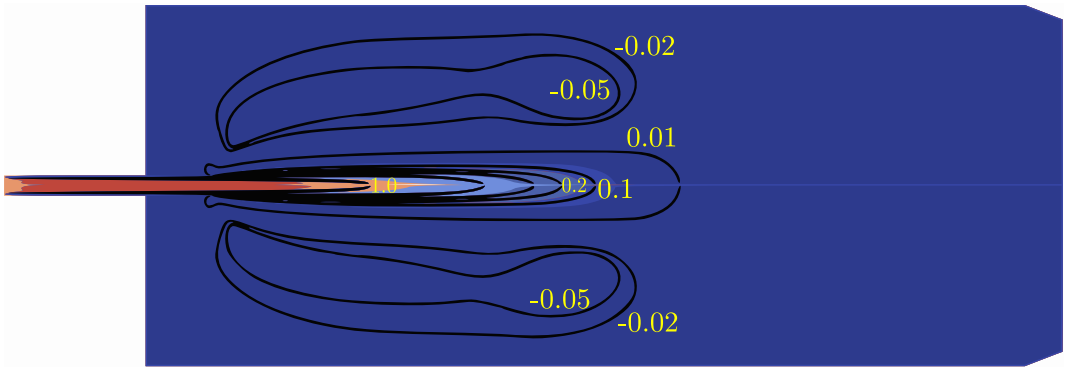

Figure 7.8 *U_x/U_{bulk} velocity contours for $C_m = 3\%$, Q=0.7dm^3/s*

The negative contours in figures 7.7 and 7.8 display reverse flow areas. The flow field produced by the laminar $C_m = 2\%$ model is incorrect, as the jet shows very little

spread and velocity decay. Thus, the laminar flow model cannot be recommended for very low mass consistency suspension modelling.

7.3 $k-\omega$ SST simulations

Simulations of turbulent pulp-fibre suspension were done with $k-\omega$ SST turbulence model combined with a Herschel-Bulkley material model for mass consistencies ranging from 1-3%. Two different flow rates were simulated, which corresponded to the flow rates used in the measurements.

The $k-\omega$ SST turbulence model proved to be a good fit for the turbulent simulations as it is computationally robust. This proved to be important, as many turbulence models, such as the $k-\varepsilon$ turbulence model had serious problems with solution convergence.

7.3.1 Flow discharge Q=0.7 dm^3/s

For the flow rate of 0.7 dm^3/s, the turbulence model is expected to increase the diffusion of momentum in the flow field. Figure 7.9 depicts the maximum x-directional velocity on the measurement plane downstream from the pipe nozzle for all mass consistencies.

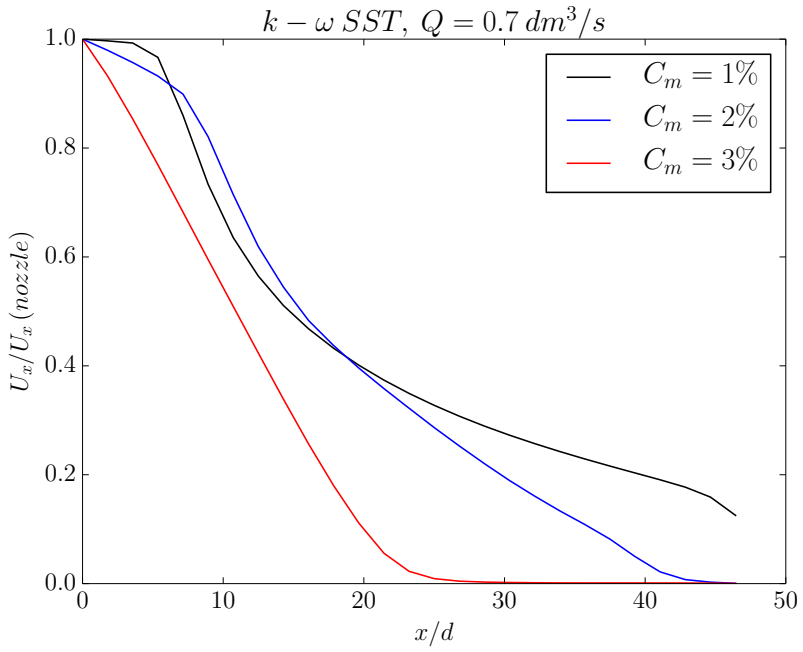

Figure 7.9 *Maximum U_x velocity development from pipe nozzle Q=0.7 dm^3/s*

The jet penetration depth could not be measured for the 1% mass consistency suspension, thus no data is available to validate the result of the black line in 7.9. The $C_m = 2\%$ $k-\omega$ SST simulation shows a faster velocity decay rate, than the laminar flow model for the same consistency. The turbulence model increases the lateral spread rate of the jet, which in turn causes the x-directional velocity to decay at a greater pace. The increased spread rate of the jet can be observed by comparing figures 7.6 and 7.10.

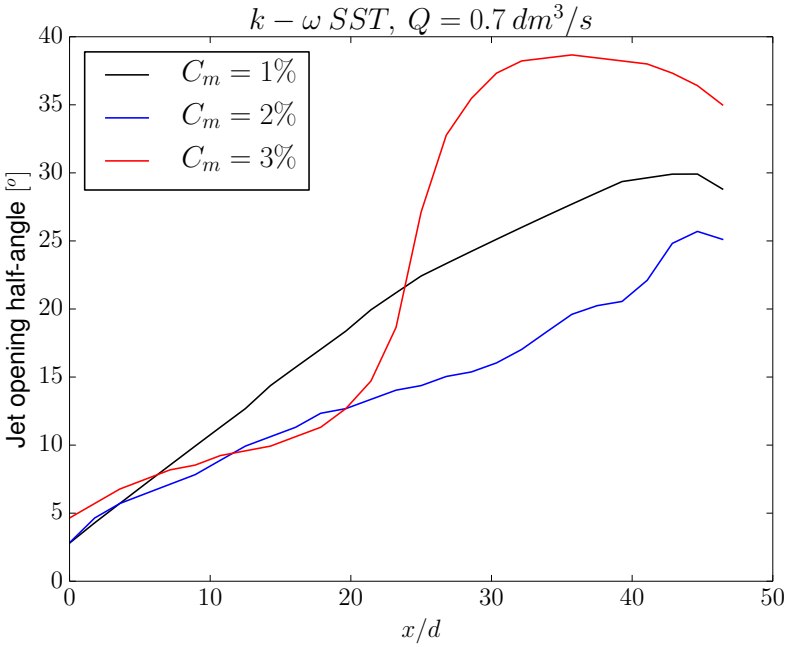

Figure 7.10 *Jet half-angle development from pipe nozzle Q=0.7 dm^3/s*

By comparing figures 7.5 and 7.6 with figures 7.9 and 7.10 for the 3% mass consistency suspension, the simulation results are practically identical. It can be interpreted from these results, that for 3% mass consistency suspension, the turbulence model has no significant effect on the resulting flow field at this velocity range. The apparent molecular viscosity given by the Herschel-Bulkley material model is dominating the flow behaviour of the jet, making turbulent viscosity negligible.

Figures 7.11, 7.12 and 7.13 show x-directional velocity contours divided by bulk velocity.

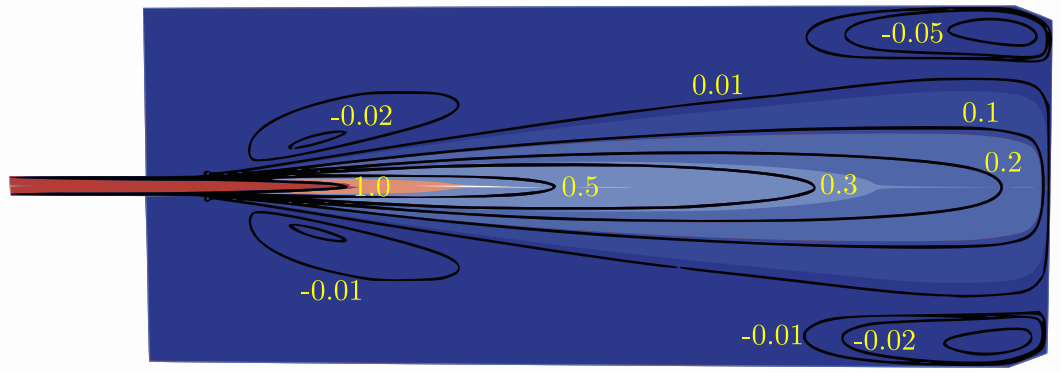

Figure 7.11 *U_x/U_{bulk} velocity contours for $C_m = 1\%$, Q=0.7dm^3/s*

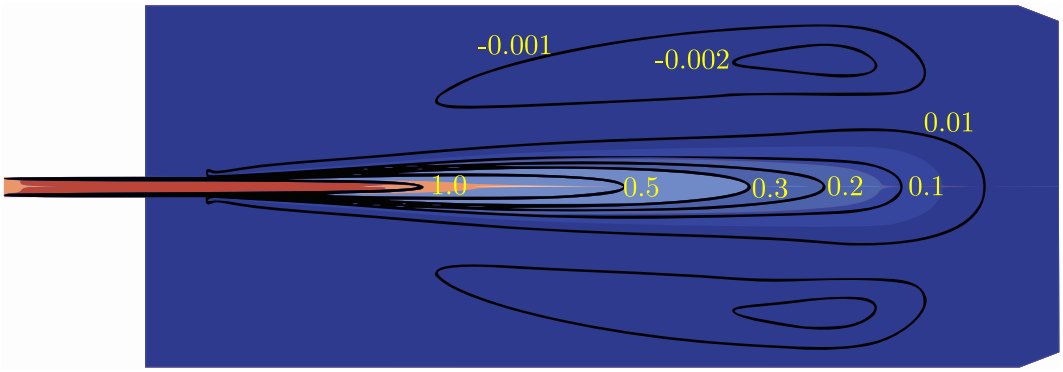

Figure 7.12 *U_x/U_{bulk} velocity contours for $C_m = 2\%$, Q=0.7dm^3/s*

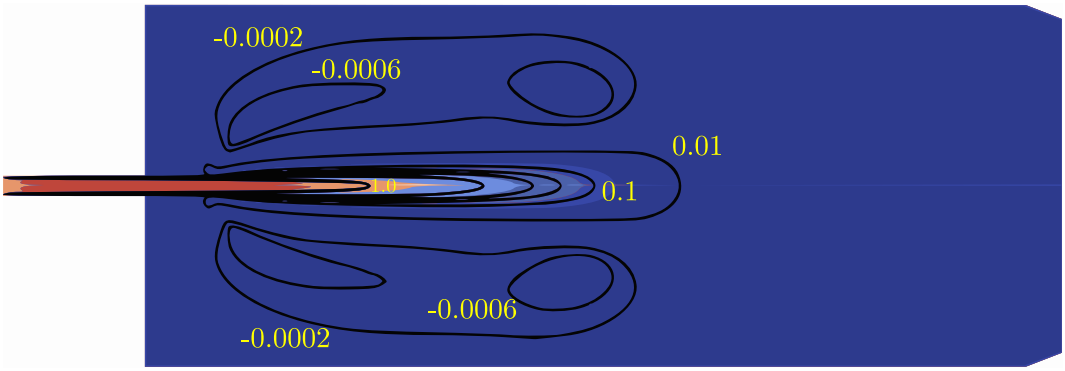

Figure 7.13 *U_x/U_{bulk} velocity contours for $C_m = 3\%$, Q=0.7dm^3/s*

From figures 7.11- 7.13, the effect of the viscosity model on the flow field is apparent. The increased molecular viscosity reduces the range of the jet greatly. The backward directional flow is also reduced by the viscosity model. Comparing velocity contours for the $C_m = 2\%$ mass consistency laminar (figure 7.7) and $k-\omega$ SST (figure 7.12) simulations show a drastic difference in the resulting jet flow shape. The turbulent simulation provides a more realistic flow field, where the jet spreads and decays in the same manner, as observed during measurements.

Velocity contours were also post-processed on the symmetry plane of the jet chamber.

Figure 7.14 shows U_x/U_{bulk} velocity contours on the symmetry plane of the jet chamber.

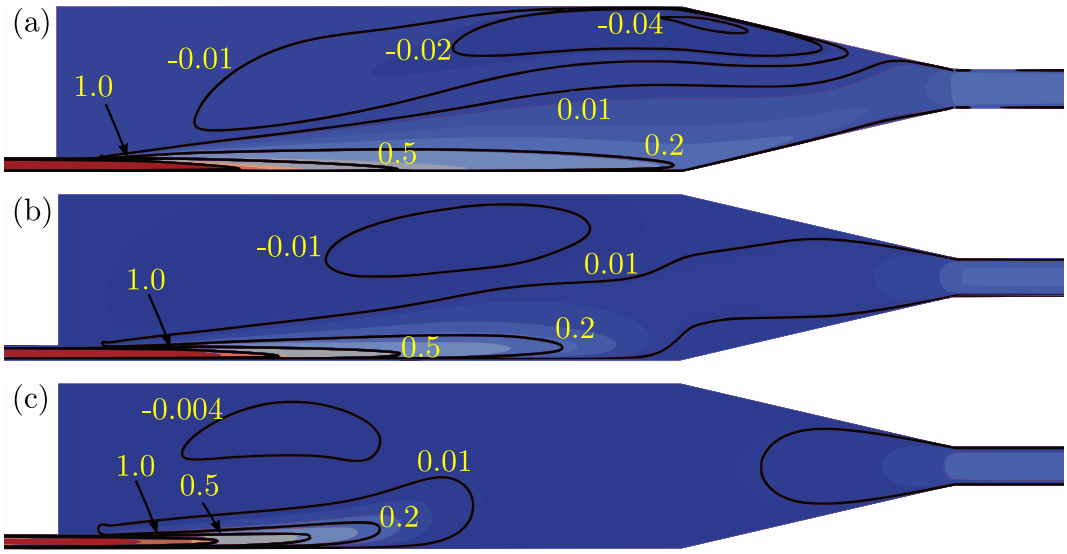

Figure 7.14 *U_x/U_{bulk} velocity contours in symmetry plane for (a): $C_m = 1\%$ (b): $C_m = 2\%$ (c): $C_m = 3\%$ suspension, Q=0.7 dm^3/s*

The $C_m = 3\%$ suspension flow field is significantly different from the lower consistencies, as can be seen from figure 7.14. The high molecular viscosity reduces the jet penetration depth and creates a plug-flow type flow region, after the jet velocity decays. Close to the outlet, the fluid velocity increases, as shearing forces break down the plug. The flow field of 1% and 2% suspensions are similar, except the reverse flow areas of 2% suspension are smaller.

The role of turbulence in the system can be observed by inspecting the ratio of eddy viscosity to apparent molecular viscosity. This viscosity ratio depicts areas of the flow where turbulence dominates the behaviour over molecular viscosity. Figure 7.15 shows the viscosity ratios for all simulated mass consistencies, at the symmetry plane of the computational domain

The increase of molecular viscosity reduces the effect of turbulence in the flow field. As seen in figure 7.15 c and a, the level of turbulence in the $C_m = 3\%$ suspension is non-existent at this velocity range, while in the $C_m = 1\%$ the turbulent viscosity can be 25-times higher than the molecular viscosity. The intensity of turbulence is highest at the pipe nozzle, where high shearing forces are present. Highly turbulent areas are also found in the angled section of the tank, where shearing forces increase, as the cross-section area of the flow decreases.

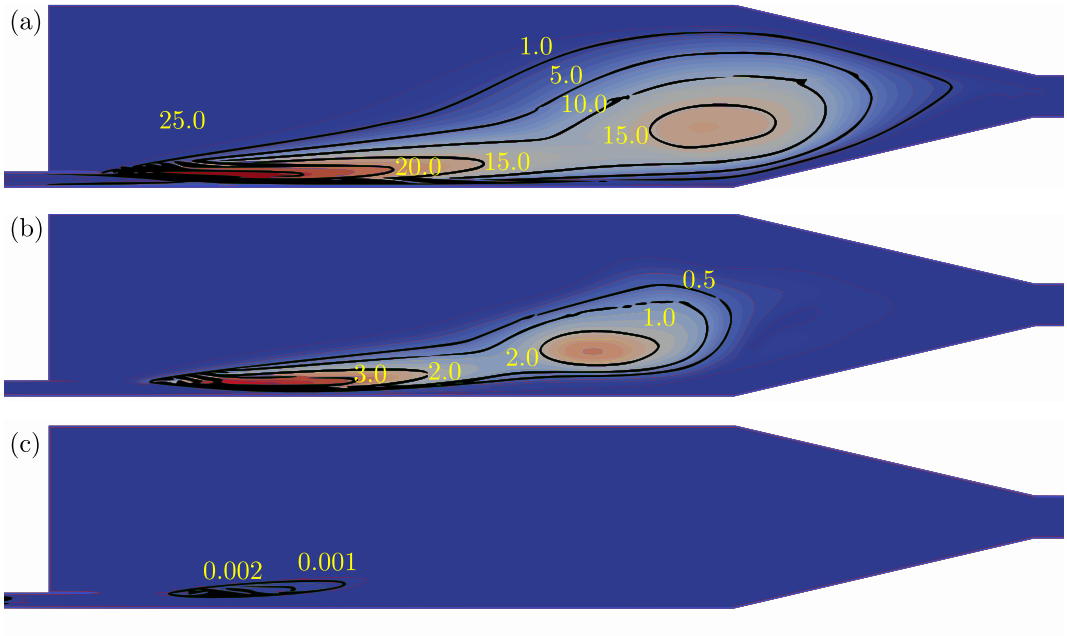

Figure 7.15 *Viscosity ratios for (a): $C_m = 1\%$ (b): $C_m = 2\%$ (c): $C_m = 3\%$ suspension, Q=0.7 dm^3/s*

7.3.2 Flow discharge Q=1.05 dm^3/s

The suspension jet flow field was also simulated for 1.05 dm^3/s using the $k-\omega$ SST turbulence model and HB-material model. With increasing flow rate, the unsteady turbulent effects become more prominent in the flow field. Convergence of the solution was harder to achieve at high flow rate. To increase the numerical robustness of the simulation, an initial solution field was first achieved with a coarse mesh, which was then mapped onto the fine mesh, where the final solution was achieved.

Figure 7.16 shows the velocity decay rate for all simulated consistencies for the $k-\omega$ SST turbulence model.

The measured jet penetration depths for birch pulp suspension at Q=1.05 dm^3/s were **47.3d** and **41.6d** for $C_m = 2\%$ and $C_m = 3\%$ consistencies respectively. There is a good agreement with the simulated and measured penetration depths, especially for 3 percent mass consistency suspension, as can be seen from figure 7.16.

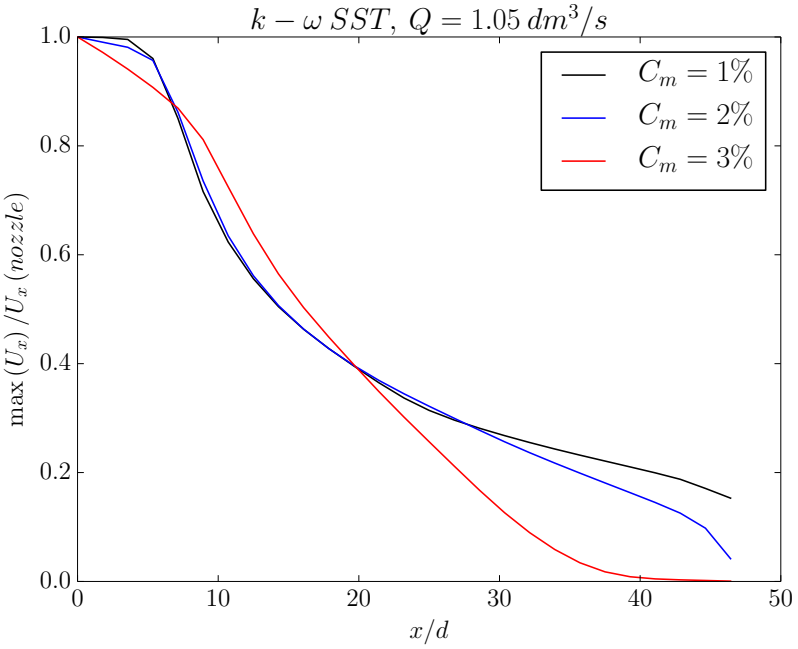

Figure 7.16 *Maximum U_x velocity development from pipe nozzle Q=1.05 dm^3/s*

Figure 7.17 presents the jet half-angle downstream from the pipe nozzle. The measured angles for birch pulp suspension at flow rate of Q=1.05dm^3/s were **10.3**^{o} and **10.0**^{o} degrees for $C_m = 2\%$ and $C_m = 3\%$ consistencies respectively.

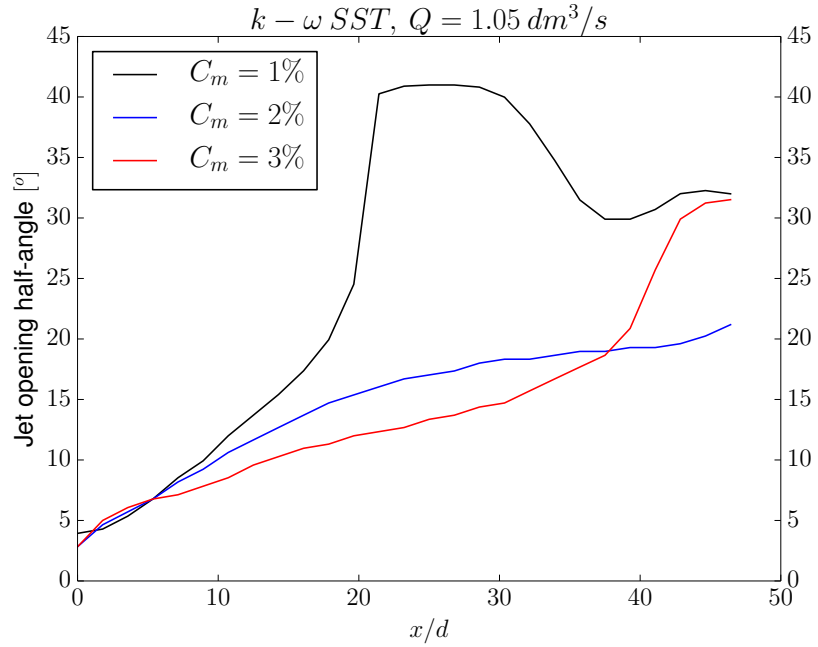

Figure 7.17 *Jet half-angle development from pipe nozzle Q=1.05 dm^3/s*

The $C_m = 1\%$ jet angle increases very fast and is bounded by the tank walls at x=20d. The angle of the jets for $C_m = 2\%$ and 3% suspensions increases linearly

until the jet decays.

The U_x/U_{bulk} velocity contours for all consistency suspensions are presented in figures 7.18, 7.19 and 7.20. The 1 percent mass consistency suspension jet attaches to the wall at x=20d as seen in figure 7.17. The 2 and 3 percent suspension flow fields are similar to those of the lower discharge rate, except the reach of the jet is longer. The turbulence model is necessary at this flow rate to stabilize the system of equations presented in chapter 4.

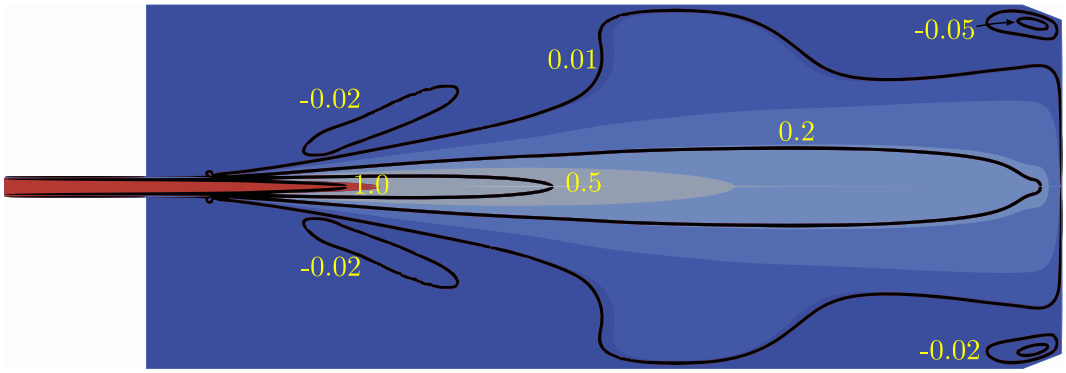

Figure 7.18 *U_x/U_{bulk} velocity contours for $C_m = 1\%$, Q=1.05dm$^3/s$*

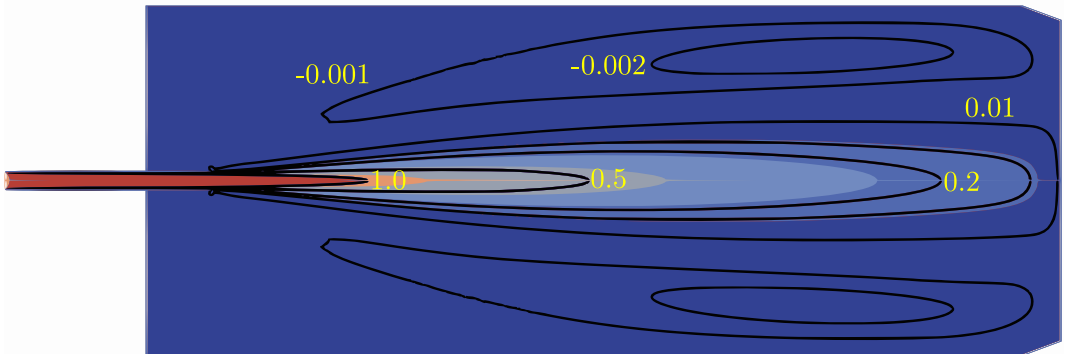

Figure 7.19 *U_x/U_{bulk} velocity contours for $C_m = 2\%$, Q=1.05dm$^3/s$*

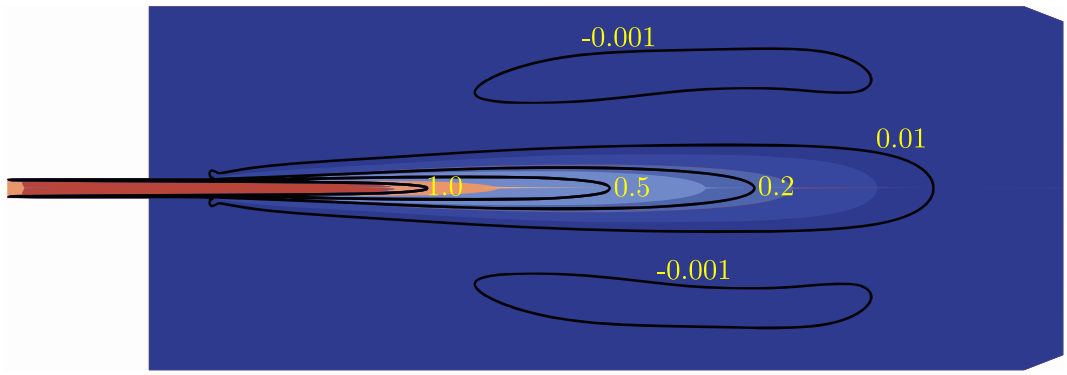

Figure 7.20 *U_x/U_{bulk} velocity contours for $C_m = 3\%$, Q=1.05dm$^3/s$*

Dimensionless velocity contours viewed from the symmetry plane are illustrated in figure 7.21 for all mass consistencies. The increase of molecular viscosity through the

material model reduces the range of the jet in the same manner as in the lower flow rate simulations. The difference between the 1 percent and 2 percent consistency suspension is mainly in the reserve flow areas, which are bigger for 1 percent mass consistency suspension.

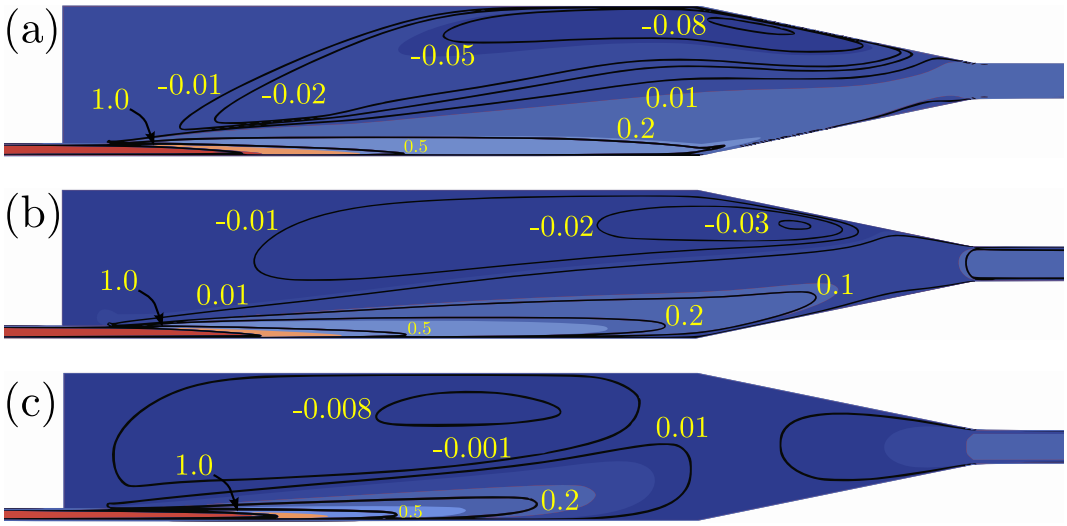

Figure 7.21 *U_x/U_{bulk} velocity contours in symmetry plane for (a): $C_m = 1\%$ (b): $C_m = 2\%$ (c): $C_m = 3\%$ suspension, Q=1.05 dm^3/s*

Viscosity ratios on the symmetry plane for this flow rate are presented in figure 7.22.

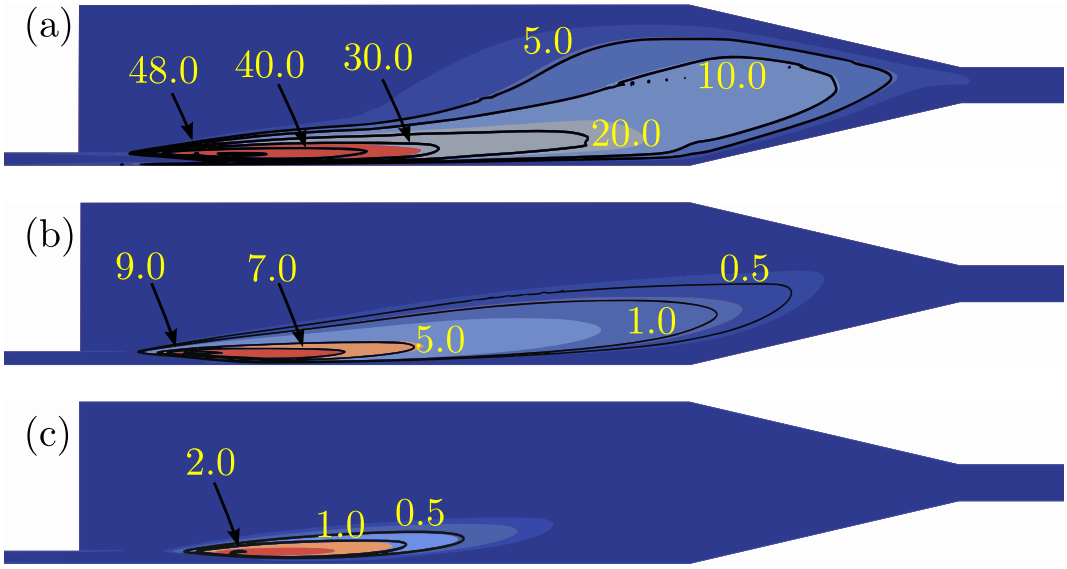

Figure 7.22 *Viscosity ratios for (a): $C_m = 1\%$ (b): $C_m = 2\%$ (c): $C_m = 3\%$ suspension, Q=1.05 dm^3/s*

Turbulent viscosity is as significant as the apparent viscosity in the high flow rate simulations for all consistencies. Increasing the flow rate increases the viscosity ratio

for all consistencies, as shearing forces in the flow are higher, thus increasing the role of eddy viscosity.

7.4 CFD and PUDV comparison

The velocity profiles measured by pulsed ultrasound doppler velocimetry were compared to the simulated velocity profiles. From the measured velocity profiles, it is apparent that there is a wall-slip effect in the suspension flow field, as the velocity abruptly jumps to a high value close to the wall. However, PUDV cannot measure near-wall velocities accurately, so the near wall velocities measured by PUDV should be considered critically.

Figure 7.23 shows the measured PUDV velocity profile and the $k-\omega$ SST simulation for $C_m = 1\%$ mass consistency suspension at a flow rate of Q=0.7 dm^3/s.

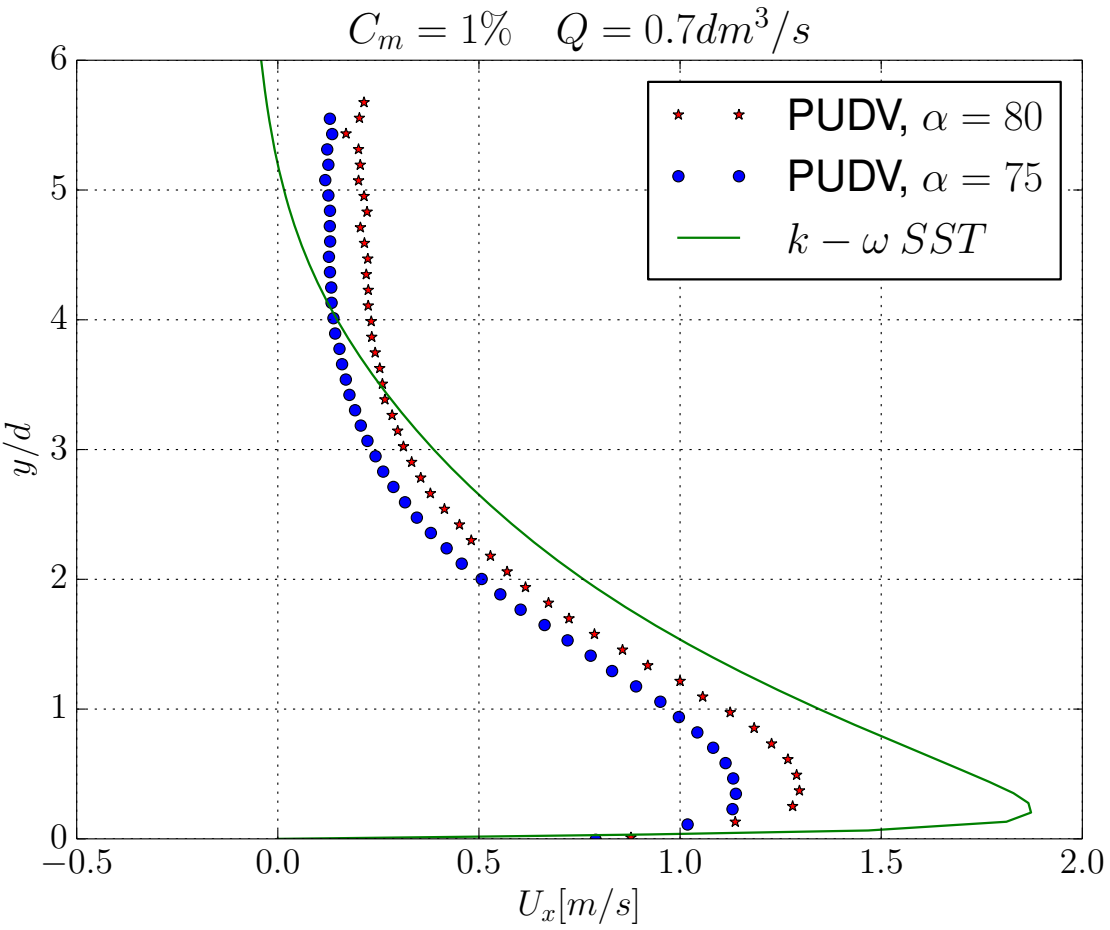

Figure 7.23 *Measured velocity profiles for $C_m = 1\%$ birch pulp suspension compared to $k-\omega$ SST simulation*

There is an reasonable agreement with the measured velocity profile and the profile

gained through $k-\omega$ SST turbulence model. The general trend of the profile is is close to that of the measured one when y=$1-4d$, but a deviation in the trend begins as y increases. The measured profile evens out at approximately $U_x = 0.25$ m/s, while the simulated profile continues to decay and producing reverse flow.

Figure 7.24 shows the measured PUDV velocity profile against a laminar simulation and $k-\omega$ SST simulation.

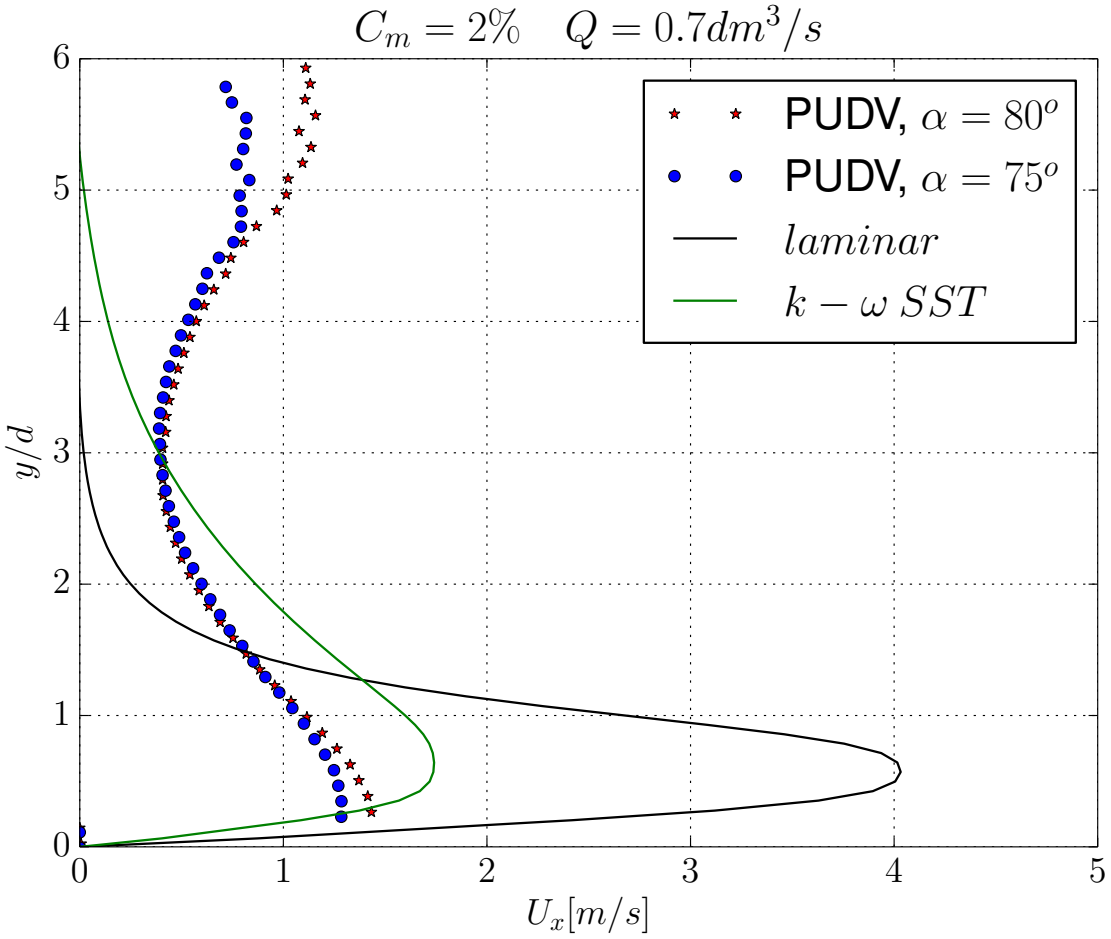

Figure 7.24 *Measured velocity profiles for $C_m = 2\%$ birch pulp suspension compared to $k-\omega$ SST simulation and laminar simulation*

From figure 7.24 it can be seen, that the laminar simulation fails to predict the measured profile completely, producing a very sharp profile with a high velocity peak. The increased turbulent diffusion from the $k-\omega$ SST model spreads the jet momentum in the y-direction and creating a more correct velocity profile. There is however, a big difference between the SST model velocity profile and the measured one after $y > 3d$. The increase in velocity in the measured profile could be a measurement error.

Figure 7.25 shows the measured velocity profile compared to velocity profiles gained from laminar and $k-\omega$ SST simulations at $C_m = 3\%$ mass consistency.

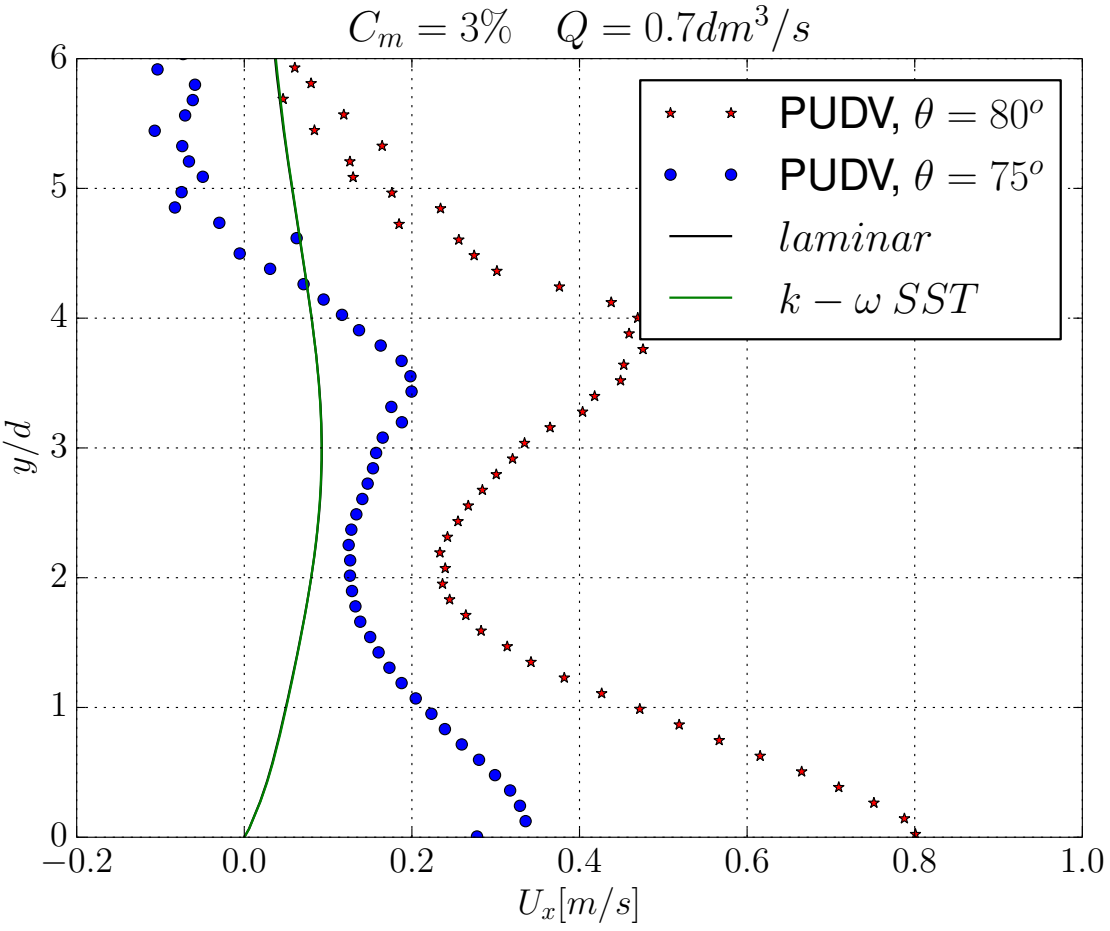

Figure 7.25 *Measured velocity profiles for $C_m = 3\%$ birch pulp suspension compared to $k-\omega$ SST simulation and laminar simulation*

The simulated velocity profiles overlap, as the turbulence model has no significant effect on the simulated flow field at $C_m = 3\%$. There is a significant deviation between the measured and simulated profiles. The shape of the measured profile is complex, there is a apparent wall-slip effect after which velocity decays. Moving further into the suspension, the velocity increases after y=2d to create a small velocity peak at y=4d.

From the PUDV measurements it can be concluded, that the real flow field of a pulp-fibre suspension wall jet is complex. A simple simulation approach, such as the combination of turbulence model and a viscosity model, is unable to predict the details of the flow field.

8. CONCLUSION AND DISCUSSION

Predicting the flow field of turbulent pulp-fibre suspension is a complex problem. The new experimental approach presented in this thesis allowed the visualization of turbulent pulp-fibre jet discharging next to a wall. The effect of mass consistency and flow rate on the jet penetration depth and opening angle was easily seen in the image analysis.

The simulation method presented in this thesis is a simplified way of approaching the problem of non-Newtonian turbulent flow. The resulting flow field from combining a Herschel-Bulkley material model with a $k-\omega$ SST turbulence model does correlate with the jet measurements made from the photographs. There is, however, a big deviation between the velocity profiles measured by PUDV and the simulated ones. The inner flow field produced by the wall jet is more complicated, than what a simple single-phase flow model predicts.

In industrial applications, the objectives of CFD modelling is to simulate the flow field inside the unit process as accurately as possible and test new geometries. For these purposes, the simulation approach used in this thesis fits well, as simulation results can be obtained in relatively quick time frames. Having rheological data for the viscosity model is very important for accurate simulations. For turbulence modelling, the $k-\omega$ SST turbulence model is the preferred choice. The numerical robustness of the model makes it well suited for complex geometries found in industrial processing equipment.

The work presented here indicates, that the CFD code OpenFOAM can be used to simulate process equipment with non-Newtonian medium such as pulpers and mixing tanks. The open-source code allows easy customization of solvers and flow models. OpenFOAM is also well suited for big problems found in industrial applications, due to ease of parallelization and no additional software license costs.

Experimental validation of CFD models is very important. Future work in pulp-fibre suspension research should be directed at designing and creating new experimental configurations, which would reveal more about the flow behaviour of the suspension.

Flow field of pulp-fibre suspension in rotating machinery is one of the key interests in industrial applications. Additionally, there is a rising interest in high consistency pulp processing. The flow behaviour of high mass consistency suspension ($C_m > 5\%$) is very different from the consistencies used in this thesis and additional work is needed in order to correctly simulate high consistency pulp-fibre suspension flow.

BIBLIOGRAPHY

[1] K. F. K. Adane, "Experimental and numerical investigation of three dimensional laminar wall jet of newtonian and non-newtonian fluids," University of Manitoba, 2009, 7 p. Available: http://mspace.lib.umanitoba.ca/jspui/bitstream/1993/3871/1/Adane-KFK.pdf.

[2] U. Ayachit, *The ParaView Guide: A Parallel Visualization Application*. Kitware, 2015.

[3] S. B.Pope, *Turbulent Flows*. Cambridge University Press, 2000.

[4] R. Chhabra and J. Richardson, *Non-Newtonian Flow and Applied Rheology: Engineering Applications*, 2nd ed. Oxford, UK: Elsevier, 2008.

[5] B. Derakhshandeh, "Rheology of low to medium consistency pulp fibre suspensions," Ph.D. dissertation, The University of British Columbia, 2011, Available: http://turbulence-initiated.sites.olt.ubc.ca/files/2013/02/2011-Derakhshandeh-PhD-thesis-Pulp-Rheology.pdf.

[6] B. Derakhshandeh, S. G. Hatzikiriakos, and C. P. Bennington, "The apparent yield stress of pulp fiber suspensions," *Journal of Rheology*, vol. 54, no. 5, pp. 1137–1154, 2010.

[7] B. Derakhshandeh, R. Kerekes, and C. P. Bennington, "Rheology of pulp fibre suspensions: A critical review," *Chemical Engineering Science*, vol. 66, pp. 3460–3470, 2011.

[8] C. Donofrio, *Introduction to Pulping*, ser. Pulp and paper science and technology, Volume 1: Pulp. Joint Textbook Committee of the Paper Industry, 1962.

[9] P. Durbin, "Near-wall turbulence closure modelling without damping functions," *Theoretical and Computational Fluid Dynamics*, vol. 3, pp. 1–13, 1991.

[10] F. Ein-Mozaffari, C. P. J. Bennington, G. A. Dumont, and D. Buckingham, "Measuring flow velocity in pulp suspension mixing using ultrasonic doppler velocimetry," *Chemical Engineering Research and Design*, vol. 85, pp. 591–597, 2007.

[11] M. A. Garman, "Local particle velocity measurements in slurry flow in pipes and centrifugal pumps using ultrasound technique," Ph.D. dissertation, Case Western Reserve University, 2015.

[12] A. A. Gavrilov and V. Y. Rudyak, "A model of averaged molecular viscosity for turbulent flow of non-newtonian fluids," *Journal of Siberian Federal University. Mathematics and Physics*, vol. 7, pp. 46–57, 2014.

[13] ——, "Reynolds-averaged modeling of turbulent flows of power-law fluids," *Journal of Non-Newtonian Fluid Mechanics*, vol. 227, pp. 45–55, 2015.

[14] K. Hanjalić, M. Popovac, and M. Hadžiabdić, "A robust near-wall elliptic-relaxation eddy-viscosity turbulence model for cfd," *International Journal of Heat and Fluid Flow*, vol. 25, pp. 1047–1051, 2004.

[15] J.-P. Huhtanen, "Non-newtonian flows in paper making," Tampere University of Technology, Tech. Rep. 137, 1998.

[16] ——, "Modeling of fiber suspension flows in refiner and other papermaking processes by combining non-newtonian fluid dynamics and turbulence," Ph.D. dissertation, Tampere University of Technology, 2004.

[17] F. Juretić, *cfMesh User Guide v.1.1.1*. Zagreb, Croatia: Creative Fields, Ltd, 2015.

[18] A. Jäsberg, "Flow Behaviour of Fibre Suspensions in Straight Pipes: New Experimental Techniques and Multiphase Modeling," Ph.D. dissertation, University of Jyväskylä, 2007.

[19] R. Kerekes and C. Schell, "Characterization of fibre flocculation regimes by a crowding factor," *Journal of pulp and paper science*, vol. 18, no. 1, pp. 32–38, 1992.

[20] B. Launder and W. Rodi, "The turbulent wall jet - measurements and modeling," *Annual Review of Fluid Mechanics*, vol. 15, pp. 429–459, 1983.

[21] K. Madlener, B. Frey, and H. Ciezki, "Generalized Reynolds Number For Non-Newtonian Fluids," *Progress in Propulsion Physics*, no. 1, pp. 237–250, 2009.

[22] D. Martinez, K. Buckley, S. Jivan, A. Lindström, R. Thiruvengadaswamy, J. Olson, T. Ruth, and R.J.Kerekes, "Characterizing the mobility of papermaking fibres during sedimentation," in *12th Fundamental Research Symposium*, Oxford, September 2001.

[23] F. Menter, M. Kuntz, and R. Langtry, "Ten years of industrial experience with the sst turbulence model," *Turbulence, Heat and Mass Transfer*, vol. 4, 2003.

[24] A. Metzner and J. Reed, "Flow of non-newtonian fluids - correlation of the laminar, transition and turbulent-flow regions," *AiChE journal*, vol. 1, 1955.

[25] K. Mustalahti, "Measurements of flow properties of pulp suspension," 2015, master of Science Thesis.

[26] B. Norman, *Web Forming*, 2nd ed., ser. Papermaking Science and Technology Book 8: Papermaking Part 1, Stock Preparation and Wet End. Helsinki, Finland: Finnish Paper Engineers' Association, 2007, pp. 216–288.

[27] J. A. Olson, S. Delfel, C. Ollivier-Gooch, and R. W. Gooding, "Computational fluid dynamics in the pulp and paper industry - the design of a high performance pulp screen rotor," in *Seventh International Conference on CFD in the Minerals and Process Industries*, Melbourne, Australia, December 2009.

[28] "Salome the open source integration platform for numerical simulations," Open Cascade, http://www.salome-platform.org/.

[29] L. Pakzad, F. Ein-Mozaffari, and P. Chan, "Using computational fluid dynamics modeling to study the mixing of pseudoplastic fluids with a scaba 6srgt impeller," *Chemical Engineering and Processing*, vol. 47, pp. 2218–2227, 2008.

[30] F. Pinho, "A GNF framework for turbulent flow models of drag reducing fluids and proposal for a $k - \varepsilon$ type closure," *Journal of Non-Newtonian Fluid Mechanics*, vol. 114, pp. 149–184, 2003.

[31] L. F. Richardson, "Weather prediction by numerical process," Cambridge, 1922.

[32] P. Sagaut, *Large Eddy Simulation for Incompressible Flows*, 2nd ed. Berlin Heidelberg: Springer-Verlag, 2002.

[33] B. Sajjadi, A. A. A. Raman, and R. Parthasarathy, "Fluid dynamic analysis of non-newtonian flow behaviour of municipal sludge simulant in anaerobic digesters using submerged, recirculating jets," *Chemical Engineering Journal*, vol. 298, pp. 259–270, 2016.

[34] Y. Takeda, "Velocity profile measurement by ultrasonic doppler method," *Experimental Thermal and Fluid Science*, vol. 10, pp. 444–453, 1995.

[35] R. I. Tanner, *Engineering Rheology*, 2nd ed. New York, United States: Oxfor University Press, 2000.

[36] The OpenFOAM Foundation, *OpenFOAM User Guide*, 2016, Available: https://www.openfoam.org.

[37] H. K. Versteeg and W. Malalasekera, *An Introduction to Computational Fluid Dynamics: The Finite Volume Method*. Pearson Education Limited, 2007.

[38] T. Wang, J. Wang, F. Ren, and Y. Jin, "Application of doppler ultrasound velocimetry in multihpase flow," *Chemical Engineering Journal*, vol. 92, pp. 111–122, 2002.

[39] H. Weller, G. Tabor, H. Jasak, and C. Fureby, "A tensorial approach to computational continuum mechanics using object-oriented techniques," *Computers in Physics*, vol. 12, no. 6, 1998.

[40] H. Xu, "Measurement of fiber suspension flow and forming jet velocity profile by pulsed ultrasonic doppler velocimetry," Ph.D. dissertation, Institute of Paper Science and Technology, 2003.

[41] W. Zheng, C. Yan, H. Liu, and D. Luo, "Comparative assessment of sas and des turublence modeling for massively separated flows," *Acta Mechanica Sinica*, vol. 32, pp. 12–21, 2015.